

Binder Effects on Si-Alloy Electrode Performance

by

Congxiao Wei

Submitted in partial fulfillment of the requirements
for the degree of Master of Science

at

Dalhousie University
Halifax, Nova Scotia
November 2019

© Copyright by Congxiao Wei, 2019

TABLES OF CONTENTS

LIST OF TABLES	v
LIST OF FIGURES	vi
ABSTRACT	x
LIST OF ABBREVIATIONS AND SYMBOLS USED.....	xi
ACKNOWLEDGEMENTS	xiv
Chapter 1 INTRODUCTION.....	1
1.1 Background	1
1.1.1 Cathodes	3
1.1.2 Anodes	4
1.1.3 Electrolytes	4
1.1.4 Binders	5
1.2 Organic Binders	6
1.2.1 Unfunctionalized Polymeric Binders	6
1.2.2 Functionalized Polymeric Binders	8
1.3 Optimization of Organic Binders in Cells.....	11
1.4 Inorganic Binders	14
1.5 Motivation.....	15
Chapter 2 EXPERIMENTAL SECTION.....	17
2.1 Electrochemical Cells.....	17
2.2 Electrochemical Measurements	18
2.3 Ion Milling	20
2.4 Scanning Electron Microscopy and Energy Dispersive X-ray Spectroscopy	21
2.5 Thermogravimetric Analysis	23
Chapter 3 SMALL FUNCTIONAL MOLECULES AS SLURRY ADDITIVES FOR SI- ALLOY COATINGS WITH CMC/SBR BINDER	24
3.1 Introduction	24
3.2 Experimental	25

3.3 Results and Discussion.....	27
3.4 Conclusion	33
Chapter 4 THE EFFECT OF BINDER MOLECULAR WEIGHT ON ALLOY ANODE CYCLING PERFORMANCE	35
4.1 Introduction	35
4.2 Experimental	37
4.3 Results and Discussion.....	40
Section I Effect of Binder MW on Alloy Cycling.....	40
Section II Slurry Recipe Optimization & Viscosity Measurement	48
4.4 Conclusions	52
Chapter 5 MOLECULAR BINDERS FOR SI-ALLOY ANODES.....	53
5.1 Introduction	53
5.2 Experimental	54
5.3 Results and Discussion.....	55
5.4 Conclusion	60
Chapter 6 THE EFFECT OF BINDERS ON ALLOY DEGRADATION AND CYCLING	61
6.1 Introduction	61
6.2 Experimental	62
6.3 Results and Discussion.....	63
6.4 Conclusion	74
Chapter 7 INORGANIC COMPOUNDS AS BINDERS FOR SI-ALLOY ANODES	76
7.1 Introduction	76
7.2 Experimental	76
7.3 Results and Discussion.....	77
7.4 Conclusion	87
Chapter 8 CONCLUSION	88
8.1 Conclusions	88
8.2 Future work	91

Bibliography95

LIST OF TABLES

Table 1.1 Chemical structures of unfunctionalized polymers.....	8
Table 1.2 Chemical structures of functionalized polymers.....	11
Table 4.1 Physical state and molecular weight of PAA or NaPAA binders.	39
Table 4.2 Slurry formulations of the prepared V7 (or V7 fines)-NaPAA coatings.	40
Table 4.3 Capacity retention and coulombic efficiency of the neat V7f electrodes as indicated.	48
Table 4.4 Formulations of the prepared neat V7f slurries using different MW binders. ..	50
Table 5.1 Slurry formulations used in this study (all quantities in grams).	54
Table 6.1 Cycling performance of V7/LiPAA, V7/CA, and V7/PVDF electrodes after different cycles.	65
Table 7.1 Densities of electrode component materials in g/cm ³	81

LIST OF FIGURES

Figure 1.1 Schematic diagram of an LCO cathode (on aluminum foil) vs. graphite anode (on copper foil) lithium ion cell showing the direction the electrons and lithium ions flow during the charging process.....	2
Figure 2.1 An exploded view of a coin cell.	17
Figure 2.2 First cycle potential vs. capacity curve of a Si-alloy electrode. Reversible and irreversible capacities during the initial lithiation process are shown as indicated.	19
Figure 2.3 A schematic diagram showing the working principle of a cross-section polisher (CP). A sample is placed in the beam path of a stationary broad argon beam. The area in the dashed red circle represents the sample protruding from the edge of the masking plate.....	20
Figure 3.1 Chemical structures of the slurry additives tested. All additives contain various number of carboxyl/carboxylate groups.	27
Figure 3.2 Capacity retention (a) and CE (b) vs cycle number of V7/graphite electrode and electrode prepared with different slurry additives.	29
Figure 3.3 The first cycle potential vs. capacity curves of the V7/graphite-CMC/SBR electrode and electrodes with Na mellitate, Na citrate, NaPAA additives.	30
Figure 3.4 Cross sectional SEM images of Si alloy-graphite electrode. (a) Fresh electrode without additive, (b) after 100 cycles without additive, (c) after 100 cycles with Na mellitate, (d) after 100 cycles with NaCA, (e) after 100 cycles with NaPAA (1.2k), (f) after 100 cycles with Na acetate. Light grey, dark grey, and black areas correspond to V7 alloy particles, SEI layers, and graphite, respectively. 32	
Figure 4.1 Appearance of V7/1.2k/H ₂ O and V7/250k/H ₂ O electrodes. Both electrodes show particle settling.....	41
Figure 4.2 Cross-sectional schematic diagrams of (a) V7/low MW binder/H ₂ O and (b) V7/high MW binder/H ₂ O. Grey areas correspond to the binder solution in electrode slurries.....	42
Figure 4.3 The first cycle potential vs. capacity curves of V7/1.2k/H ₂ O and V7/1250k/H ₂ O electrodes, respectively.	42

Figure 4.4 Cycling performance V7 electrodes using NaPAA binders with different MW.	43
Figure 4.5 Appearance of V7/250k/CMC (left) and V7/1.2k/CMC (right) electrodes.....	44
Figure 4.6 The cycling of (a) V7/250k/H ₂ O and V7/250k/CMC electrodes, and (b) V7/1.2k/H ₂ O and V7/1.2k/CMC electrodes.....	44
Figure 4.7 Thermogravimetric Analysis (150 mL/min air flow, 1 °C/min) of a 45 wt% NaPAA 1.2k aqueous solution and a propylene glycol solvent in a weight ratio of 1:1.....	45
Figure 4.8 Cycling performance of (a) V7/1.2k/PG, (b) V7f/1.2k/H ₂ O, and (c) V7f/1.2k/PG electrodes.....	46
Figure 4.9 (a) Cycling performance and (b) CEs of V7f electrodes with different MW NaPAA binders and with PG or H ₂ O slurry solvent.....	47
Figure 4.10 Viscosity vs. time curves for electrode slurries using different MW NaPAA binders as indicated.....	51
Figure 5.1 Viscosity vs. time curves for V7-CA slurries made with (a) PG and (b) H ₂ O. (b) Digital photos of V7-CA coatings made with (c) PG and (d) H ₂ O solvent.	56
Figure 5.2 The first cycle potential vs. capacity curves of V7-CA/PG and V7-LiPAA/H ₂ O electrodes.....	56
Figure 5.3 (a) Capacity retention and (b) CE for V7-CA/PG and V7-LiPAA/H ₂ O electrodes.....	57
Figure 5.4 The first cycle potential vs. capacity curves of V7/MAGE-CA and V7/MAGE- LiPAA electrodes.....	58
Figure 5.5 (a) Capacity retention and (b) CE of V7/MAGE-CA and V7/MAGE-LiPAA electrodes.....	58
Figure 5.6 Cross-sectional BSE images of (a) V7/MAGE-CA/PG and (b) V7/MAGE- LiPAA/H ₂ O electrodes.....	59
Figure 6.1 (a) Capacity retention vs. cycle number for V7/CA, V7/LiPAA, and V7/PVDF electrodes. (b) CE for V7/CA and V7/LiPAA electrodes.....	64

Figure 6.2 BSE images of V7/LiPAA electrodes after different cycles without image processing.	66
Figure 6.3 BSE images of V7/CA electrodes after different cycles as indicated without image processing.	67
Figure 6.4 BSE images V7/PVDF electrodes after different cycles as indicated without image processing.	68
Figure 6.5 (A) An original BSE image of a neat V7 electrode obtained by SEM. (B) Brightness of image A increased by 40%. (C) Contrast of image A increased by 40%. (a-c) Corresponding histogram of image A-C.....	68
Figure 6.6 (A) A cross-sectional BSE image of a V7/LiPAA electrode after 20 cycles (B) Image (A) processed by increasing the contrast to the maximum. (a) and (b) Corresponding histograms of image (A) and (B), respectively.	70
Figure 6.7 Processed cross-sectional BSE images of V7/LiPAA electrodes after different cycles as indicated.	71
Figure 6.8 Processed cross-sectional BSE images of V7/CA electrodes after different cycles as indicated.	72
Figure 6.9 Processed cross-sectional BSE images of V7/PVDF electrodes after different cycles as indicated.	73
Figure 6.10 Alloy volume fraction vs. cycle number for pristine and post-cycled (a) V7/LiPAA electrodes, (b) V7/CA, and (c) V7/PVDF electrodes.	74
Figure 7.1 Structures of the inorganic binders investigated in this study.	77
Figure 7.2 (a) Lithium polysilicate conversion to hydrated lithium polysilicate. (b) Proposed mechanism of hydrated lithium polysilicate connected onto the particle surface.	78
Figure 7.3 Digital photographs of (a-c) neat Si alloy and (d-i) neat graphite coatings prepared with $\text{Li}_2\text{Si}_5\text{O}_{11}$, $(\text{NaPO}_3)_n$, and H_2LiPO_4 binders, as indicated.	79
Figure 7.4 (a) Potential curves and (b) differential capacity curves of LiPAA, $\text{Li}_2\text{Si}_5\text{O}_{11}$, $(\text{NaPO}_3)_n$, and H_2LiPO_4 binders vs. Li-metal as measured in a TiN/binder composite coating.	80

Figure 7.5 The first cycle potential vs. capacity curves of neat V7 electrodes with $\text{Li}_2\text{Si}_5\text{O}_{11}$, $(\text{NaPO}_3)_n$, H_2LiPO_4 , and LiPAA binders, respectively.	81
Figure 7.6 Cycling performance of (a) V7- $\text{Li}_2\text{Si}_5\text{O}_{11}$, (b) V7- $(\text{NaPO}_3)_n$, (c) V7- H_2LiPO_4 , (d) graphite- $\text{Li}_2\text{Si}_5\text{O}_{11}$ and (e) graphite-20 wt% inorganic binders electrodes. The electrochemical performance of V7 electrodes using inorganic binders was shown with the comparison of a V7-LiPAA electrode.	82
Figure 7.7 SEM images of (a, c, e) pristine and (b, d, f) post-cycled (100 cycles) V7- $\text{Li}_2\text{Si}_5\text{O}_{11}$, V7- $(\text{NaPO}_3)_n$, and V7- H_2LiPO_4 electrodes, respectively.	84
Figure 7.8 (a, d, g) BSE, (b, e, h) C mapping, and (c, f, i) Si/P mapping of pristine graphite- $\text{Li}_2\text{Si}_5\text{O}_{11}$, graphite- $(\text{NaPO}_3)_n$, and graphite- H_2LiPO_4 electrodes, respectively.	85
Figure 7.9 Calculated and measured inorganic binder volume fractions in graphite/binder (10 wt%) electrodes.	86

ABSTRACT

Si-based anodes have been investigated to improve the energy density of Li-ion batteries due to their high volumetric capacity. However, huge volume changes of Si-based materials can cause severe particle fracture, leading to cell fade. Good binders for Si-based electrodes are expected to inhibit particle disconnection during cycling and simultaneously enhance cell performance.

This work comprises several binder projects of interest for Si-based materials. For instance, how to improve the Si-alloy cell cycling performance by either chemical or rheological means. Then a feasible way to study the alloy electrode fading mechanism via SEM imaging was investigated. Some new binder systems such as molecular binders and inorganic binders for Si-alloy electrodes were also explored. Finally, future work is introduced.

As a result of this work, new insights into alloy fade and completely new binder chemistries were discovered. This suggests many new directions in Si-alloy anode research for improving electrode performance.

LIST OF ABBREVIATIONS AND SYMBOLS USED

BMF	Polyethylene blown microfiber
BSE	Backscattered electron
CA	Citric acid
CB	Carbon black
CE	Coulombic efficiency
CMC	Carboxymethyl cellulose/Sodium carboxymethyl cellulose
CP	Cross-section polisher
DEC	Diethyl carbonate
DMC	Dimethyl carbonate
DS	Degree of substitution
EC	Ethylene carbonate
EDS	Energy dispersive X-ray spectroscopy
EMC	Ethylmethyl carbonate
EV	Electric vehicle
FEC	Fluoroethylene carbonate
FEG	Field emission gun
FTIR	Fourier transform infrared spectroscopy
GC	Glycol chitosan
HOMO	Highest occupied molecular orbital
ICE	Initial coulombic efficiency
IRC	Irreversible capacity
LCO	LiCoO ₂

LIBs	Lithium-ion batteries
LiPAA	Lithium polyacrylate
LMO	LiMn_2O_4
LTO	$\text{Li}_4\text{Ti}_5\text{O}_{12}$
LUMO	Lowest unoccupied molecular orbital
M_n	Number average molecular weight
M_v	Viscosity average molecular weight
M_w	Weight average molecular weight
MW	Molecular weight
NaCA	Sodium citrate
NaPAA	Sodium polyacrylate
NMC	$\text{LiNi}_x\text{Mn}_y\text{Co}_{1-x-y}\text{O}_2$
NMP	1-Methyl-2-pyrrolidinone
PC	Propylene carbonate
PE	Portable electronic
PG	Propylene glycol
PI	Polyimide
PTFE	Polytetrafluoroethylene
PVA	Polyvinyl alcohol
PVDF	Poly(vinylidene fluoride)
RC	Reversible capacity
SEI	Solid electrolyte interphase
SEM	Scanning electron microscope

TGA	Thermogravimetric analysis
VC	Vinylene carbonate
XPS	X-ray photoelectron spectroscopy

ACKNOWLEDGEMENTS

First of all, I would like to thank my supervisor, Dr. Mark Obrovac. Over the past three years, he has been an extremely patient mentor that always giving support and encouragement. He has taught me a lot about paying attention to the details about experimental result analyses and manuscript writing. I have learned not only scientific methods and strategies to solve the experimental problems, but also expressive skills to clearly present theories and results to the audiences.

I would like to thank my committee member, Dr. Josef Zwanziger, for his advice about my projects. I would also like to thank all members of the Obrovac lab, I really appreciate their help. Particularly, I would like to thank Tim for letting every experimental facility run smoothly. I would also like to thank Lea Gawne for the reminders about every deadline.

Finally, I would like to thank my parents for their consistent understanding, love, and support.

Chapter 1 INTRODUCTION

1.1 Background

Considering the supply limitations and carbon dioxide emissions of conventional fossil fuels, renewable energies are being implemented to develop sustainable and green energy sources.¹ However, renewable energy systems such as wind energy and solar power are not constant nor reliable power sources. Batteries can be used to store the energy produced by these intermittent energy systems and to enable them to be used more efficiently.² Li-ion batteries are the most promising candidate for energy storage among various battery technologies because they have many advantages, including higher operating potential, longer cycle life, and higher specific energy density, compared to other secondary battery systems such as lead acid batteries and nickel-cadmium batteries. Sony Corporation first launched LiCoO_2 (LCO)/C Li-ion cells commercially in June 1991.³ After the development over the last 28 years, Li-ion batteries are the most widely used batteries in portable electronics (PE), electric vehicles (EV), and stationary energy storage systems.² Compared to the very first version, the energy density of modern Li-ion batteries is much larger and they are about ten times less expensive. Nevertheless, the pursuit of better battery performance drives electrochemists to further improve battery energy density, cycle life, rate capability and safety; while simultaneously lowering cost.⁴

A lithium-ion cell has three main components: a cathode, an anode, and an electrolyte. For the purposes of this thesis, a cell refers to a basic 2-electrode electrochemical device, while a battery refers to a collection cells connected in series or in parallel. Figure 1.1 shows a schematic diagram of a typical lithium ion cell with an LCO cathode and a graphite anode during the charging process. During charging, an externally

applied potential causes electrons to pass from the cathode to the anode via the external circuit. This causes the cathode release lithium ions, which move to the anode via the electrolyte, to balance the charge. As the potential difference between the cathode and the anode becomes larger, the Li-ion cell stores more energy. When the cell is discharging, the electrochemical processes happen in reverse. Lithium ions flow to the cathode, where its electrochemical potential is lower than that at the anode. The electrons are then forced through the external circuit to balance the charge and may be used to provide electrical work.

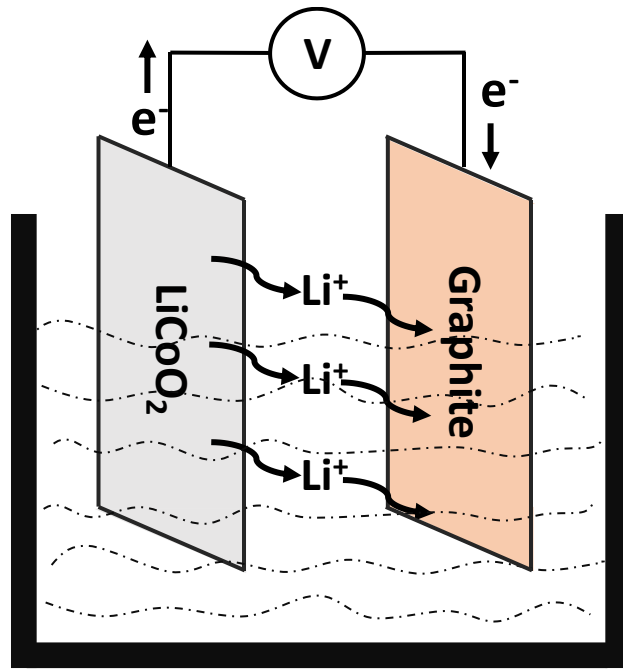


Figure 1.1 Schematic diagram of an LCO cathode (on aluminum foil) vs. graphite anode (on copper foil) lithium ion cell showing the direction the electrons and lithium ions flow during the charging process.

During cell operation, the potential difference between cathode and anode is

$$V_c = V_{cathode} - V_{anode} \quad (1.1)$$

where $V_{cathode}$ and V_{anode} are the potentials of the cathode and anode vs. Li/Li^+ , respectively.

Cell energy (E_c) is related to both the cell potential (V_c) and capacity (C_c), according to:

$$E_c = \int V_c * dC_c \quad (1.2)$$

Where C_c is integrated over the actual capacity that a cell can provide before becoming fully discharged.⁵ Thus, the most feasible methods to increase cell energy density involve increasing the working potential and developing materials possessing higher capacity.³ Two types of capacity, volumetric capacity and gravimetric (specific) capacity, are used depending on specific cases. Volumetric capacity is more important than gravimetric capacity considering the cell volumetric energy is more meaningful for applications such as portable devices and EVs, where space is more precious than weight.⁶

1.1.1 Cathodes

Present cathode materials in common use are lithium transition metal oxides such as LCO, LiMn_2O_4 (LMO), and $\text{LiNi}_x\text{Mn}_y\text{Co}_{1-x-y}\text{O}_2$ (NMC).⁴ LCO is the most popular cathode in commercial cells, because it has high volumetric capacity (1363 Ah/L), high discharge potential (~ 3.9 V vs. Li/Li^+), and long cycle life.⁷ It has a theoretical capacity of 274 mAh/g, however, a maximum specific capacity of ~ 165 mAh/g can only be obtained in practical cells owing to severe capacity fade at higher potentials (greater than 4.35 V), resulting from structural degradation.⁸ As mentioned above, the most achievable ways to enhance cathode energy density are to increase the cathode working potential and to produce high capacity materials. For instance, in the case of LCO, Liu et al. improved its capacity to 190 mAh/g through lanthanum and aluminum doping to stabilize its structure at potentials up to 4.5 V.⁸

1.1.2 Anodes

Graphite has an overwhelming dominance in commercial cells. It possesses many advantages including good conductivity, good thermal stability, low volume change during cycling, high coulombic efficiency (CE), excellent rate capability, good cycle life, and is a plentiful and cheap raw material.⁹ However, the portable electronics battery industry desires volumetric energy improvements over batteries with conventional graphite anodes (719 Ah/L). Thus, anode materials with low average potential and high volumetric capacity, such as Si-based alloys (2194 Ah/L) and lithium metal (2046 Ah/L), are being explored. The greatest challenge for the utilization of Si-based negative electrodes is the huge volume expansion up to 280%¹⁰ of Si during lithiation.¹¹ The consequences of that severe volume expansion are detrimental, leading to the loss of electrical connection of active materials and thus capacity fade. Additionally, fresh surfaces are created due to the repeated fracture of Si particles, resulting in continuous electrolyte consumption, which exhausts active Li ions in the electrolyte.⁹ One of the main strategies to tackle this problem is to introduce inactive phases such as SiC, SiO, and transition metal silicides.¹²⁻¹⁷ The volume expansion of Si can be buffered by the presence of inactive components, leading to cycling performance improvement.¹⁶

1.1.3 Electrolytes

Electrolyte for Li-ion cells can be in the form of a gel, a liquid, or a solid. A typical liquid electrolyte is made up of a lithium salt (e.g. LiPF₆, LiBF₄, and LiClO₄) and a mixture of organic alkyl carbonate solvents, for instance, ethylene, diethyl, and dimethyl carbonates (EC, DEC, and DMC). Electrolyte additives can be introduced to improve the cycling

performance. Vinylene carbonate (VC) is known to be an effective electrolyte additive to improve the lifetime of graphite cells by increasing CE.^{18,19} Fluoroethylene carbonate (FEC) is considered as a standard electrolyte additive for Li-ion batteries comprising Si-based anodes because it can significantly enhance cycling performance.²⁰⁻²²

Electrolyte molecules decompose on electrode surfaces during cell cycling. Insoluble products from electrolyte decomposition deposit on the anode and form a passivating layer called the solid electrolyte interphase (SEI).²³ The SEI is believed to play a vital role in enabling the stable cycling of anode materials, especially for Si-based materials, which encounter iterative volume change during cycling. A robust SEI should evenly cover anode surfaces to protect it from direct contact with electrolyte and prevent continuous SEI formation and reformation, which consumes active lithium ions and leads to low CE.²⁴

1.1.4 Binders

Binders are usually polymers that bind active materials and the current collector together and keep particles in contact during cycling, thus the electrode mechanical and electronic integrity can be maintained (all binders introduced in this section are not electronically conductive).^{25,26} They can also serve as dispersing agents or thickeners to permit an even distribution of solid materials in electrode slurries. Additionally, binders can modify the electrode wettability and promote active Li ion transportation at active material/electrolyte interfaces.²⁷ In Si-based anodes, binders have to possess high mechanical strength to tolerate their large volume changes during cycling.²⁸

Binders can influence electrode properties via surface modification.²⁹ Binders commonly used for Si-alloy anodes, such as polyacrylic acid (PAA) and carboxymethyl cellulose (CMC), can uniformly cover and chemically bond to the surfaces of active materials, resulting in artificial SEI layers.⁹ It has been reported that during cycling, binders can be electrochemically reduced, converting carboxylic groups to lithium carboxylates and forming a protective layer.³⁰ This binder covered Si surface can suppress the reduction of carbonate solvents in cells by generating a thin and stable SEI.³⁰ Binders can also improve cycling at the cathode. For instance, Park et al. demonstrated that an LCO cathode can cycle well at a high potential, up to 4.4 V, encapsulating LCO with a highly-continuous polyimide (PI) gel layer.^{31,32}

1.2 Organic Binders

Organic binders introduced here can be divided into two main categories: functionalized binders and unfunctionalized binders.

1.2.1 Unfunctionalized Polymeric Binders

In state-of-the-art Li-ion batteries, unfunctionalized polymer binders such polyvinylidene fluoride (PVDF) and styrene-butadiene rubber (SBR) are widely used in cathode and carbon-based anodes.³³⁻³⁵ During the coating making process, these binders wet the electrode surface and then are hardened by heating.²⁷ They can mechanically hold active materials and conductive carbons together while not forming direct bonds with them.^{26,29}

PVDF is a popular choice for cathode binder in commercial Li-ion batteries, due to its high chemical, physical and thermal stability.²⁷ However, it cannot support cycling of

high volumetric capacity materials (i.e., Si, Si alloys) because it only binds to materials with weak Van der Waals forces.³⁶ A report shows that when PVDF is used as a binder for a pure Si anode at room temperature, only the first discharge capacity is observed due to the destruction of electrode integrity by Si expansion. Little charge capacity can be seen because of the loss of electrical connections between Si particles resulting from Li-Si alloy contraction during delithiation.³⁷ However, heat treatment of PVDF can improve the performance of PVDF-Si electrodes.³⁸ The improvement could be attributed to PVDF and conductive carbon redistributing to form a continuous coating on Si and the Cu substrate surface when PVDF melts at 300 °C.³⁸ However, the cycling performance of this electrode is still relatively poor. The biggest drawback of PVDF binders is the requirement of using a toxic organic solvent, NMP, to cast homogenous films.³⁹ Both PVDF and NMP are expensive and are not easy to recycle.⁴⁰ The industrial cost of PVDF polymer in multi-ton scale is around \$17-20/kg.⁴¹ The cost of NMP solvent is \$1.21/kg,⁴² however much more NMP is used than binder (~ 25× as much). If the cost of NMP recovery is included, the electrode processing cost will be larger than aqueous processing because the cost of evaporating and condensing slurry solvent rises due to the higher boiling point and lower vapor pressure of NMP.⁴² In addition, PVDF swells in battery electrolyte, which leads to the isolation of active materials and thus poor adhesion and poor cycling performance.^{43,44}

Polytetrafluoroethylene (PTFE) is also employed as a binder for Li-ion battery cathodes. It is typically available as an emulsion in water, thus the environmentally unfriendly NMP solvent can be avoided. Like PVDF, PTFE also has high thermal, chemical, and electrochemical stability. Though PTFE has many advantages, it is still not the binder of choice for commercial cell makers, since the high pH of aqueous lithium metal oxide

slurries contributes to serious aluminum current collector corrosion during electrode manufacturing.⁴⁵ PTFE cannot serve as a binder for high energy density materials, such as Si-based alloys, either because it is unfunctionalized.

Styrene butadiene rubber (SBR) is a copolymer of styrene and butadiene. Its properties are highly dependent on the ratio of these components. SBR is commercially available as an aqueous emulsion. In Li-ion cells, SBR can improve adhesion to current collectors and help increase electrode cycle life.⁴⁶ It is an elastomeric polymer with large breakage elongation⁴⁶ and has been regarded as the primary binder for LiFePO₄ cathode with CMC used additionally as a thickening agent.⁴⁷ In the case of graphite, SBR-CMC binders can also ameliorate the dispersion stability of graphite suspensions, resulting in improved rate capability and higher specific capacity of graphite electrodes, compared to graphite electrodes made from unstable graphite suspensions with CMC alone.⁴⁸ For Si-alloy based anodes, SBR is still jointly used with stiff functionalized CMC binder to control the elasticity of the electrode film and thus facilitate the fabrication process.⁴⁹

Table 1.1 Chemical structures of unfunctionalized polymers.

$\text{--}[\text{CH}_2\text{--CF}_2]\text{--}_n$	$\text{--}[\text{CF}_2\text{--CF}_2]\text{--}_n$	$\text{--}[(\text{CH}_2\text{--CH=CH--CH}_2)_m\text{--CH}(\text{C}_6\text{H}_5)\text{--CH}_2]\text{--}_n$
Polyvinylidene fluoride (PVDF)	Polytetrafluoroethylene (PTFE)	Styrene-butadiene rubber (SBR)

1.2.2 Functionalized Polymeric Binders

Unfunctionalized polymeric binders do not result in good cycling performance when used for electrodes with high volumetric density materials such as Si and Si-based

alloys. Thus, functionalized polymers are used to tackle this problem. Polymeric binders containing carboxyl groups can chemically bond with hydroxyl groups on the natural surface of Si and the treated surface of Cu foil, forming strong ester-like covalent bonds and weaker hydrogen bonds.⁹ This chemical bonding can help maintain the mechanical and electrical integrity of electrodes containing high volumetric density materials during repeated cycling,²⁷ thus long cycle life of cells are attainable.

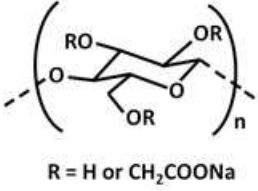
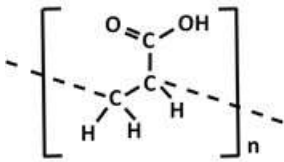
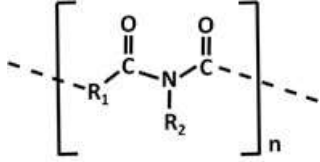
Sodium carboxymethyl cellulose (CMC) is produced by the insertion of carboxymethyl groups in natural cellulose,⁵⁰ it is usually preserved as a sodium salt due to the poor water solubility of its acid form. CMC is now a common binder used for Li-ion anodes and is of interest because of its water solubility and low cost of \$1-2/kg.⁴¹ CMC is stiff and brittle,³⁸ which is a disadvantage in the fabrication process of wound cells. Therefore, as mentioned above, CMC is typically used in combination with the highly elastic SBR binder in industry. The mechanical properties of CMC are dependent on its molecular weight (MW), which influences the solubility and viscosity of its water solutions.⁵¹ It is widely accepted that the binder functional group density can significantly influence the cycling of electrodes containing Si-based materials. A higher content of carboxylic groups in binders are supposed to contribute to a larger number of binder-Si bonds and thus result in improved cycling performance.⁵² Therefore, the degree of substitution (DS), which indicates the average number of carboxymethyl groups per monomer unit,⁵³ matters when CMC serves as binder in cells. DS values vary from 0.2 to 3 for CMC, and for battery applications range from 0.6 to 1.4.⁵¹

Polyacrylic acid (PAA) has been considered as a binder for Si-based electrodes for the last decade.⁵⁴ Like CMC, PAA is also water-soluble. The cycling performance of PAA-

Si electrodes surpasses that of CMC-Si electrodes due to the higher density of carboxylic groups moieties in PAA.⁵⁵ Another explanation for the better performance of PAA electrodes is that PAA is stiffer than NaCMC, the stiff mechanical property leading to a spring like conformation which helps maintain the electronic percolation network during cycling.⁵⁶ However, it is still not utilized commercially. The key challenge for application of PAA binders in practice is its superhydrophilicity in air, which results in the introduction of moisture into cells and causes electrodes to curl during the drying process. Water solubility is an environmental advantage, however, water can react with Si nanoparticles to form hydrogen and silicon oxide.³⁰ The surface oxidation of Si affects the CE and cycle life of Si materials.⁵⁴

Polyimide (PI) is of interest as a binder for anodes in LIBs due to its superior mechanical properties.⁵⁷ It is produced by imidization reaction of poly(amic acid) at high temperature (250-400 °C). There are two types of PI, aromatic PI (aro-PI) and aliphatic PI (ali-PI), both can adhere to and uniformly cover substrate surfaces. However, only aro-PI is electrochemically active and can make alloy electrodes cycle well. The reason for good cycling of aro-PI is suspected to be because it decomposes to form conductive hydrogen-containing carbons during lithiation.⁵⁸ Unfortunately this reaction consumes lithium, resulting in high irreversible capacity. Moreover, its high price and the required use of NMP solvent also limit its utilization in industry.

Table 1.2 Chemical structures of functionalized polymers.

		
<p>Sodium carboxymethyl cellulose (CMC)</p>	<p>Polyacrylic acid (PAA)</p>	<p>Polyimide (PI)</p>

1.3 Optimization of Organic Binders in Cells

The behavior of a binder on Si-based anodes can be impacted by many factors, such as their acidity, molecular weight, and structure. Much effort has been devoted to optimizing these characteristics to achieve excellent cell performance and long cycle life. The acidity of a polymeric binder can affect the function of all electrode components, including current collectors, active materials, and the binder itself. For instance, Doberdò et al. showed that the high pH value of a CMC aqueous electrode slurry contributes to serious aluminum foil corrosion during NMC cathode manufacturing.⁴⁵ Nguyen et al. reported that the surface oxidation degree of Si nanoparticles is dependent on the pH value of the binder solution.³⁰ It was observed that a higher pH of CMC and PAA binder leads to a greater intensity X-ray photoelectron spectroscopy (XPS) SiO_x peaks for Si-CMC and Si-PAA electrodes. The generation of a thick silicon oxide layer on the Si surface likely results in poor cycling performance.³⁰ For the binder itself, a strong acid or alkali environment is a common cause of binder degradation. However, binder degradation, such as molecular weight reduction, is difficult to observe or measure in cells. A commonly

discussed characteristic of a binder with different pH values is its distribution on specific substrates. Pejovnik et al. showed the surface distribution of gelatin binder on the surface of a highly oriented pyrolytic graphite. It was found that at pH 12, gelatin has a much smaller thickness (several nm) compared to the thickness of gelatin at pH 9 (up to 200 nm).²⁹ A higher pH of gelatin is more extended and less polarized, which results in better coverage on the surface of graphite and thus better cell performance. This conclusion has been confirmed by other studies that show that functionalized polymers such as CMC and PAA are agglomerated at low pH owing to intermolecular hydrogen bonds between the carboxylic side groups and are extended at higher pH due to the electrostatic repulsion between carboxylate groups.⁵⁹

The molecular weight (MW) of polymeric binders affects the rheological properties of slurry, the electronic conductivity, the mechanical properties such as adhesive strength, solubility, swellability, thermal stability, and the final electrochemical performance of electrodes.^{54,60} The molecular weight of a synthetic polymer does not have a single value. There is always a molecular weight distribution around an average value for a given polymer species. The most frequently used molecular weight average are M_n (number average molecular weight), M_w (weight average molecular weight), and M_v (viscosity average molecular weight). Number average molecular weight is defined as the total weight of polymer divided by the total number of molecules.

$$M_n = \frac{\sum M_i N_i}{\sum N_i} \quad (1.3)$$

Where N_i is the number of molecules having molecular weight M_i . Weight average molecular weight is calculated by the sum of the product of the weight fraction W_i and molecular weight of each type of molecules.

$$M_w = \sum W_i M_i = \frac{\sum M_i^2 N_i}{\sum M_i N_i} \quad (1.4)$$

Viscosity average can be determined from the Mark-Houwink-Sakarada (M-H-S) equation, which describes the relation between intrinsic viscosity $[\eta]$ and M_v .

$$[\eta] = K M_v^a \quad (1.5)$$

Where K and a are constants dependent on the polymer-solvent system. Then M_v can be calculated by

$$M_v = \left[\frac{\sum M_i^{1+a} N_i}{\sum M_i N_i} \right]^{\frac{1}{a}} \quad (1.6)$$

Many studies have been done to determine the optimal MW for specific cases. For example, Lee et al. tried five different types of CMC (from 90k to 700k) binders for $\text{Li}_4\text{Ti}_5\text{O}_{12}$ (LTO) electrodes to figure out how MW influences coating preparation and electrode cycling performance.⁵³ It turned out that as MW decreases, the electrolyte wettability and ionic conductivity of CMC binder increases because of more facile vibration of polymer backbones, while both adhesion strength and interaction between CMC and LTO decreases due to the lower surface coverage of CMC on LTO surfaces. Hu et al. tested a series of LiPAA binders in a wide MW range (from 2 kDa to 450 kDa) on a Si/graphite anode. They found that M_n from 24 to 150 kDa is optimum for maintaining the cohesion of active materials and enables the stable cycling of cells over 100 cycles. LiPAAs with MW < 24 kDa performed poorly due to the loss of ester bonding between the polymer chains and siloxyl groups.⁶¹

The architecture of binders can also affect cell performance. Branched polymers tend to obstruct external forces through interchain interactions. The multidimensional

contacts provided by branched polymers can offer more robust binding forces with active materials by productively accommodating the huge change of Si particles during cycling than linear-chain polymers.^{27,62,63} For instance, Song et al. prepared a type of interpenetrated PAA-polyvinyl alcohol (PVA) superabsorbent gel binder for a Si/graphite anode. The resulting electrode showed enhanced cycling stability and a higher CE compared to electrodes with NaCMC binders alone.⁶⁴ Cao et al. synthesized a graft block copolymer GC-g-LiPAA (glycol chitosan backbone and lithium polyacrylate side chains) as a binder for a Si/graphite anode. They noticed that the graft copolymer had an improved capacity retention and a higher CE than a physically mixed linear GC and LiPAA polymers at the same composition due to its vigorous adhesion on Si particles.

1.4 Inorganic Binders

Inorganic binders are also of interest in LIBs. Compared with widely used organic polymeric binders, inorganic binders possess the advantage of high electrochemical and thermal stability and can tolerate the high temperature during the drying process. To avoid the decomposition of organic binders in drying steps, electrode coatings have to be heated at temperatures significantly below the onset of binder decomposition, leading to the incomplete removal of NMP or water solvents. Residual water in electrodes is likely to cause detrimental side reactions such as the liberation of HF from the LiPF₆ electrolyte salt. Additionally, inorganic binders are usually insoluble in organic solvents. Therefore, there is no concern about binders aging or the loss of association with active materials and current collectors due to their volume expansion resulting from electrolyte absorption. So far, the use of inorganic binders for alloy anodes has not been reported.

Some silicate and phosphate binders were studied in this thesis. Silicates are compounds with various ratios of silicon dioxide and alkali metal oxide. Soluble silicates may react with silicon fluorides or silica to produce acid-resistant cement. Sodium silicate, commonly called “water glass”, is mainly used as the cement for papers, corrugated cardboard, wood, stoneware, etc.⁶⁵ It can withstand temperatures up to 1100 °C.⁶⁵ Lithium polysilicate was used as binder in LIBs (LCO cathodes and graphite anodes) about two decades ago, the cells show stable cycling.⁶⁶ Both lithium and sodium phosphate binders have been tested as the binders in $\text{LiMn}_{0.8}\text{Fe}_{0.2}\text{PO}_4$ cathodes, resulting in good cycling performance with high capacity retention and good rate capability.⁶⁷

1.5 Motivation

To date, most of the research in the battery field focuses on the development of active materials and electrolytes. Less attention has been paid to explore new binder systems or understand binder function in cells. Throughout this thesis, efforts have been expended to investigate some binder systems of interest.

Chapter 1 gives an overview of Li-ion cells, mainly concentrating on the binder systems used in cells. Chapter 2 introduces the experimental tools used in this study. Chapter 3 shows how to use small functional molecules as slurry additives to improve the cycling of anodes containing Si-alloy. Chapter 4 explores the effect of sodium polyacrylate (NaPAA) binder molecular weight on performance of Si-alloy anodes. Chapter 5 introduces the use of small organic functional molecules as binders for Si-alloy anodes instead of the commonly used functionalized polymeric binders. Chapter 6 shows how Si-alloy particle

degradation depends on the binder. Chapter 7 describes the performance of Si-alloy and graphite anodes with inorganic binders.

Chapter 2 EXPERIMENTAL SECTION

2.1 Electrochemical Cells

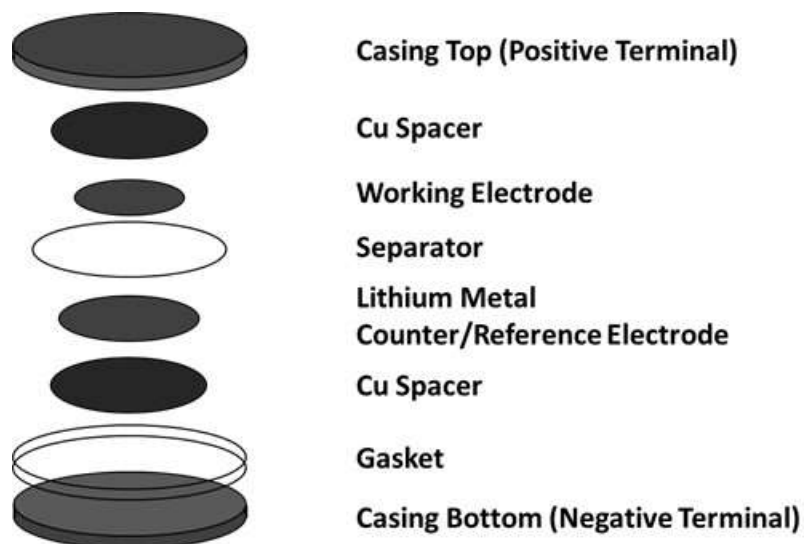


Figure 2.1 An exploded view of a coin cell.

Coin cells were used for all projects in this thesis. Figure 2.1 shows an exploded view of a coin cell. To prepare coin cell electrodes, first a slurry with a mixture of active materials, conductive carbons (may not include), and binders was prepared. Different component ratios were used, depending on the project. The electrode slurry was mixed using a planetary mill (Retsch PM200) at 100 rpm for 1 hour with three 0.5-inch tungsten carbide balls or by using a Mazerustar mixer at 5000 rpm for 10 mins. Mixed slurries were spread onto a piece of 15 μm thick copper foil (Furukawa) with a coating bar having a 0.004-inch gap. The coating was dried for 1h at 120°C in air. Electrode disks with an area of 1.30 cm^2 were punched from the coating after drying and heated under vacuum at 120°C overnight before cell making. Coin cell assembly was conducted in an argon-filled glovebox. 2325 coin cells were made with a working electrode versus Li metal foil (99.9%, trace metals basis, Sigma-Aldrich) (as the counter/reference electrode). The electrolyte used was 1M LiPF_6 (battery grade from BASF) dissolved in a solvent mixture of ethylene

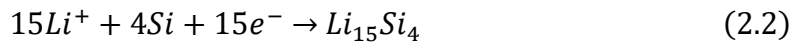
carbonate: diethyl carbonate: fluoroethylene carbonate (EC:DEC:FEC, all battery grade from BASF) in a volume ratio of 3:6:1. Two layers of Celgard-2301 and one layer of BMF (polypropylene blown microfiber separator, ~190 μm thick, from 3M Company) were used as separators. Each coin cell contains two Cu spacers to guarantee proper internal pressure.

2.2 Electrochemical Measurements

Galvanostatic cycling was used to analyze the electrochemical performance of coin cells. During galvanostatic charge and discharge of a cell, the current is often expressed as a C-rate, the value is calculated from the battery theoretical capacity Q , which is

$$Q = z * \frac{F}{M} \quad (2.1)$$

where z is the number of electrons transferred in the reaction, F is the Faraday constant, and M is the molecular mass of the active material. Silicon is chosen as an example in this theoretical capacity calculation, the reaction occurring during the cell discharge is



The fully lithiated phase for Si at room temperature is $\text{Li}_{15}\text{Si}_4$,⁶⁸ its theoretical capacity is

$$Q = \frac{15}{4} * \frac{26802 \text{ mAh/mol}}{28.08 \text{ g/mol}} = 3579 \text{ mAh/g} \quad (2.3)$$

1C means the necessary current is applied on a cell to completely charge or discharge an electrode in one hour. In this thesis, the typical cycling current is C/5, which means that it takes 5 hours to completely charge or discharge a coin cell, theoretically. Potential vs. capacity curves are used to express how cell potential changes as the capacity is changed.

Figure 2.2 shows the first cycle potential vs. capacity curve of a Si-alloy electrode. The lithiation curve comprises a small plateau at about 0.18 V, which is likely due to the

nucleation and growth of new Li_xSi phases during the initial lithiation,^{15,69,70} followed by two characteristic sloping plateaus of Si-alloy, indicating that the Si phase in the alloy remained amorphous during cycling.^{11,16}

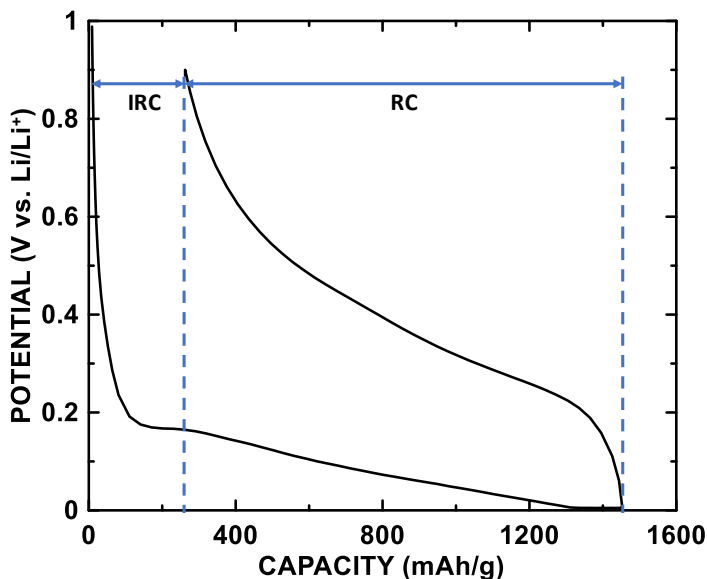


Figure 2.2 First cycle potential vs. capacity curve of a Si-alloy electrode. Reversible and irreversible capacities during the initial lithiation process are shown as indicated.

Some electrochemical concepts used to describe the performance of a cell are capacity retention, reversible/irreversible capacity (RC/IRC), and coulombic efficiency (CE). Capacity retention is the fraction of a cell's capacity left after it has been cycled for a period of time. Capacity losses of a cell can be reversible or irreversible.⁷¹ Reversible capacity loss is known as self-discharge and can be reversed by charging whereas irreversible capacity loss is known as capacity fade,⁷¹ which usually comes from the destruction of active materials or the consumption of active Li ions due to electrolyte decomposition to form SEI. CE is used to describe the charge transfer efficiency in an electrochemical reaction, which is the ratio of discharge capacity to charge capacity.

Electrochemical testing of coin cells was performed using a Maccor Series 4000 Automated Test System. Cells were cycled with potential limits of 0.005 V and 0.9 V for

the first two cycles with a C/10 and a C/40 trickle discharge at 0.005 V and the following cycles with a rate of C/5 and a C/20 trickle discharge at 0.005 V.

2.3 Ion Milling

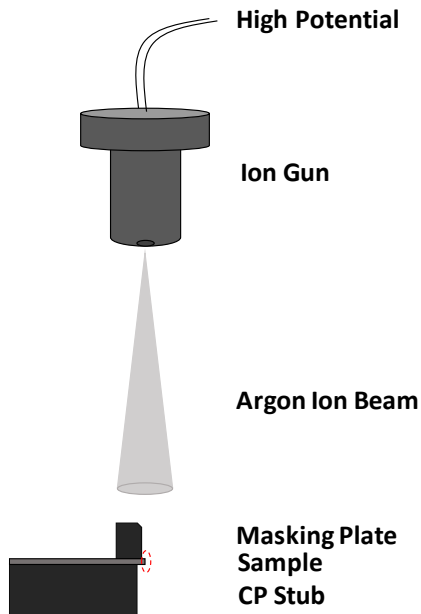


Figure 2.3 A schematic diagram showing the working principle of a cross-section polisher (CP). A sample is placed in the beam path of a stationary broad argon beam. The area in the dashed red circle represents the sample protruding from the edge of the masking plate.

Ion milling is a physical etching technique using a high-energy argon ion beam to remove materials from a sample surface. In this thesis, a JEOL IB-19530CP Cross Section Polisher (CP) was used to prepare smooth cross-sections of specimens. Figure 2.3 shows a schematic diagram of the CP working principle. In the CP, an argon ion beam is emitted from a ion gun, perpendicular to the sample, which is partially covered with a shielding plate (masking plate), the beam cuts the sample along the border of the masking plate and only the area of the sample protruding from the edge of the masking plate is milled away.

There are three main parameters that can be adjusted in a CP during the cutting process: the working potential (0-8 kV), the argon gas flow, and the cutting time. The argon flow affects the argon ion beam current. There is a stable argon gas region (70-80% of the maximum) for a given cutting potential. Both insufficient and excess gas flow can make the cutting beam unstable. Generally, a lower potential requires a higher argon gas flow. Cut width and removal rate are determined by the potential. A higher potential gives a wider cut and a faster removal rate. Cut depth is determined by both time and materials type, a longer time leads to a deeper cut for the same type of sample.

In this thesis, all samples were cross-sectioned at 6 kV with an argon gas flow of 5.5 (a unitless machine setting).

2.4 Scanning Electron Microscopy and Energy Dispersive X-ray Spectroscopy

A scanning electron microscope (SEM) creates images of a sample by scanning the sample surface with a focused beam of electrons. By using electrons as the beam source, SEM resolution is significantly better than a conventional light microscope because electrons possess much shorter wavelengths, at picometer levels.

When an electron beam with high energy interacts with a sample in SEM, both elastic and inelastic scattering can occur. This results in the production of secondary electrons, backscattered electrons, and characteristic X-rays, depending on the penetration depth in the sample during the sample-electron interaction. Signals from all three processes can be detected and used to acquire information about surface topography and sample composition. Both secondary electrons and backscattered electrons are frequently used for imaging by SEM users. Secondary electrons originate from the surface or the near-surface

regions of the sample due to inelastic interactions between the sample and the primary electron beam. They are very beneficial for the observation of the topography of the sample surface. Backscattered electrons originate from a broader and deeper region within the interaction volume due to the elastic collision of electrons with atoms, leading to a change in the trajectory of electrons. Compared to light atoms, larger atoms backscatter electrons more strongly, and thus they are brighter in the image. Therefore, brightness in backscattered electron images can convey information on the composition of a sample. Characteristic X-rays are also emitted from the sample during its interaction with the incident electron beam. When the inner shell electrons of an atom are excited by primary electrons and ejected from the atom, the outer shell electrons will fill the vacancy, emitting X-ray photons at the same time. Those X-rays produced are characteristic for elements due to their distinct configurations, thus can be used for element analysis with a technique called energy dispersive X-ray spectroscopy (EDS).

In this thesis, a TESCAN MIRA 3 LMU Variable Pressure Schottky Field Emission Scanning Electron Microscope (FE-SEM) was used to acquire SEM images. FE-SEM is a type of SEM using field-emission electron gun (FEG). In Schottky FEG, a wire of tungsten with a very sharp tip coated with a layer of zirconium oxide, less than 100 nm, emits electrons within a strong electric field. Compared with a traditional thermionic emission electron gun, which emits electrons by heating a tungsten filament to a high temperature, FEG can produce an electron beam with a small energy spread, small beam current and high brightness, up to 10^7 to 10^8 , resulting in significantly improved signal-to-noise ratio and resolution. All samples for observation in SEM were prepared by ion milling in this

study. All SEM images, including SE and BSE images, were acquired at an accelerating potential of 5 kV.

2.5 Thermogravimetric Analysis

Thermogravimetric analysis (TGA) is a type of thermal analysis method used to characterize the thermal properties of materials. TGA can continuously monitor the mass of a sample when the sample is heated under a programmed temperature rise in a specific atmosphere (air, argon or helium). This measurement can convey information about both physical and chemical properties of a sample such as phase transitions, adsorption, desorption, thermal decomposition and oxidation/reduction in different gases. In this study, TGA was carried out using a TA Instrument SDT Q600 with a dried air flow of 150 mL/min from room temperature to 400 °C with a heating rate of 1 °C/min to confirm that propylene glycol (PG) can be removed entirely by heating when PG is used as a solvent for electrode slurries.

Chapter 3 SMALL FUNCTIONAL MOLECULES AS SLURRY ADDITIVES FOR SI-ALLOY COATINGS WITH CMC/SBR BINDER

3.1 Introduction

As mentioned in Chapter 1, good cycle life has been obtained for Si alloys if functional binders, such as polyacrylic acid (PAA)⁵⁴ and carboxymethyl cellulose (CMC)⁷² are used. These functional polymeric binders containing carboxyl groups can interact with alloy and copper foil surfaces via strong ester-like covalent bonds and weaker hydrogen bonds.⁵⁴ Hydrogen bonding is well-known to be responsible for the “self-healing” effect that contributes to maintain association between particles even after rupture.⁷³ Aromatic binders, like PI, represent another class of high performance binders for alloy electrodes.⁴ Such binders can decompose during lithiation, forming a conductive carbon network, leading to good cycling.⁵⁸ Though cycling performance of PAA and PI electrodes surpass those using CMC binder, they are not the binders of choice for Li-ion cell makers at the present stage. PAA binder suffers from its superhydrophilicity in air. In the case of PI, its high cost and the use of NMP as a required solvent restrict its implementation.

In addition to polymeric binders, small organic compounds have also shown to be effective binders for Si electrodes. For instance, citric acid (CA) has been added in Si electrode slurry as a pH buffer^{46,74} or used directly used as binder.^{75,76} Electrodes containing citric acid displayed better capacity retention than those using PAA binders. Nguyen et al. mentioned that small molecules like CA could modify the surface of Si, resulting in the superior performance, even though CA does not provide strong mechanical or adhesion strength.⁷⁵

Since CMC/SBR binders are already used in graphite electrodes for commercial cells, it would be highly advantageous if such binders could be made effective for use also with Si-alloy containing electrodes. In this study we explore the use of small molecule slurry additives for improving the performance of CMC/SBR binders in Si-alloy electrodes. Some additives were found to be highly effective, resulting in Si electrodes with CMC/SBR binder having superior performance to those with PAA binder.

3.2 Experimental

Baseline electrode coatings were prepared by mixing Si alloy powder (3M L-20772 V7 Si alloy, hereafter called V7, from 3M Co., St. Paul, MN), graphite, including MAGE (Hitachi, 20 μm average size) and KS6 (Timcal), carbon black (CB, C-ENERGY Super C65, Timcal), a 5 wt% aqueous solution of sodium carboxymethyl cellulose (CMC), prepared from distilled water and CMC powder (average $M_w \sim 90,000$, Sigma-Aldrich), and styrene butadiene rubber (SBR, 50 wt% emulsion in water, MTI Corp.) in a 30:59:5:2:2:2 V7/MAGE/KS6/CB/CMC/SBR weight ratio. Small organic functional molecules used as slurry additives included sodium acetate (fused-anhydrous, Fisher Scientific Company), trisodium citrate dihydrate (99%, Alfa Aesar), sodium mellitate (prepared by neutralizing a solution of 10 wt% mellitic acid (99%, Aldrich) in distilled water with 1M NaOH (reagent grade, $\geq 98\%$, Sigma-Aldrich), sodium hydrogen L-tartrate (anhydrous, 98%, Alfa Aesar), disodium terephthalate (99+%, Alfa Aesar), pyromellitic acid (96%, Alfa Aesar), and poly(acrylic acid, sodium salt) (average $M_w \sim 1,200$, 45 wt% in H_2O , Aldrich). These additives were added to the baseline coating slurry formulation in an amount of 5 wt% of the total slurry weight. All slurries were mixed using distilled water as solvent in a

planetary mill (Retsch PM200) at 100 rpm for 1 hour with three 0.5-inch tungsten carbide balls and then spread onto copper foil with a coating bar having a 0.004-inch gap. All slurries had final pH values in the range of 6.6 to 7.7. All coatings were dried for 1h at 120 °C in air. Electrode disks with an area of 1.30 cm² were punched from the coatings after drying and heated under vacuum at 120 °C overnight before cell making. The mass loading of electrodes was ~2.8 mg/cm², corresponding to a specific capacity of ~1.8 mAh/cm² (calculated based on a V7 alloy specific capacity of ~1200 mAh/g and a graphite specific capacity of 372 mAh/g).

Coin cells were assembled in an Ar-filled glove box. 2325 Coin cells were made with a working electrode versus Li metal foil (99.9%, trace metals basis, Sigma-Aldrich) (as the counter/reference electrode). Electrolyte used was 1M LiPF₆ (battery grade from BASF) dissolved in a solvent mixture of ethylene carbonate: diethyl carbonate: fluoroethylene carbonate (EC:DEC:FEC, all battery grade from BASF) in a volume ratio of 3:6:1. Two layers of Celgard-2301 and one layer of BMF (polypropylene blown microfiber separator, ~190 μm thick, from 3M Company) were used as separators. Each Li-ion cell contained two Cu spacers to guarantee proper internal pressure.

Electrochemical testing of coin cells was performed using a Maccor Series 4000 Automated Test System. Cells were cycled with potential limits of 0.005-0.9 V for the first two cycles with a C/10 and a C/40 trickle discharge at 0.005 V and following cycles with a rate of C/5 and a C/20 trickle discharge at 0.005 V. Cross-sections of electrodes before and after cycling were prepared using a cross-section polisher (JEOL, IB-19530CP). Cross section morphologies were characterized using a scanning electron microscope (SEM, TESCAN MIRA3) with an accelerating potential of 5kV. Electrodes after cycling were

opened in an Ar-filled glove box and rinsed with dimethyl carbonate (DMC, BASF) three times to remove remnant electrolyte salts. To abate air exposure, a desiccator was used to transfer cycled electrode samples to the cross-section polisher and a stream of argon gas was flowed over air-sensitive electrodes during the sample loading procedure for the cross-section polisher and SEM.

3.3 Results and Discussion

Figure 3.1 shows the molecular formula of all functional molecules tested as slurry additives in this study. NaPAA, a common polymeric binder used for Si-alloy negative electrodes, was also evaluated as a slurry additive for comparison with the molecular additives. All molecules selected for use as slurry additives contain carboxylic groups which are believed to form bonds with alloy particles and the current collector. Sodium citrate and sodium hydrogen L-tartrate contain hydroxyl groups as well, which is expected to be conducive to hydrogen bonding with each other and the CMC binder.

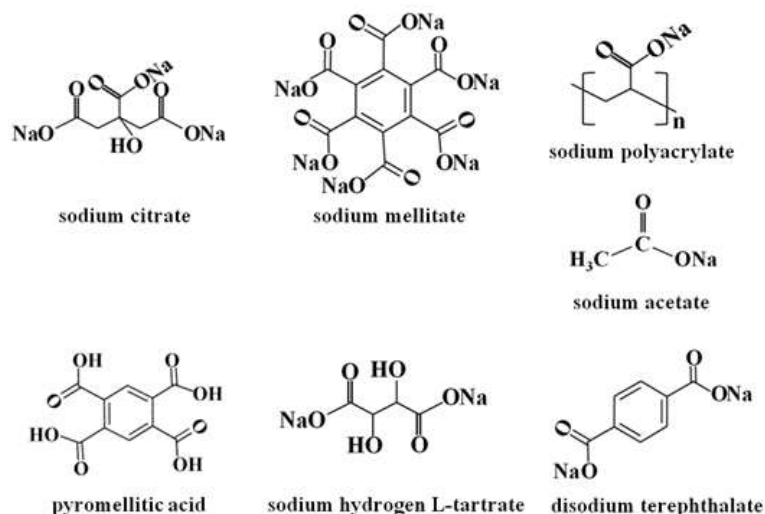


Figure 3.1 Chemical structures of the slurry additives tested. All additives contain various number of carboxyl/carboxylate groups.

Figure 3.2 shows the capacity retention and CE (from the second cycle) versus cycle number of the baseline V7/graphite-CMC/SBR electrode and electrodes including 5 wt% of different slurry additives. After 100 cycles, the baseline electrode V7/graphite-CMC/SBR retains 68.2% of its original discharge capacity. The addition of 5 wt% slurry additive to the slurry formulation has significant effects on the cycling performance of the baseline V7/graphite-CMC/SBR electrode. The capacity retention becomes significantly reduced and the CE becomes low with the addition of 5 wt% pyromellitic acid, sodium hydrogen L-tartrate, sodium acetate, and sodium terephthalate. All these additives were found to result in poor slurry/electrode properties. For instance, pyromellitic acid was found to be practically insoluble in water. Therefore, it likely acts like an insulating impurity in the coating, leading to the isolation of alloy particles and capacity fade. Sodium hydrogen L-tartrate and sodium terephthalate caused particle aggregation in the slurry, resulting in poor particle dispersion and poor quality coatings. Although the coating containing sodium acetate was found to be of good quality visually, sodium acetate likely decomposed when the coating was heated at 120°C, since the boiling point of acetic acid is 118.1 °C.

In contrast, the discharge capacity retention of the baseline V7/graphite-CMC/SBR electrode increased significantly to 84.2%, 81.1%, and 75.6% after 100 cycles with the addition of sodium mellitate, sodium citrate, and sodium polyacrylate (MW ~1,200), respectively. The CE also increased, with the average CEs (cycle 2-100) of the sodium mellitate, sodium citrate, and sodium polyacrylate electrodes, being 99.69%, 99.68%, and 99.62%, respectively, which are slightly higher than that of the baseline electrode, 99.56%. Interestingly, the molecular slurry additives improved cycling to a greater extent than

NaPAA, demonstrating that the polymeric nature of binders is not necessarily related to cycling properties. It is also interesting that all these binders have a higher content of carboxyl groups per unit mass than CMC. Indeed, the cycling performance of the electrodes correlates with the number of carboxyl groups added to the slurry; with sodium mellitate, sodium citrate, and NaPAA having 1.7, 1.6, and 1.4 times as many carboxyl groups per unit mass than CMC, respectively. Therefore, good slurry additives are likely molecules with a large amount of carboxyl groups, that maintain good slurry dispersion and whose acid form have a high boiling point, to avoid evaporation of the additive during curing.

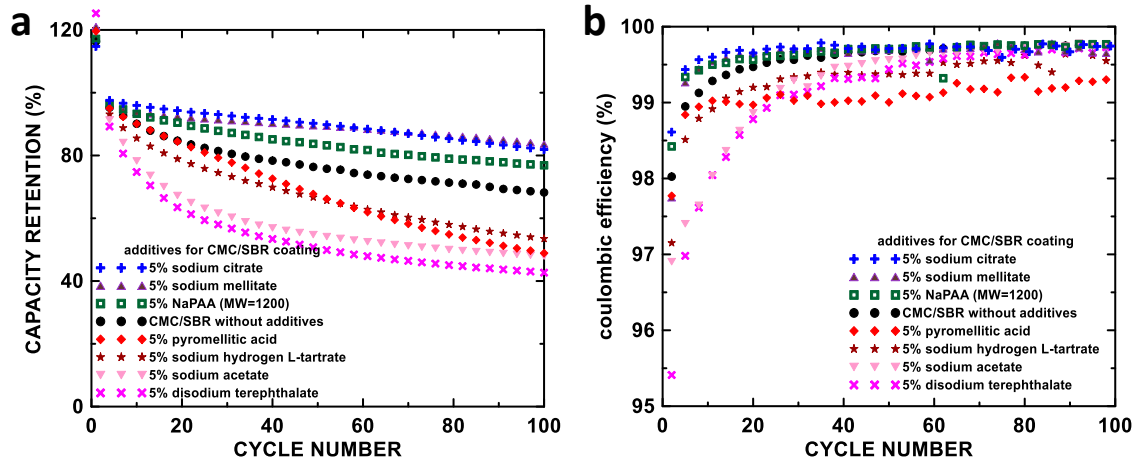


Figure 3.2 Capacity retention (a) and CE (b) vs cycle number of V7/graphite electrode and electrode prepared with different slurry additives.

Figure 3.3 shows potential vs. capacity curves of the baseline CMC/SBR electrode and electrodes with Na mellitate, Na citrate, and NaPAA additives. All cells show a combination of two characteristic sloping plateau of amorphous Si-based alloy^{16,77} and three plateaus of graphite.⁷⁸ The initial coulombic efficiency (ICE) of all the electrodes was similar, being 86%, 83%, 84%, and 87%, respectively, for the baseline and the electrodes with Na mellitate, Na citrate, and NaPAA additives. The first delithiation capacity of electrodes with Na mellitate, Na citrate, NaPAA, and without additives was 645, 617, 599,

and 652 mAh/g, respectively. This is close to the 636 mAh/g theoretical specific capacity based on the composition of the electrodes. The observed capacity variation is likely from random error in cell building/weighing of the active mass.

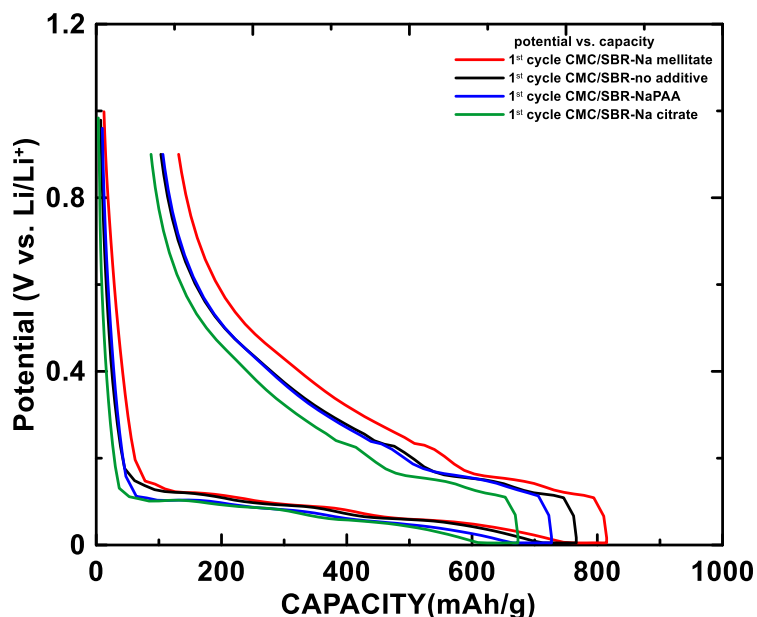


Figure 3.3 The first cycle potential vs. capacity curves of the V7/graphite-CMC/SBR electrode and electrodes with Na mellitate, Na citrate, NaPAA additives.

Electrodes using different additives were cross sectioned and SEM images were obtained using a BSE (back-scattered electron) detector, so that the morphology of the alloy particles can be clearly seen. Figure 3.4(a) shows an image of the baseline electrode prior to cycling. The pristine V7 particles are bright in the image and are present as individual primary particles and aggregated clusters, but all have distinct edges. Graphite appears as dark grey. After 100 cycles, alloy particles in the different electrodes are subjected to varying degrees of degradation, as shown in Figure 3.4(b) through 3.4(f). Cycled alloy particles have eroded and rough surfaces surrounded by grey regions, corresponding disintegrated nano-alloy particles mixed with SEI. Similar observations have been made by Krause et al.⁷⁹ In electrodes with poor cycling performance, pristine alloy particles are

still present after 100 cycles, due to their being electrically disconnected from the electrode during cycling. Figure 3.4(b) shows the cross section of the baseline electrode after 100 cycles. It contains a mixture of alloy particles with eroded surfaces and pristine alloy particles that have become disconnected during cycling. The disconnected particles are likely the cause of cell fade in this electrode. Figure 3.4(c-e) show the cross section of electrodes with sodium mellitate, sodium citrate, and NaPAA additives after 100 cycles. In these electrodes nearly all the particles are seen to have eroded surfaces, showing that they have all maintained connection with the electrode during cycling, resulting in the improved cycling performance of these electrodes. In contrast, a poorly performing additive, like sodium acetate, shown in Figure 3.4(f), results in an electrode with many uncycled, disconnected particles, corresponding to the rapid fade of this electrode.

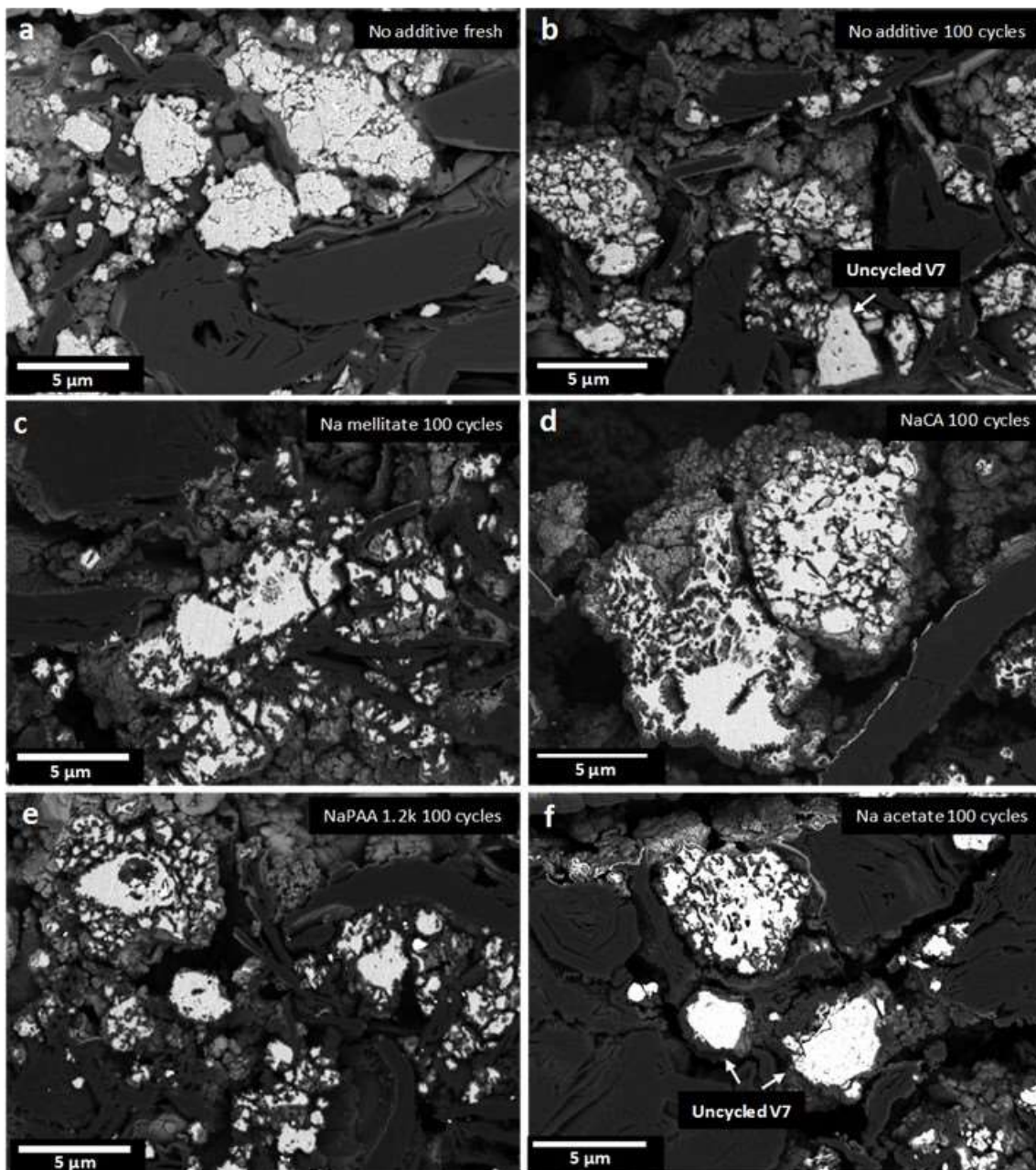


Figure 3.4 Cross sectional SEM images of Si alloy-graphite electrode. (a) Fresh electrode without additive, (b) after 100 cycles without additive, (c) after 100 cycles with Na mellitate, (d) after 100 cycles with NaCA, (e) after 100 cycles with NaPAA (1.2k), (f) after 100 cycles with Na acetate. Light grey, dark grey, and black areas correspond to V7 alloy particles, SEI layers, and graphite, respectively.

It can be seen from this study that, adding additional carboxylic acid groups to a slurry mixture can improve cycling by helping to maintain good particle connectivity to

the electrode. These slurry additives could aid cell manufacturers incorporate Si-alloy materials in their existing electrode formulations with CMC/SBR binders. However, as shown above, while such additives improve cycling performance, they do not reduce particle fracturing and erosion. Apparently, these binders work by improving alloy cycling, despite the appearance of surface erosion. This is a serious issue, since particle erosion causes the formation of new surfaces, resulting in electrolyte consumption and significant volume growth of the electrode itself. Further specialty binders, particle coatings or electrolyte additives are needed to address this issue. Alternatively, alloy particle fracture may simply be a consequence of repeated volume expansion/contraction of the alloy and may require solutions in the form of completely new materials.

3.4 Conclusion

It was found that molecules with a high density of carboxyl groups, that maintain good slurry dispersion and whose acid form have a high boiling point can be used as effective slurry additives to improve the cycle life of Si-alloy electrodes using CMC/SBR binders. In particular, the molecular additives sodium mellitate, and sodium citrate were found to be especially effective for increasing capacity retention. SEM analysis of cycled electrodes show that these additives improve cycling performance by maintaining good alloy particle connectivity to the electrode. These slurry additives could aid cell manufacturers incorporate Si-alloy materials into their existing electrode formulations with CMC/SBR binders. However, as cycling performance was improved by these additives, erosion of the alloy surface during cycling became more severe. Further specialty binders,

particle coatings or electrolyte additives are needed to address this issue. Alternatively, new materials design is needed to eliminate alloy fracture during cycling.

Chapter 4 THE EFFECT OF BINDER MOLECULAR WEIGHT ON ALLOY ANODE CYCLING PERFORMANCE

4.1 Introduction

It was mentioned in Chapter 1 and Chapter 3 that PAA is a promising binder for Si-contained anodes due to its high carboxylic group density. Such groups form strong ester-like covalent bonds and weak hydrogen bonds, which is claimed to result in a “self-healing” process during cycling.

PAA was originally used as the binder for a Si anode by Dinh Ba Le⁸⁰ in 2007, since then a lot of research has been done to optimize this system, such as the neutralization degree, of PAA binders and their alkali salts in the electrode, and to understand the mechanism of how these binders affect the cycling performance of Si-contained anodes. For example, Komaba et al. compared the effect of binders made from various alkaline (NH_4^+ , Li^+ , Na^+ , K^+) polyacrylate salts on Si-graphite electrode performance.⁵⁹ It appeared that the optimal neutralization degree of Li_xPAA , Na_xPAA and K_xPAA are 100%, 80%, and 60%, respectively. They also reported that the electrode slurry reached maximum viscosity at the optimum neutralization degree of each binder. One possible explanation for this correlation, as they stated, was related to the dispersion of neutralized PAA in the slurry. The slurry with a well dispersed binder could have a high crosslink level between binder and electrode materials, resulting in an even coverage of the binder on the electrode materials and a strong connection between them. Among these binders, $\text{Na}_{0.8}\text{PAA}$ had the best cycling performance, mainly due to the presence of sodium ions, which modified the properties of the SEI layer and the porous structure of the electrode formed by $\text{Na}_{0.8}\text{PAA}$, which could effectively buffer volume expansion of Si during lithiation.⁸¹

As mentioned in Chapter 1, the MW of LiPAA binders is considered to play an important role in the electrochemical performance of anodes containing Si. This conclusion has been confirmed by other studies. For instance, Haon et al. studied Si anode performance using PAA (MW = 100k, 250k) binders.⁵⁶ It was found that better CEs were obtained with larger PAA or LiPAA molecular weight. Kasinathan et al. studied the MW (250k, 450k, 1250k) effect on Si-alloy/graphite electrode cycling performance.⁶⁰ The research was mainly focused on PAA 250k and PAA 450k, because the viscosity of PAA 1250k was too high to handle. Contrary to the conclusion drawn in the previous case, PAA 250k showed higher capacity retention, better rate capability and smaller crack formation on the surface compared with PAA 450k at the same binder proportion of 8 wt% after cycling. It was thought that these effects resulted from the PAA 250k binder providing excellent slurry processability and rheological behavior.

Despite these conflicting results, to our knowledge no other systematic studies on the effect of PAA binder molecular weight on cycle life have been reported. Furthermore, according to the above mentioned studies, the ways in which PAA can improve alloy electrode cycling performance can be categorized according to whether they are chemical or rheological/mechanical means:

Chemical (functional group related)	Rheological (MW and functional group related)
directly bonding with alloy surfaces providing an artificial SEI	improving slurry viscosity providing good coating dispersion

According to this categorization, the "Chemical" methods for cycling improvement are only related the type and number of functional groups provided by the binder and should not be related to the binder molecular weight. It is clear from the previous studies that the improvements provided in the "Chemical" category by the functional groups are absolutely

crucial for good cycling of alloy electrodes. However, the relative importance of the rheological/mechanical properties of the binder are needed for good cycling. In other words, after a slurry with a good viscosity coated to obtain an electrode with a good particle dispersion, does the molecular weight of the binder play any role in cycling performance? This question is what this study intends to answer.

In this study, NaPAA binders with a wide molecular weight range (from 1.2k to 1250k) are carefully evaluated to elucidate their effect on cycling. The binders were evaluated with water as a solvent, where the NaPAA molecular weight is crucial for obtaining a good coating distribution. The binders are also evaluated using propylene glycol as a solvent. Since propylene glycol is highly viscous, it can provide all the rheological properties needed to form a good coating dispersion, independent of the binder molecular weight. In this way good dispersion coatings can be obtained with NaPAA of various molecular weights to see if the MW has any effect on the electrode performance independent of the binder's rheological properties.

4.2 Experimental

PAA and NaPAA with different MW were purchased from Sigma-Aldrich and Polysciences. Table 4.1 displays the details of the binders obtained. PAA ($M_w = 100k, 250k$) were obtained as aqueous solutions. 2.2 wt% PAA 1250k solution was prepared by dissolving powders in distilled water. PAA ($M_w = 100k, 250k, M_v = 1250k$) acid solutions were neutralized by adding 1M NaOH (reagent grade, $\geq 98\%$, Sigma-Aldrich) until a pH of $\sim 6.5-7.5$ was reached to obtain NaPAA. Distilled water was added to NaPAA ($M_w = 6k$) powders to obtain 40 wt% aqueous solutions. All obtained NaPAA solutions were mixed

by tumbling at 20 rpm for 24h in an empty container to make sure that binder solutions were well-mixed. NaPAA ($M_w = 1.2k, 3k, 8k, 15k$) binders were received as aqueous solutions and used as received. Electrode slurries were prepared by mixing Si alloy (3M V7 alloy) and NaPAA binders in a weight ratio of 9:1. Two types of V7 alloy were used: V7 (D50: 12.15 μm , (D90-D10)/D50: 6.79) and V7 fines (V7f, D50: 0.91 μm , (D90-D10)/D50: 4.70). V7 alloy particle sizes were measured by a laser scattering particle size distribution analyzer LA-950V2. Water or propylene glycol (PG, $\geq 99.5\%$, Sigma-Aldrich) which served both as a solvent and as a thickener were added to control slurry viscosity. Sodium carboxymethyl cellulose (CMC, average $M_w \sim 90,000$, Sigma-Aldrich) was also used as a slurry thickening agent for some coatings. Table 4.2 shows the coating recipe of the prepared binder slurries made with different thickeners. These V7f/NaPAA 9/1 w/w slurries are labelled as [alloy]/[MW NaPAA]/[thickener] (e.g. V7f/1.2k/PG indicates a V7f/NaPAA 9/1 w/w slurry made with 1.2k NaPAA with PG slurry solvent used as a thickener). V7/NaPAA 9/1 slurries were made in the same way with no thickener and with 0 - 2 g of distilled water to control viscosity. These slurries are labeled as [alloy]/[MW NaPAA]/H₂O (e.g. V7/1.2k/H₂O indicates a V7/NaPAA 9/1 w/w slurry made with 1.2k NaPAA with distilled water used as the slurry solvent). All slurries were mixed in a planetary mill (Retsch PM200) at 100 rpm for 1 hour with three 0.5-inch tungsten carbide balls. Then slurries were coated onto 15 μm thick Cu foil (Furukawa Electric, Japan) with a 0.004 inch gap coating bar. Neat V7f coatings made with the 0.004 inch gap height possess a high active material loading of $\sim 5 \text{ mg/cm}^2$ because of the fine particle size and the high density of the V7f material. Thus a layer of tape with a thickness of ~ 0.002 inch was used to control the alloy loading of a neat V7f alloy electrode. The coatings were stored

in air at room temperature overnight, dried in air at 120 °C for half an hour, cut into 1.3 cm² disks and then heated under vacuum overnight at 120 °C. The mass loading of the active material was ~2.0-2.5 mg/cm², corresponding to a specific capacity of ~2.4-3.0 mAh/cm².

Assembly and electrochemical tests of coin cells were the same as described in the experimental section of Chapter 3. Slurry viscosity was measured using a Viscolead ONE Rotational Viscometer (Fungilab) with a stainless steel L4 spindle and rotating at 100 rpm. Thermogravimetric Analysis (TGA) was carried out using a TA Instruments SDT Q600 under dried air flow (150 mL/min) from room temperature to 400 °C with a heating rate of 1 °C/min.

Table 4.1 Physical state and molecular weight of PAA or NaPAA binders.

M_w	Vendor	Physical State
1,200	Aldrich	Sodium salt, 45 wt% in H ₂ O
3,000	Polysciences	Sodium salt, 40 wt% in H ₂ O
6,000	Polysciences	Sodium salt, powder
8,000	Aldrich	Sodium salt, 45 wt% in H ₂ O
15,000	Aldrich	Sodium salt, 35 wt% in H ₂ O
100,000	Aldrich	Acid, 35 wt% in H ₂ O
250,000	Aldrich	Acid, 35 wt% in H ₂ O
1,250,000 (M_v)	Aldrich	Acid, powder

Table 4.2 Slurry formulations of the prepared V7 (or V7 fines)-NaPAA coatings.

	Slurry	V7f/g	Binder/g	1M NaOH Solution/g	Thickener/g
1	V7/1.2k/H ₂ O	1.0	0.25	N/A	NR
2	V7/3k/H ₂ O	1.0	0.28	N/A	NR
3	V7/6k/H ₂ O	1.0	0.11	N/A	NR
4	V7/8k/H ₂ O	1.0	0.25	N/A	NR
5	V7/15k/H ₂ O	1.0	0.32	N/A	NR
6	V7/100k/H ₂ O	1.0	0.25	1.10	NR
7	V7/250k/H ₂ O	1.0	0.25	1.10	NR
8	V7/1250k/H ₂ O	1.0	0.088	1.10	NR
9	V7/1.2k/CMC	1.0	0.25	N/A	0.022 (CMC)
10	V7/250k/CMC	1.0	0.25	1.10	0.022 (CMC)
11	V7f/1.2k/PG	1.0	0.25	N/A	1.3 (PG)
12	V7f/3k/PG	1.0	0.28	N/A	1.3 (PG)
13	V7f/6k/PG	1.0	0.11	N/A	1.3 (PG)
14	V7f/8k/PG	1.0	0.25	N/A	1.3 (PG)
15	V7f/15k/H ₂ O	1.0	0.32	N/A	1.2 (H ₂ O)
16	V7f/100k/H ₂ O	1.0	0.25	1.10	0.5 (PG)
17	V7f/250k/H ₂ O	1.0	0.25	1.10	0.2 (PG)
18	V7f/1250k/H ₂ O	1.0	0.088	1.10	3.85 (H ₂ O)

* N/A = not applicable; NR = no record. For slurries 1-9, water was added as a slurry solvent (thickener), but the amount was not recorded.

4.3 Results and Discussion

Section I Effect of Binder MW on Alloy Cycling

Figure 4.1(a) and (b) show images of V7/1.2k/H₂O and V7/250k/H₂O electrodes, respectively. All the NaPAA electrode slurries with NaPAA MW of 250k or less had low viscosities and were unable to maintain a suspension of the alloy particles. Even the V7/250k/H₂O slurry, which is a typical NaPAA MW used in electrodes, had a low viscosity of ~400 cPs, with alloy particles subsidence observed during the viscosity measurement. The viscosity of the V7/1250k/H₂O slurry was not measured because it was too viscous. During coating of low viscosity slurries, the alloy particles settled on the current collector

(see Figure 4.1(a)). This caused the amount of alloy to be high in the place where the slurry was first poured onto the foil. The alloy particle size was likely the highest in this position also (large particles first to settle from the slurry). As the coating bar was drawn with simultaneous alloy settling, the electrode loading decreases and particle size likely becomes smaller. At the same time the alloy particles settled to the current collector, the low viscosity binder solution spread in all directions, as illustrated in Figure 4.2(a). Particle settling can lead to varying material/binder composition along the electrode and unreliable electrode performance. Consequently, the concentration of the binder in the low MW coatings was decreased substantially below the designed value. However, when NaPAA with MW > 100k were used, the binder solution did not spread out appreciably beyond the boundaries of the coated area, as shown for the V7/250K/H₂O electrode in Figure 4.1(b), and schematically illustrated in Figure 4.2(b).

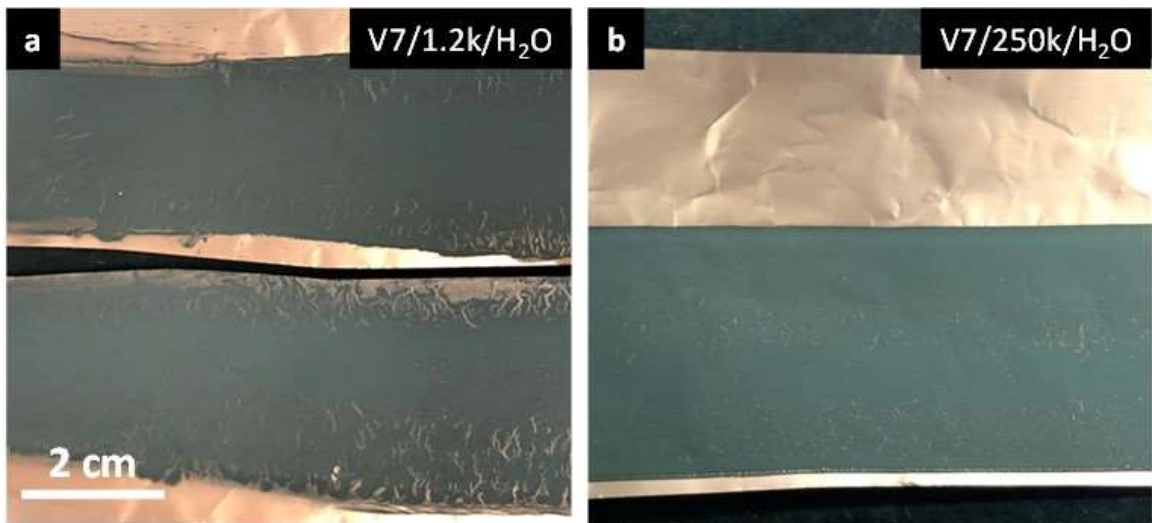


Figure 4.1 Appearance of V7/1.2k/H₂O and V7/250k/H₂O electrodes. Both electrodes show particle settling.

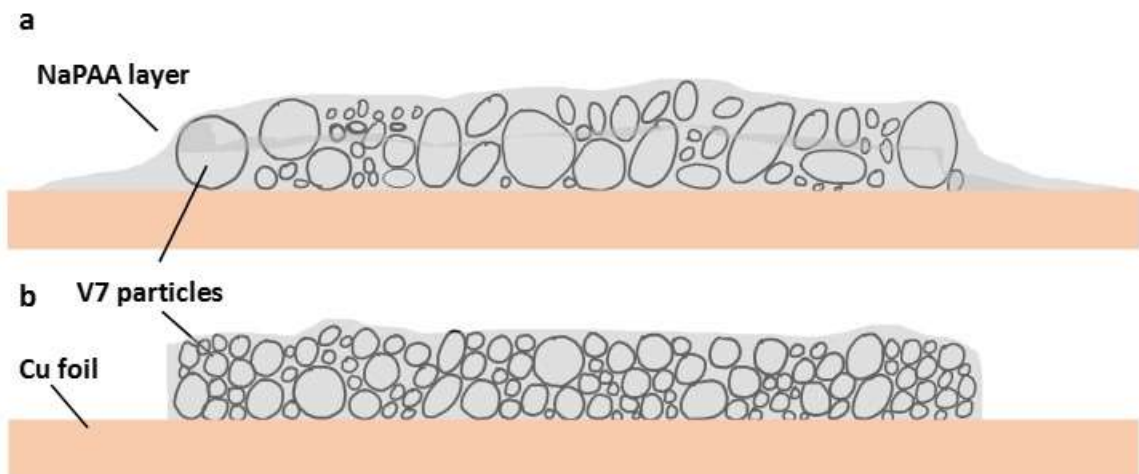


Figure 4.2 Cross-sectional schematic diagrams of (a) V7/low MW binder/H₂O and (b) V7/high MW binder/H₂O. Grey areas correspond to the binder solution in electrode slurries.

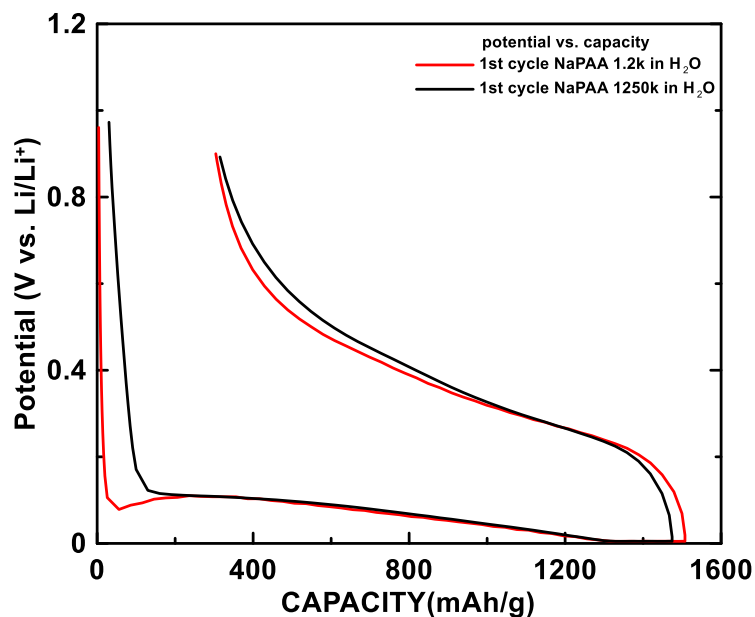


Figure 4.3 The first cycle potential vs. capacity curves of V7/1.2k/H₂O and V7/1250k/H₂O electrodes, respectively.

Figure 4.3 shows potential versus capacity curves of V7/1.2k/H₂O and V7/1250k/H₂O electrodes. The V7/1.2k/H₂O electrode shows a prominent initial nucleation/growth plateau at about 0.1 V, while the V7/1250k/H₂O electrode does not. This

may be because the 1.2k electrode possessed more large particles that settled in the area where the electrode was punched. The large electrode particles being more susceptible to Li nucleation and growth processes during the initial lithiation than the small alloy particles. Both curves show the two characteristic sloping plateaus of Si-alloy as mentioned in Chapter 1. The ICE of V7-NaPAA 1.2k and V7-NaPAA 1250k was 80% and 79%, respectively. The first delithiation capacity of V7-NaPAA 1.2k and V7-NaPAA 1250k was 1203 mAh/g and 1161 mAh/g, respectively. The observed capacity variation is likely from random error in cell building/weighing of the active mass.

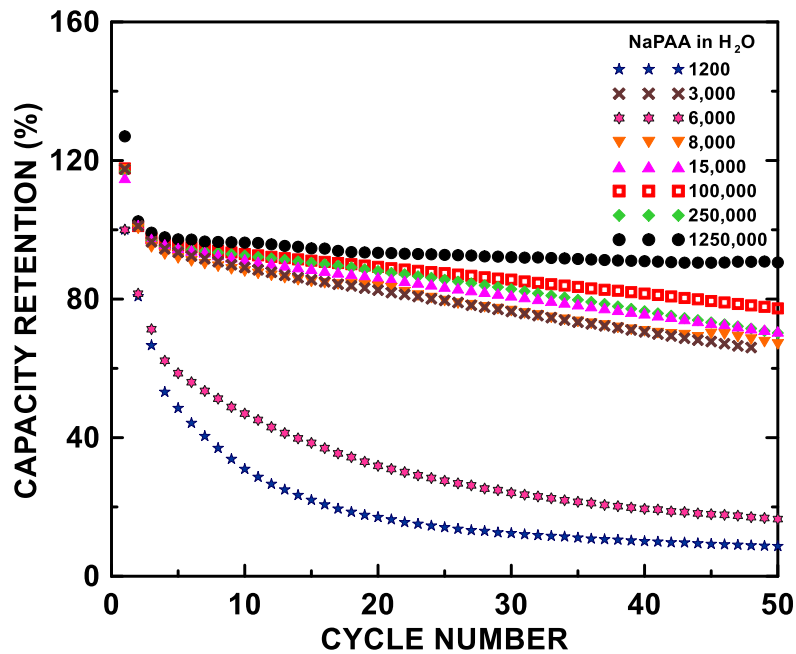


Figure 4.4 Cycling performance V7 electrodes using NaPAA binders with different MW.

Figure 4.4 shows the cycling performance over 50 cycles of Si-alloy/NaPAA electrodes where the NaPAA molecular weight is varied from 1.2k - 1.25M and where the coating solvent used was pure distilled water. The electrodes with low molecular weight (1.2k - 6k) binders have unpredictable cycling performance, with the cycling performance of the 1.2k and 6k electrodes being extremely poor while the cycling performance of the 3k electrode being good. This is likely due to nonuniform material/binder composition

resulting from particle settling and the loss of binder from the electrode during coating, as discussed above.



Figure 4.5 Appearance of V7/250k/CMC (left) and V7/1.2k/CMC (right) electrodes.

To increase the slurry viscosity, polymeric CMC was used as a slurry thickener.⁸² The appearance of electrodes with 2 wt% CMC thickener is shown in Figure 4.5. It is apparent that the addition of CMC thickener provides little aid in the coating quality, with particle settling being apparent for the V7/1.2k/CMC slurry, which is likely due to the small thickener amount. Surprisingly, the 1.2k binder solution separation from the active material disappeared compared to what observed in Figure 4.1(a).

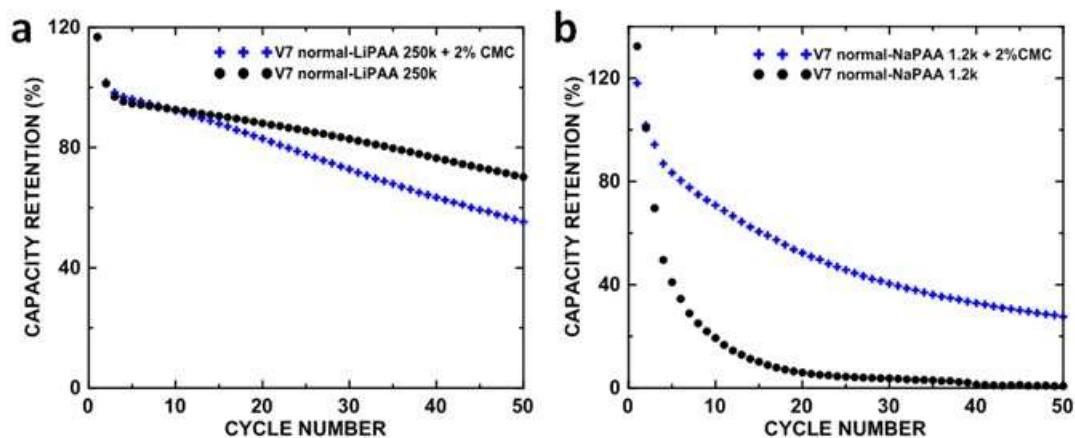


Figure 4.6 The cycling of (a) V7/250k/H₂O and V7/250k/CMC electrodes, and (b) V7/1.2k/H₂O and V7/1.2k/CMC electrodes.

Figure 4.6 shows the cycling performance of V7/250k/H₂O and V7/1.2k/H₂O electrodes with and without 2 wt% CMC. It was found that the addition of 2 wt% of CMC resulted in a reduction in capacity retention of the V7/250k/H₂O electrode (see Figure 4.6(a)). This is likely due to the lower functional group density of CMC compared to NaPAA binder.²⁷ In contrast, 2 wt% CMC resulted in a significantly enhanced capacity retention of the V7/1.2k/H₂O electrode, as shown in Figure 4.6(b). The most likely reason that CMC improved the capacity retention of the V7/1.2k/H₂O electrode is that CMC polymer prevented binder loss during the coating making process. It is unfortunate, however, that the presence of CMC in the V7/250k/CMC electrode reduced its capacity retention compared to the V7/250k/H₂O electrode. This shows that the addition of a CMC thickener can improve slurry rheological properties, but can negatively affect cycling performance because of the low functional group density of CMC compared to NaPAA.

To fully appreciate the effect of improving slurry rheology on capacity retention requires a slurry thickener that can be removed during the electrode drying process, so that the final electrode composition is unchanged. This was accomplished by using PG as the slurry solvent instead of water.

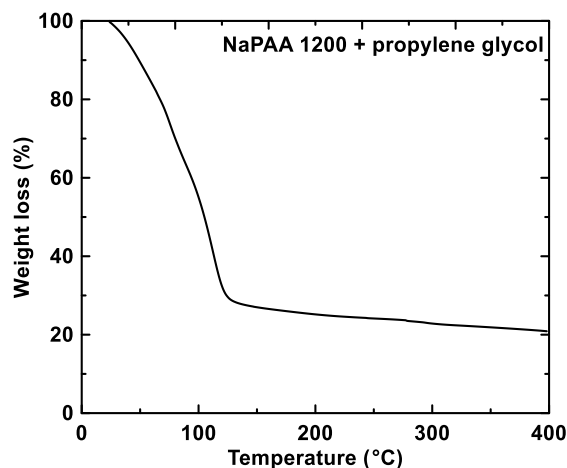


Figure 4.7 Thermogravimetric Analysis (150 mL/min air flow, 1 °C/min) of a 45 wt%

NaPAA 1.2k aqueous solution and a propylene glycol solvent in a weight ratio of 1:1.

To determine if the PG could be removed from the slurry by standard solvent drying methods, a solution comprising a 45 wt% 1.2k NaPAA aqueous solution and PG in a weight ratio of 1:1 (i.e. a NaPAA/H₂O/PG 22.5/27.5/50 solution) was prepared. The obtained solution was clear, colorless and uniform. Figure 4.7 shows the result of a TGA measurement of this solution. After heating to 175 °C, 22.5 wt% of the solution mass remained, while further heating up to 400 °C resulted in little mass change. This confirmed that the H₂O/PG solvent could be successfully removed by heating, leaving only the NaPAA binder as a residue.

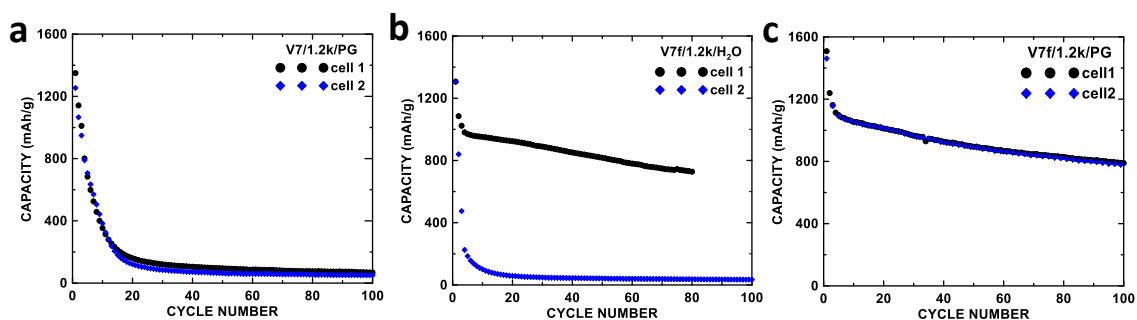


Figure 4.8 Cycling performance of (a) V7f/1.2k/PG, (b) V7f/1.2k/H₂O, and (c) V7f/1.2k/PG electrodes.

Figure 4.8(a-c) shows the cycling performance of V7f/1.2k/PG, V7f/1.2k/H₂O and V7f/1.2k/PG electrodes respectively. V7f/1.2k/PG electrodes retain ~10% of their original discharge capacity over 100 cycles, because they suffer from bad coating quality resulting in particle settling and binder loss, similarly as shown in Figure 4.2(a). The binder loss resulting from the low slurry viscosity leads to the poor mechanical integrity of V7 electrodes and thus the undesirable cell cycling. The large particles in the V7 material exacerbate the situation, since the uneven material loading due to the particle settling are very likely to result in Li plating during the repeated lithiation/delithiation process. Binder

loss is also a problem faced for the V7f/1.2k/H₂O coating. In this case, the liquid phase of the slurry spread out immediately after pouring the slurry onto the Cu foil, and the solid phase tended to remain where the slurry was poured. Therefore, the part of the coating at the beginning comprises more binder and, conversely, the part at the end comprises more particles. As a result, the cell cycling is highly dependent on the location where the electrode is obtained due to the uneven component distribution. As shown in Figure 4.8(b), the electrode for cell 2 is possibly from a low binder content part of the coating, which fades quickly at the beginning of cycling due to mechanical failure. Compared to these electrodes, V7f/1.2k/PG electrodes have the significantly improved cycling performance and good cycling reproducibility (Figure 4.7(c)), since a homogenous coating without binder loss can be obtained due to the proper slurry viscosity.

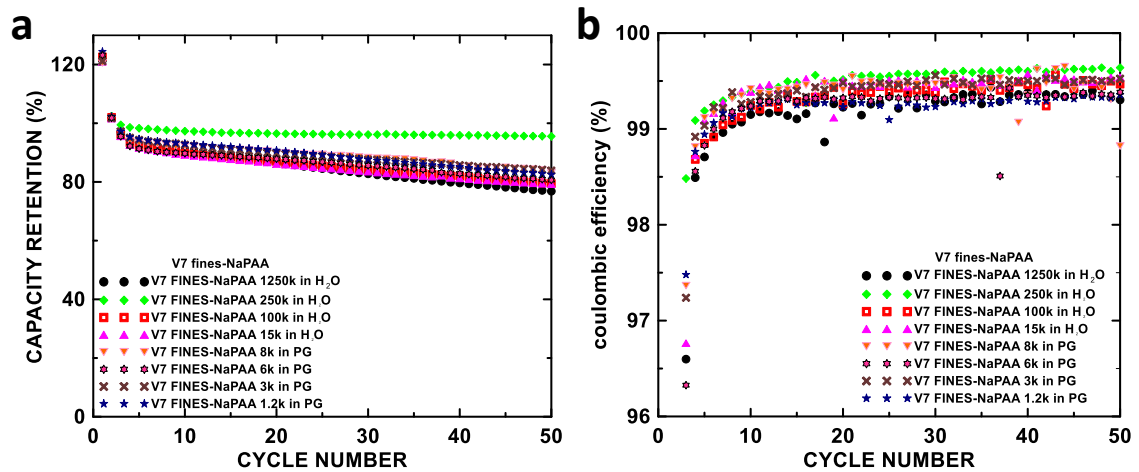


Figure 4.9 (a) Cycling performance and (b) CEs of V7f electrodes with different MW NaPAA binders and with PG or H₂O slurry solvent.

Figure 4.9 shows the discharge capacity retention and the CE versus cycle number of V7f electrodes with different NaPAA binder MWs and H₂O or PG slurry solvent. In Figure 4.9(a), the performance of the electrode with NaPAA 250k binder significantly outperformed others, which displayed the highest average coulombic efficiency of 99.48%

(from 2nd to 50th cycle) and the highest capacity retention of 94.58% over 50 cycles. It is not known why this particular batch of binder had such good performance. The electrodes with other binders: NaPAA 1.2k, 3k, 6k, 8k, 15k, and 100k all show comparable capacity retention, ICE and CE values. No obvious trend in capacity retention, ICE or CE with respect to binder MW could be observed (see Table 4.3 for more details). Since these parameters are related to electrode mechanical failure and SEI forming parasitic reactions, similar values in these parameters indicate that alloy particles of all electrodes were in good contact and underwent similar parasitic reactions during cycling. This is in contrast to the electrodes shown in Figure 4.4, where low viscosity slurries resulted in particle settling, binder loss and poor cycling performance. These results show that when slurry rheology is maintained by other means, the binder MW has no relation to alloy cycling performance.

Table 4.3 Capacity retention and coulombic efficiency of the neat V7f electrodes as indicated.

electrode	First CE (%)	Average CE (2 nd -50 th cycles) (%)	Discharge capacity retention over 50 cycles (%)
V7f/1.2k/PG	81.01	99.26	84.25
V7f/3k/PG	82.84	99.39	85.68
V7f/6k/PG	81.28	99.24	79.89
V7f/8k/PG	82.64	99.38	85.29
V7f/15k/H ₂ O	82.78	99.38	80.68
V7f/100k/H ₂ O	81.93	99.21	78.11
V7f/250k/H ₂ O	81.56	99.49	94.58
V7f/1250k/H ₂ O	81.69	99.05	74.79

Section II Slurry Recipe Optimization & Viscosity Measurement

Electrode slurries are typically non-Newtonian fluids whose viscosity can change based on applied stress or force. They are thixotropic, where interactions such as hydrogen bonding between functionalized polymer chains can be easily broken by shear forces, leading to shear thinning.⁸³ When not under shear electrode slurries have a relatively high

and constant viscosity, which prevents particle settling during electrode processing or when a slurry is at rest.⁶⁰ In this section, slurry recipe optimization is presented to enable the use of the slurry preparation method where PG serves as a slurry thickener for neat alloy slurries in industry. Slurry rheological properties are characterized by viscosity.

Slurry rheology describes the flow behavior of its components including both solid and liquid phases and is determined by various attributes such as mass fraction, particle size and distribution, particle shape, density, rotation, temperature, pH etc.^{84,85} In this study, slurry viscosity was measured at room temperature (~ 25 °C), all NaPAA binders used have pH values of 6.5-7.5, and active materials (two types of V7 alloys) are used without further treatment. Therefore, V7/NaPAA slurry viscosity is mainly dependent on the solid fraction and the viscosity of liquid phase.

Recently, a study investigated the rheological properties of slurries comprising mainly Si, the solid content (including both particles and binders) was ~ 30 -40 wt%.⁵⁶ Considering the higher alloy density compared to pure Si, in this study, the solid fractions (solely including particles) of low MW binder slurries were set to 50 wt%, resulting in a similar volume fraction. Slurries 19-22 were made to study the effect of particle size distribution and use of thickener on the slurry viscosity. Slurry 19, which uses a low molecular weight binder and water solvent, had a very low initial viscosity of 89.3 cPs (only one data point was recorded due to appreciable particle settling during the viscosity measurement). Figures 4.10(a-c) show the viscosity vs. time curves for slurries 20-22. Both V7f/1.2k/H₂O and V7/1.2k/PG slurries showed a low viscosity of ~ 300 cPs. Solid-liquid separation was observed in these two slurries during the viscosity measurement. Particle settling was due to the large size of V7 in the case of the V7/1.2k/PG slurry and low

viscosity in the case of the V7f/1.2k/H₂O slurry. In contrast, the V7f/1.2k/PG slurry viscosity was ~2300 cPs and remained constant for 30 mins, implying that the slurry components were evenly dispersed and that settling was minimal. The properties of this slurry are in the range that is desirable for slurries for commercial electrode coatings (no settling, viscosity in the range of 1700 - 3500 cPs). It turned out that the smaller sized alloy particles are necessary to achieve a slurry with proper viscosity when PG served as the thickener. For this reason, the following experiments were carried out with fine-sized V7 alloy.

Table 4.4 Formulations of the prepared neat V7f slurries using different MW binders.

	slurry	Active material/g	Binder/g	NaOH (1M)/g	PG/g	H ₂ O/g	Solid fraction in slurry
19	V7/1.2k/H ₂ O	5.0	1.2	N/A	0	3.8	50%
20	V7/1.2k/PG	5.0	1.2	N/A	3.8	0	50%
21	V7f/1.2k/H ₂ O	5.0	1.2	N/A	0	3.8	50%
22	V7f/1.2k/PG	5.0	1.2	N/A	3.8	0	50%
23	V7f/3k/PG	4.5	1.3	N/A	3.8	0	47%
24	V7f/6k/PG	5.0	1.4	N/A	3.7	0	50%
25	V7f/8k/PG	5.5	1.4	N/A	4.1	0	50%
26	V7f/15k/PG	4.5	1.4	N/A	3.9	0	46%
27	V7f/100k/PG	3.5	1.1	4.8	0	0	37%
28	V7f/250k/PG	3.5	1.1	4.8	0	0	37%

PAA binders with relatively low MWs (< 100k) are available as sodium salts. Therefore, electrodes with such binders only contained the Si-alloy, binder and PG (Table 4.4, slurries 23-26). Binders having greater MWs (\geq 100k) are available only as acids. These binders needed to be first neutralized with 1M aqueous NaOH solution to make the PAA sodium salt. Therefore, electrodes with these binders contained Si-alloy, binder, and water from the neutralization process (Table 4.4, slurries 27-28). Electrode slurries using a PG thickener have a high viscosity (> 2000 cPs) which remains stable during the viscosity measurement (Figures 4.10(d-g)). Whereas both 100k and 250k slurries have a low

viscosity (~600 cPs for V7f/100k/H₂O and ~800 cPs for V7f/250k/H₂O, Figure 4.10(h-i)) due to the neutralization by aqueous NaOH solution. The viscosity of V7f/1250k/H₂O slurry was not measured, because it is too viscous to handle.

In future work, the results should be repeated, keeping the total percent solids content the same for all slurries and within typical slurry solids contents used by cell manufacturers (~40-50% solids by volume, corresponding to a weight fraction of 70-80% using the same type alloy). Viscosity of the slurry/binder solution should also be assessed independently of the total slurry viscosity, since the slurry/binder solution viscosity is key to prevent particle settling.

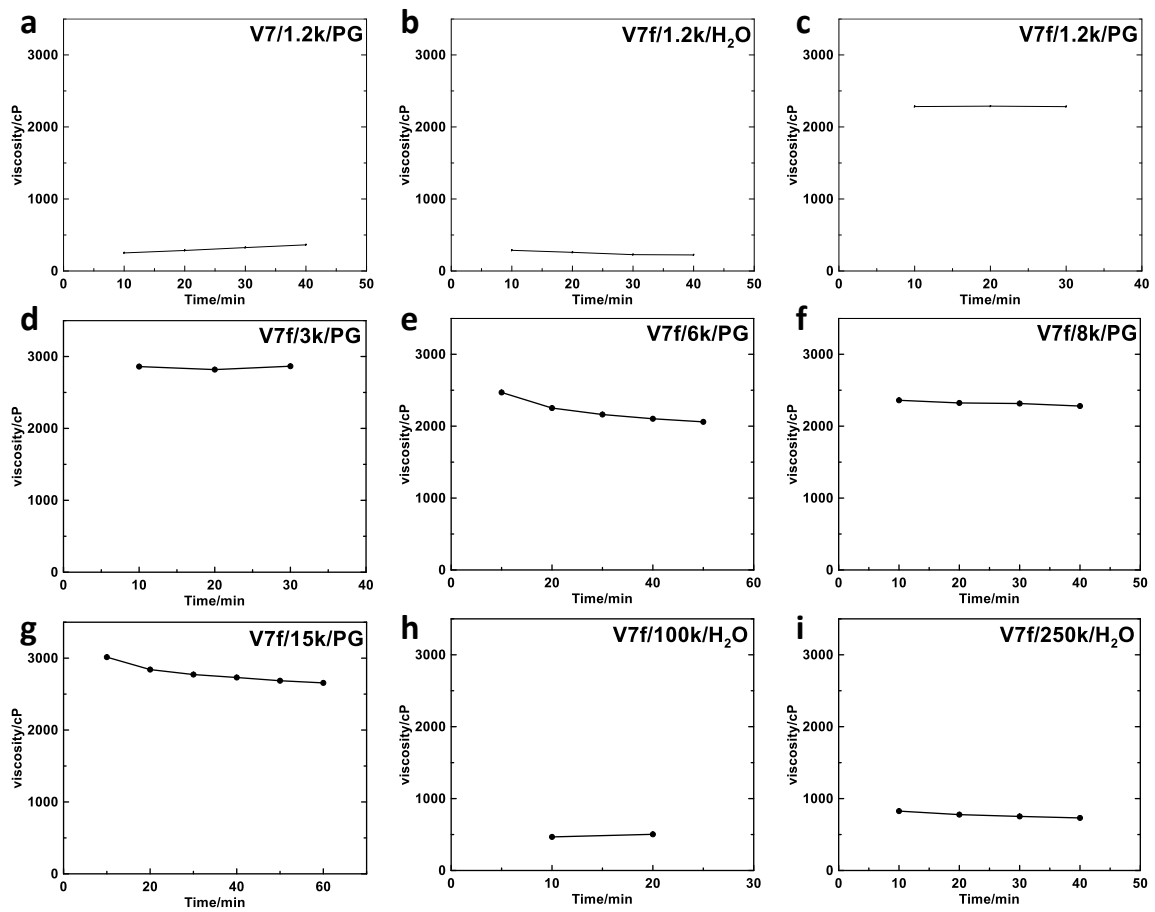


Figure 4.10 Viscosity vs. time curves for electrode slurries using different MW NaPAA binders as indicated.

4.4 Conclusions

In this chapter, the effect of NaPAA molecular weight on the cycling performance of pure Si alloy anode was investigated. Eight different molecular weights of NaPAA binders were tested (1.2k, 3k, 6k, 8k, 15k, 100k, 250k, 1250k). Low MW binders resulted in low slurry viscosity, and particle settling and binder loss during coating. Such electrodes had large capacity fade in Li cells. The addition of slurry thickeners such as CMC could mitigate the poor rheology of low MW binders, resulting in the significantly enhanced electrode performance. However, the presence of CMC was found to increase capacity fade due to it having a smaller carboxyl group density compared to NaPAA. In contrast, using PG as a slurry solvent resulted in electrode slurries with good rheological properties even when very low MW NaPAA binders were used. Moreover, all of the PG could be removed during the electrode drying process, so that it did not affect the final electrode composition. When PG was used as a slurry solvent to improve the rheology of low MW binder slurries, electrodes using binders of any MW were found to cycle well. These results show that as long as a good slurry rheology is maintained, the binder MW has no relation to alloy cycling performance.

Chapter 5 MOLECULAR BINDERS FOR SI-ALLOY ANODES

5.1 Introduction

In Chapter 4 it was shown that electrochemical performance of an alloy electrode is independent of binder molecular weight (MW) if a high-viscosity slurry solvent is used to take on the rheological role typically filled by having binders with long polymer chains. According to this observation, molecular binders might equally perform well as polymer binders if a high-viscosity slurry solvent is used. Additionally, it was shown in Chapter 3 that electrochemical performance is strongly related to binder functional group density. Therefore, it follows that molecules with high functional group density might serve as binders with good electrochemical performance if used in conjunction with a high-viscosity slurry solvent. Molecular binders have been used in the past with Si anodes. For instance, a Si nanoparticle anode with citric acid (CA) binder was observed to have similar capacity retention as a poly(acrylic acid) binder by Nguyen et al.⁷⁵ These slurries were cast from an NMP solvent, which likely has sufficient viscosity to keep Si-nanoparticles suspended in solution. However, this would not be the case for commercial anode coatings, which would comprise micron-sized graphite and micron-sized higher density alloy particles. Such active materials would quickly settle from low viscosity slurry unless thickening agents were added.

In this study, the cycling performance of pure Si-alloy (V7) and Si-alloy/graphite anodes made with a CA binder in combination with a high viscosity propylene glycol (PG) slurry solvent were evaluated and compared with conventional anodes using a long-chain LiPAA binder.

5.2 Experimental

Electrode coatings were prepared from Si-alloy (V7 alloy, 3M Company), graphite (MAGE, Hitachi or KS6, Imerys Graphite and Carbon), carbon black (CB, C-ENERGY Super C65, Imerys Graphite and Carbon), CA (anhydrous, 99.5+%, Alfa Aesar), LiPAA (from a 10 wt% solution prepared by neutralizing PAA ($M_w = 250,000$, Sigma-Aldrich) solution with lithium hydroxide ($\text{LiOH}\cdot\text{H}_2\text{O}$, $\geq 98\%$, Sigma-Aldrich)), distilled water, and PG ($\geq 99.5\%$, Sigma-Aldrich). with compositions indicated in Table 5.1. Electrode slurries were mixed in a planetary mill (Retsch PM200) at 100 rpm for 1 hour with three 0.5-inch tungsten carbide balls and then spread onto 15 μm thick copper foil with a 0.004-inch coating bar. Coatings were stored in air at room temperature overnight and then dried for 30 mins at 120 °C in air. Electrode disks with an area of 1.30 cm^2 were punched from the coatings after drying and heated under vacuum at 120 °C overnight before cell making. The mass loadings of pure V7 and V7/MAGE electrodes were $\sim 2 \text{ mg/cm}^2$ and $\sim 2.5 \text{ mg/cm}^2$, respectively, corresponding to specific capacities of $\sim 2.4 \text{ mAh/cm}^2$ and $\sim 1.6 \text{ mAh/cm}^2$.

Coin cell assembly and electrochemical test procedures were the same as described in the experimental section of Chapter 3. Slurry viscosity measurement was carried out in the same way as described in the experimental section of Chapter 4.

Table 5.1 Slurry formulations used in this study (all quantities in grams).

	V7	MAGE	KS6	CB	CA	(10 wt% LiPAA/H ₂ O)	H ₂ O	PG
V7-LiPAA/H ₂ O	0.50					0.56	0	
V7-CA/H ₂ O	0.50				0.056		0.50	
V7-CA/PG	0.50				0.056			0.50
V7/graphite-LiPAA/H ₂ O	0.50	0.98	0.083	0.033		1.8	1.4	
V7/graphite-CA/PG	0.50	0.98	0.083	0.033	0.18			3.0

*0.18g isopropanol was also added to the slurries containing graphite to increase the

wettability.

5.3 Results and Discussion

Figure 5.1 shows the slurry viscosity as a function of time and digital photographs for the V7-CA/PG and V7-CA/H₂O slurries, respectively. The viscosity of the V7-CA/PG slurry was ~1500 cP at the beginning of the measurement and remained constant at ~1400 cPs for half an hour. No particle settling was observed during the measurement. The V7-CA/PG coating was homogeneous, as depicted in Figure 5.1(b). The viscosity of the V7-CA/water slurry continuously decreased from ~900 cPs to ~600 cPs. The low slurry viscosity indicated that the particle settling occurred and the water solvent failed to inhibit the settling of V7 particles during the measurement procedure. This is not ideal as the uneven distribution of particles would cause loading variation and possible Li-plating in full cells.

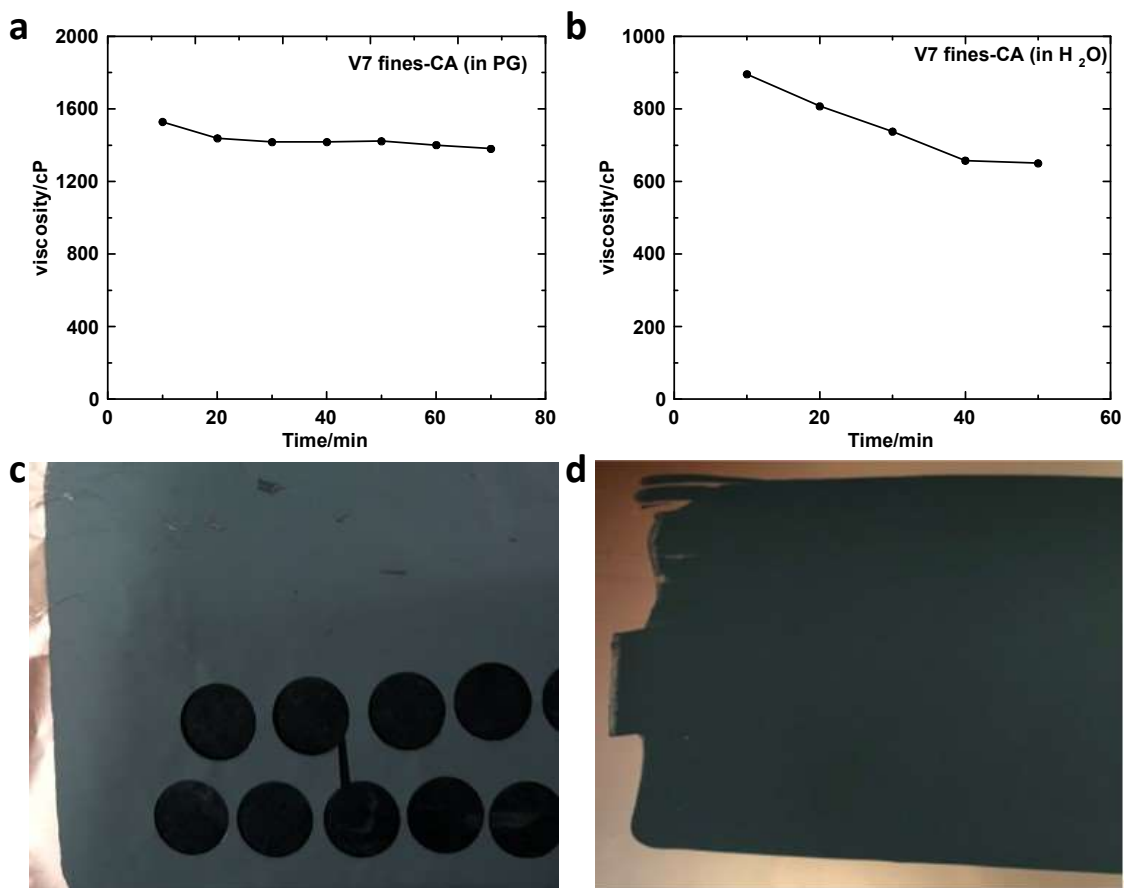


Figure 5.1 Viscosity vs. time curves for V7-CA slurries made with (a) PG and (b) H₂O. (c) Digital photos of V7-CA coatings made with (c) PG and (d) H₂O solvent.

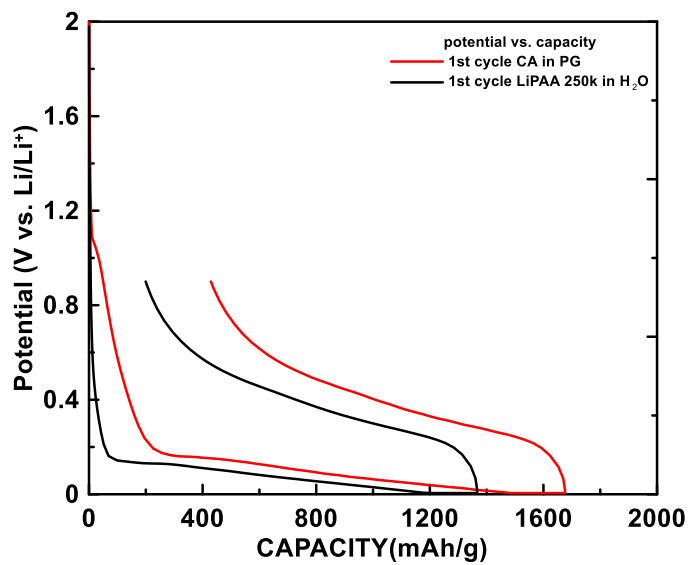


Figure 5.2 The first cycle potential vs. capacity curves of V7-CA/PG and V7-LiPAA/H₂O

electrodes.

Figure 5.2 shows the potential vs. capacity curves of V7-CA/PG and V7-LiPAA/H₂O electrodes. During the first lithiation, both curves show a nucleation plateau at ~0.16 V and two characteristic sloping plateaus of Si, as mentioned in Chapter 1. The plateau at ~1.1 V (Li/Li⁺) for the V7-CA electrode is likely because that protic acid is not stable at a low potential and reduced to release H₂(g), leading to the irreversible capacity.

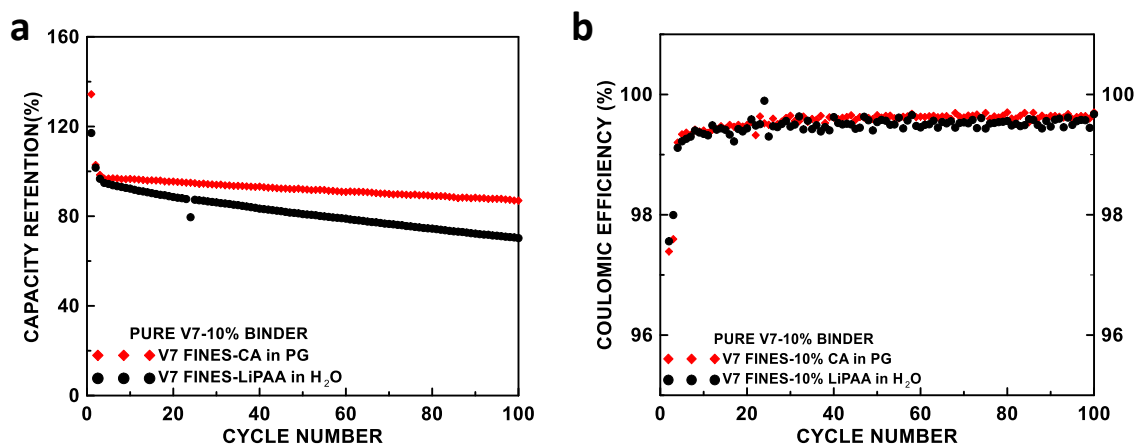


Figure 5.3 (a) Capacity retention and (b) CE for V7-CA/PG and V7-LiPAA/H₂O electrodes.

Figure 5.3 shows the capacity retention and CE (cycles 2-100) for V7-CA/PG and V7-LiPAA/H₂O electrodes. After 100 cycles, the capacity retention of the V7-LiPAA/H₂O and the V7-CA/PG electrodes were 70% and 87%, respectively. The average CEs (cycle 2-100) for V7-LiPAA/H₂O and V7-CA/PG electrodes were 99.45% and 99.54%, respectively. The V7-CA/PG electrode had higher capacity retention as well as a higher CE than the electrode with a traditional LiPAA binder processed with water. The enhanced performance of CA could be explained by its higher functional group density (1.2 times as many carboxyl groups per unit mass than LiPAA), resulting in a greater incidence of covalent and hydrogen bonding between CA binder and alloy particles.

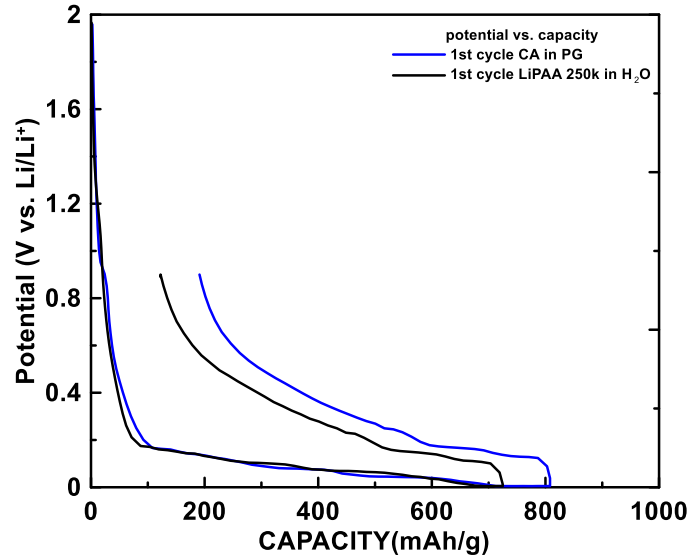


Figure 5.4 The first cycle potential vs. capacity curves of V7/MAGE-CA and V7/MAGE-LiPAA electrodes.

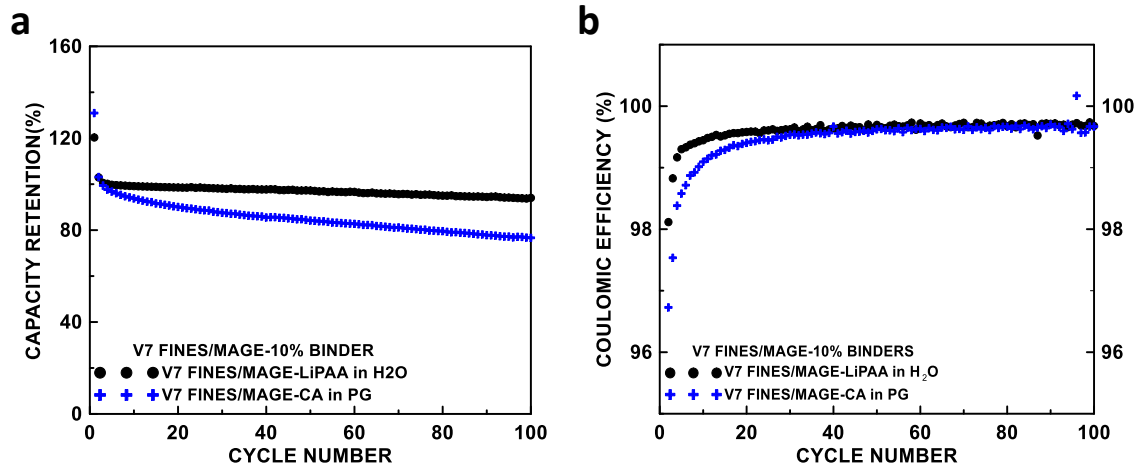


Figure 5.5 (a) Capacity retention and (b) CE of V7/MAGE-CA and V7/MAGE-LiPAA electrodes.

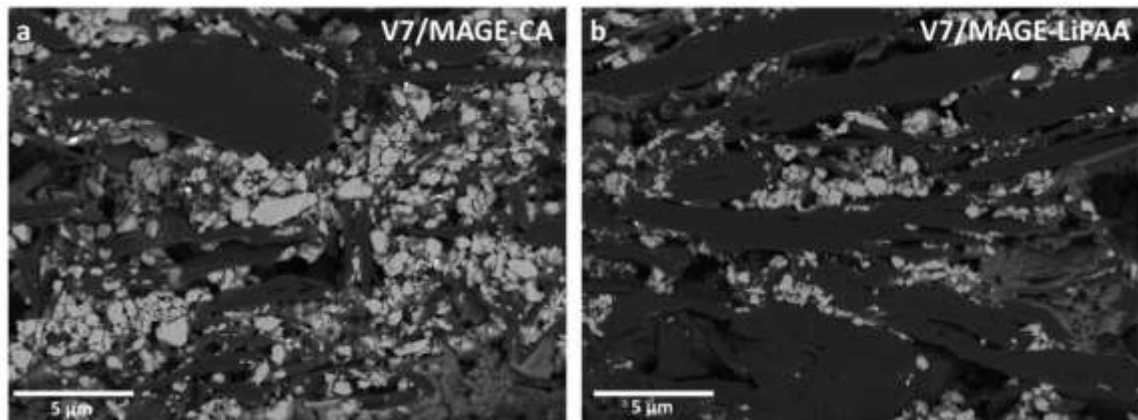


Figure 5.6 Cross-sectional BSE images of (a) V7/MAGE-CA/PG and (b) V7/MAGE-LiPAA/H₂O electrodes.

Figure 5.4 shows the potential vs. capacity curves of a V7/MAGE-CA/PG electrode and a V7/MAGE-LiPAA/H₂O electrode. During initial lithiation, both cells show a combination of two sloping plateaus characteristic of amorphous Si and three plateaus characteristic of graphite, as mentioned in Chapter 3. The small initial lithiation plateau at ~ 0.9 V (Li/Li⁺) for the V7/MAGE-CA electrode is also likely present because of the reduction of H⁺ to release H₂ gas. Figure 5.5 shows the capacity retention and CE (from the second cycle) for the same electrodes. The V7/MAGE-LiPAA/H₂O electrode showed enhanced capacity retention of 94% after 100 cycles, compared to the capacity retention of 83% of V7/MAGE-CA/PG electrode. The average CEs (cycle 2-100) for V7/MAGE-LiPAA and V7/MAGE-CA were 99.61% and 99.47%, respectively. A reason for this difference in cycling performance could stem from differences in coating dispersion quality for the two binder systems. Indeed, it was found by SEM (Figure 5.6) that V7/MAGE-CA/PG electrode contains a higher amount of agglomerated V7 particles compared to the V7/MAGE-LiPAA/H₂O electrode. This is despite using a planetary mill to disperse the slurries, which we have found can produce much better dispersions (due to collisions with the milling balls that can break apart agglomerated alloy particles) than typical Cowles

blade high-shear impeller mixers used in industry. The greater degree of V7 agglomeration could be due to the stronger interaction between particles induced by the greater functional group density and the stronger hydrogen bonding in the CA binder. The resulting inhomogeneous coating dispersion of the V7/MAGE-CA/PG electrode could lead to uneven volume changes in the electrode during cycling and gradual mechanical failure. Therefore, while electrodes with high functional group density molecular binders can have excellent cycling properties in pure alloy electrodes, improved dispersion quality needs to be achieved to enable good cycling in alloy-graphite mixed active material electrodes.

5.4 Conclusion

In this study, PG was investigated as a slurry solvent to enable the use of molecular binders in electrodes comprising Si-alloy. The use of high-viscosity PG as a slurry solvent prevents particle settling during the slurry making procedure, therefore removing the necessity of binders having to provide rheological properties to the slurry. It was found that Si-alloy-CA/PG electrodes had higher CE and capacity retention than conventional Si-alloy-LiPAA/H₂O electrodes. This demonstrates that if the rheological role played by polymer molecular weight is replaced by a high viscosity slurry solvent, then small molecules with high functional group density can be used as effective binders for Si-alloy electrodes. In contrast, Si-alloy/MAGE-LiPAA/H₂O electrodes had better performance compared to the Si-alloy/MAGE-CA/PG electrodes. This was ascribed to an inferior alloy/graphite dispersion in the Si-alloy/MAGE-CA/PG electrode. A dispersant is needed to solve the agglomeration problem to enable the use of acidic molecular binders for alloy-graphite mixed active material electrodes.

Chapter 6 THE EFFECT OF BINDERS ON ALLOY DEGRADATION AND CYCLING

6.1 Introduction

An ideal SEI is a passivating layer which has the capability of inhibiting further electrolyte degradation on anode surfaces by solely allowing Li ions to diffuse through, but limiting the passage of solvent ions during cycling.²³ As mentioned in Chapter 1, binders have been reported to act as SEI modifiers and are considered vital to anode electrochemical performance. During cycling, binders become a portion of the SEI, which mainly comprises insoluble organic and inorganic electrolyte decomposition products. The SEI is commonly analyzed by surface analysis techniques, such as XPS, FTIR, AFM etc.^{23,75,86} However, the SEI and its components are significantly sensitive to contaminants, such as air and moisture. Thus electrode samples are required to remain in an inert atmosphere during transportation to analytical instruments and during the measurements themselves, which is very difficult to accomplish. If air and moisture contamination are permitted, then the results will be suspect. In contrast, electrode cross-sectional morphologies as viewed by SEM imaging are less affected, as more exposure time to contaminants is required to cause large microstructural changes. Therefore, in this study, failure mechanisms of Si-alloy electrodes using three different polymeric organic binders, PVDF, LiPAA, and CA, were studied via SEM imaging. A quantitative relationship was established between particle surface erosion and cell electrochemical performance.

6.2 Experimental

Neat V7/CA coating was prepared by mixing Si alloy V7 (D50: 0.91 μm , (D90-D10)/D50: 4.70), and CA (anhydrous, 99.5+%, Alfa Aesar) in a weight ratio of 9:1. The slurry was mixed using PG ($\geq 99.5\%$, Sigma-Aldrich) to achieve an appropriate viscosity in a planetary mill (Retsch PM200) at 100 rpm for 1 hour with three 0.5-inch tungsten carbide balls and then spread onto 15 μm thick copper foil with one layer tape having a thickness of ~ 0.002 inch to control the electrode loading. Neat V7/LiPAA coating was prepared by mixing Si-alloy and aqueous LiPAA solution, prepared from neutralizing PAA ($M_w = 250,000$, Sigma-Aldrich) solution with lithium hydroxide ($\text{LiOH}\cdot\text{H}_2\text{O}$, $\geq 98\%$, Sigma-Aldrich), in the same weight ratio. Neat V7/PVDF coating using NMP (anhydrous 99.5%, Sigma-Aldrich) as a solvent was also made for reference. Coatings were stored in air at room temperature overnight and then dried for 30 mins at 120 $^\circ\text{C}$ in air. Electrode disks with an area of 1.30 cm^2 were punched from the coatings after drying and then heated under vacuum at 120 $^\circ\text{C}$ overnight before cell making. The mass loading of pure V7 electrodes was ~ 2 mg/cm^2 , corresponding to a specific capacity of ~ 2.4 mAh/cm^2 .

Coin cell assembly and electrochemical tests were the same as described in the Chapter 3 experimental section. After 20, 40, 60, 80, and 100 cycles, V7/CA and V7/LiPAA cells were opened in an Ar-filled glove box, and the electrodes were rinsed with dimethyl carbonate (DMC, BASF) three times to remove remnant electrolyte solvent and salts. V7/PVDF electrode after 100 cycles was also obtained for reference. Pristine and post-cycled V7/CA, V7/LiPAA, and V7/PVDF electrodes were cross-sectioned using a cross-section polisher (JEOL, IB-19530CP). Cross-sectional morphologies were characterized using a scanning electron microscope (SEM, TESCAN MIRA3) with an accelerating

potential of 5 kV. To abate air exposure, a desiccator was used to transfer cycled electrode samples to and from the cross-section polisher, and a stream of argon gas was flowed over air-sensitive electrodes during the sample loading procedure for the cross-section polisher and SEM. Alloy particle sizes were measured by a laser scattering particle size distribution analyzer LA-950V2.

6.3 Results and Discussion

Figure 6.1 shows the electrochemical performance of neat V7 electrodes using different organic binders. The CA electrode shows the highest capacity retention over 100 cycles, which can be explained by a higher functional group density of CA binder that leads to a stronger self-healing effect^{73,87} and thus enhanced performance. In the case of PVDF electrodes, alloy particles could be fully lithiated during the first discharge process because as they expand during lithiation, strong compressive forces maintain good contact between the particles. However, during charge, the alloy particles contracted and become disconnected from each other. This results in a low capacity retention and a small first cycle CE. The low discharge capacity of the V7/PVDF electrode shown in Figure 6.1(a) (~10% of its original delithiation capacity remained over 100 cycles, the first specific lithiation and delithiation capacities are ~200 mAh/g and ~20 mAh/g, respectively) is therefore not from the Li ions alloying with Si but from capacitance. The CE of the V7/PVDF electrode is not plotted because the particles were isolated after the initial cycle and therefore its value has little meaning.

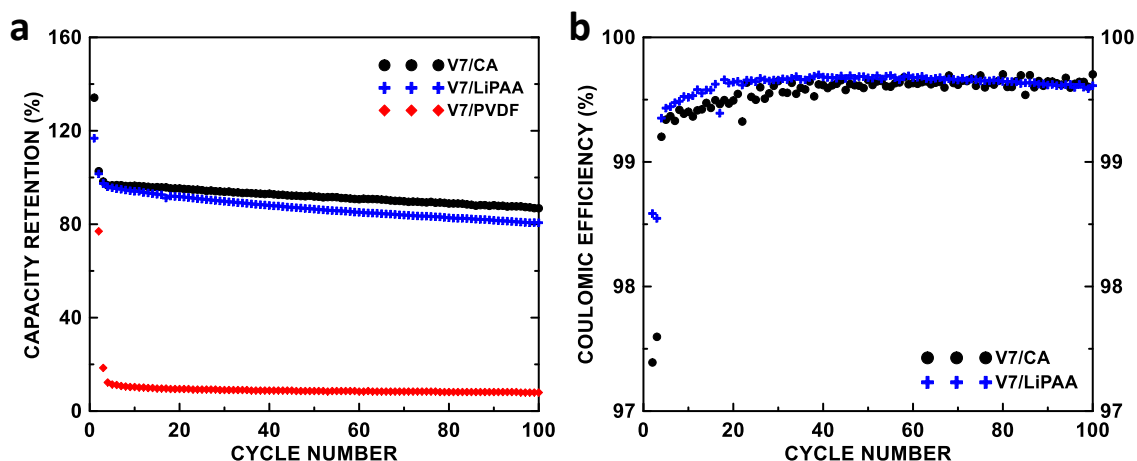


Figure 6.1 (a) Capacity retention vs. cycle number for V7/CA, V7/LiPAA, and V7/PVDF electrodes. (b) CE for V7/CA and V7/LiPAA electrodes.

Values of the capacity retention, the first CE, and the average CEs (from the second cycle) for each cell tested are summarized in Table 6.1. The low first CE of CA electrode is possibly from the reduction of H^+ to generate $H_2(g)$ during the initial discharge. The average CE of all alloy electrodes after different cycles is $<99.65\%$. These values are low compared to what can be achieved with graphite electrodes ($\sim 99.95\%$). This is likely due to alloy surface erosion, leading to the formation of new alloy surfaces and high alloy surface areas that can continuously consume electrolyte to form SEI. Generally, CA electrodes have a lower CE but a higher capacity retention compared to LiPAA electrodes, because alloy particles surrounded by CA binder might undergo more severe parasitic reactions on their surfaces which yields the lower CE, however, the larger amount of the generated SEI did not lead to the particle isolation, thus a better capacity retention can be achieved by the maintenance of particle electrical connections.

Table 6.1 Cycling performance of V7/LiPAA, V7/CA, and V7/PVDF electrodes after different cycles.

Cells	Capacity Retention (%)	First CE (%)	Average CE (%) (from the 2 nd cycle)
V7/LiPAA (20)	97.54	83.42	99.48
V7/LiPAA (40)	97.00	83.21	99.41
V7/LiPAA (60)	89.26	85.80	99.61
V7/LiPAA (80)	86.03	85.53	99.62
V7/LiPAA (100)	80.65	85.61	99.61
V7/CA (20)	96.48	71.30	99.14
V7/CA (40)	90.81	73.36	99.38
V7/CA (60)	91.58	72.33	99.46
V7/CA (80)	85.98	73.68	99.34
V7/CA (100)	86.81	74.40	99.54
V7/PVDF (10)	5.44	14.79	N/A
V7/PVDF (20)	6.58	13.09	N/A
V7/PVDF (100)	7.96	12.31	N/A

Figures 6.2-6.4 show the acquired BSE images of V7/LiPAA, V7/CA, and V7/PVDF electrodes after different cycles, respectively. There were three main components in images of cycled electrodes: alloy particles (bright), SEI surrounding them (grey), and porosity (black).

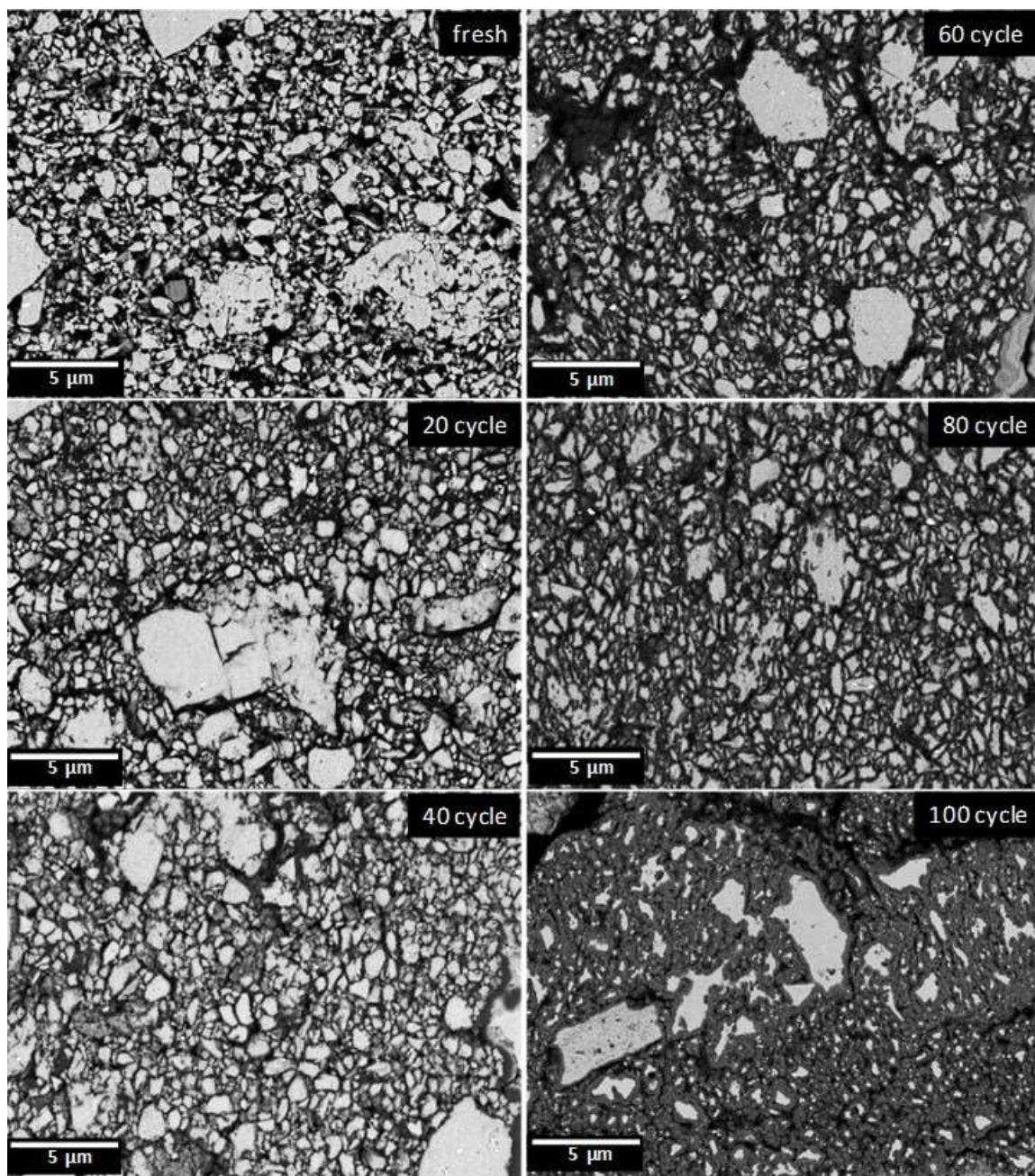


Figure 6.2 BSE images of V7/LiPAA electrodes after different cycles without image processing.

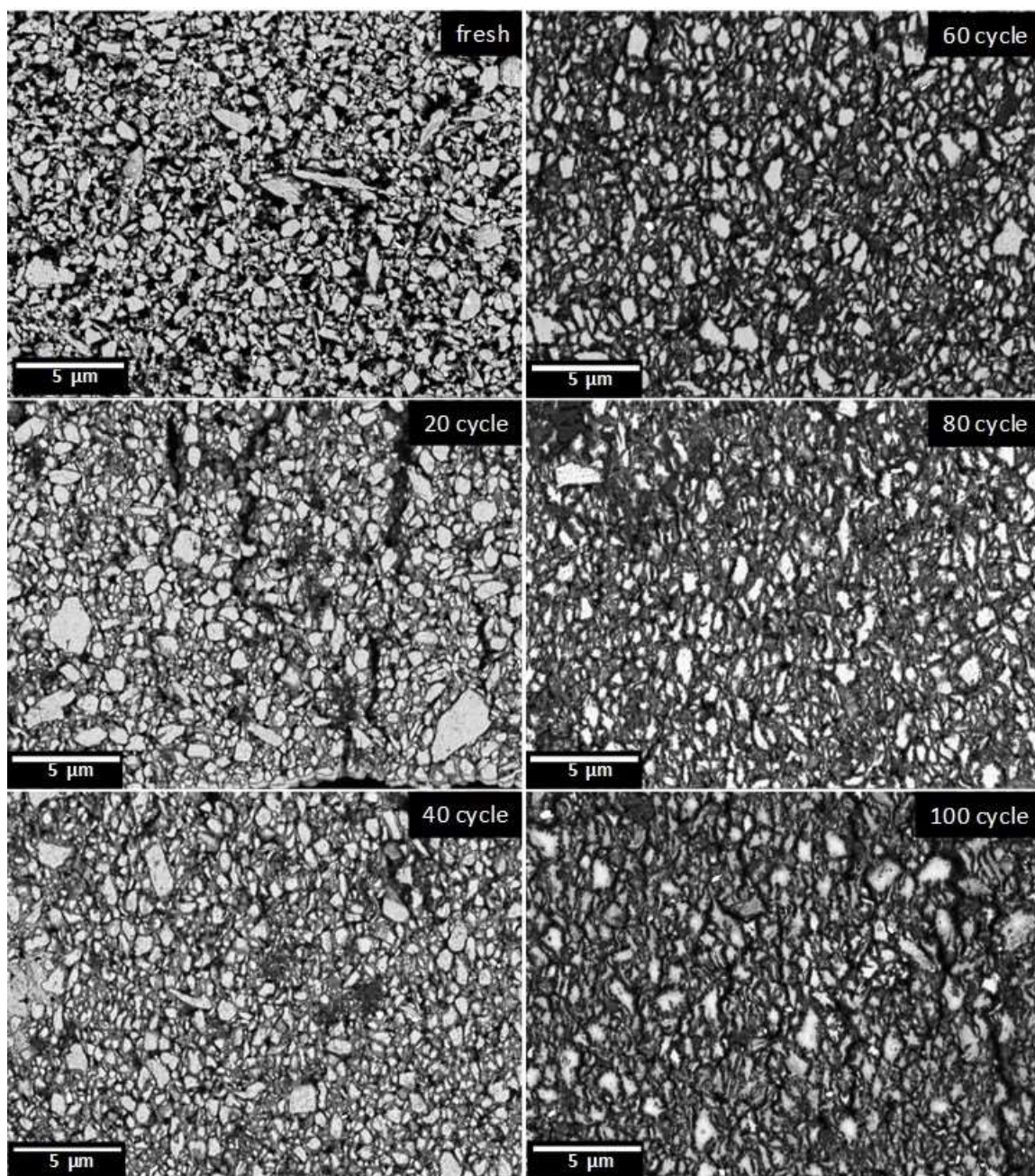


Figure 6.3 BSE images of V7/CA electrodes after different cycles as indicated without image processing.

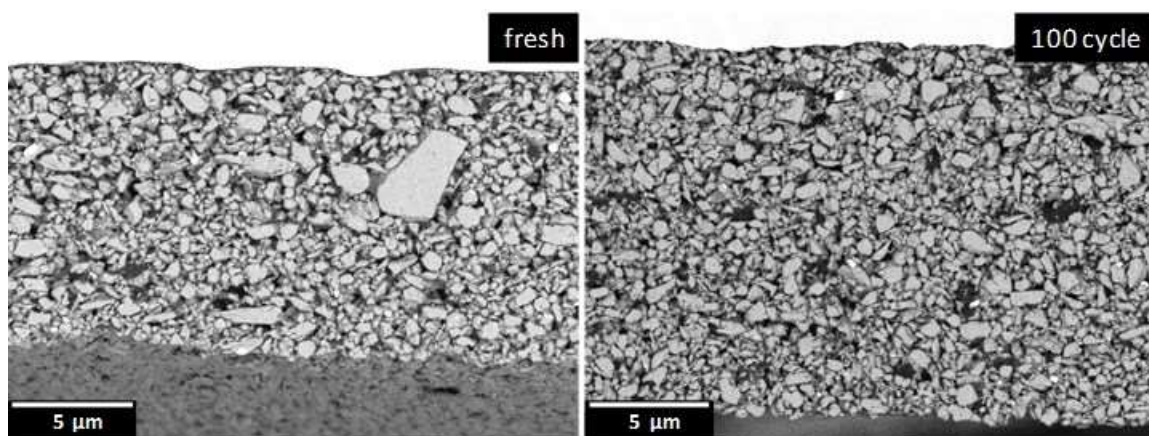


Figure 6.4 BSE images V7/PVDF electrodes after different cycles as indicated without image processing.

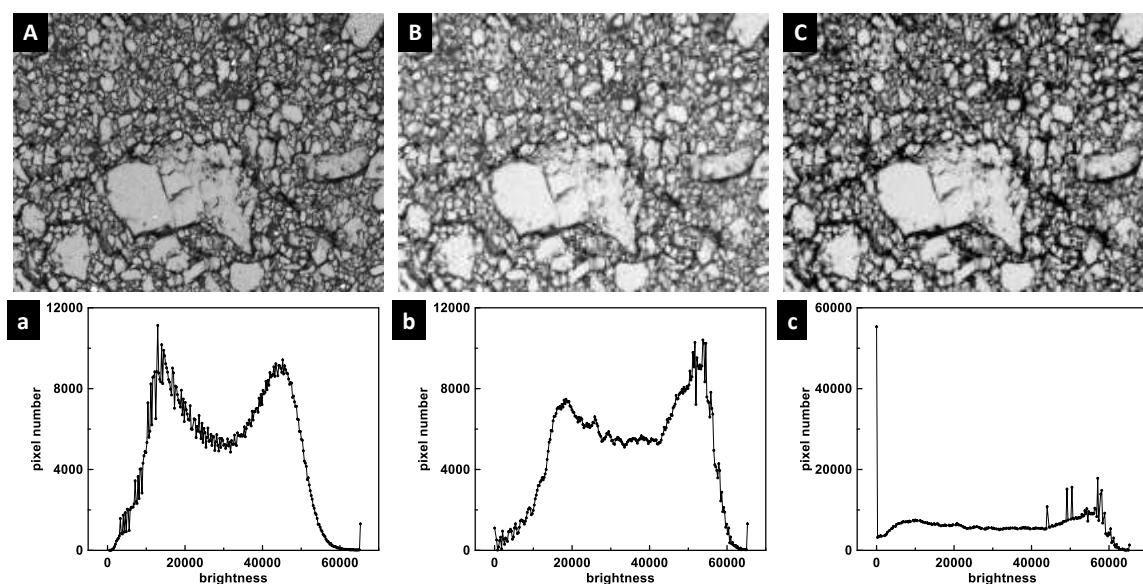


Figure 6.5 (A) An original BSE image of a neat V7 electrode obtained by SEM. (B) Brightness of image A increased by 40%. (C) Contrast of image A increased by 40%. (a-c) Corresponding histogram of image A-C.

Quantitative analysis was directly based on the histogram of the brightness distribution of each image obtained. However, it was found that the histogram curves of each BSE image were composed of broad peaks that could not easily be separated (see Figure 6.5(a)). The broader peak at the lowest brightness comprised both porosity and SEI information. Additionally, the histogram peak shapes were highly dependent on the

apparent brightness and contrast of the image. Figure 6.5(A-C) shows how the histogram curve changes as the image brightness and contrast change. Here, a BSE image of V7/LiPAA electrode after 20 cycles (Figure 6.5(A)) was taken as an example. If the brightness of the image was increased by 40% (Figure 6.5(B)), then both peaks shifted to the right and the peak at higher brightness became larger (Figure 6.5(b)). If the contrast of the image was increased by 40% (Figure 6.5(C)), then the two peaks moved to either side, and their peak areas increased. In addition to these effects, the images acquired were focused by focusing the electron beam, which altered the physical working distance between the sample surface and the electron gun, leading to inconsistent image properties between different samples even though they are acquired at the same brightness and contrast setting. All factors mentioned above limited the ability to separate contributions from the alloy particles, SEI, and porosity in the histograms of the post-cycled electrode images. For this reason, it was not possible to obtain consistent and quantitative amounts of all three of these components from the histograms of the unprocessed SEM images.

Considering these limitations, a method of quantitatively obtaining the relative amount of alloy in the images was devised, based on simply increasing the image contrast of BSE images, so that pixels either appeared as white (alloy) or black (not alloy, i.e. porosity or SEI). This is demonstrated for a cycled V7/LiPAA electrode in Figure 6.6(A and B). After processing, only two data points were observed in the histogram (see Figure 6.6(b)), the point at low brightness represents the pixel number of both SEI and electrode porosity components, and the point at high brightness represents the pixel number of the alloy particles.

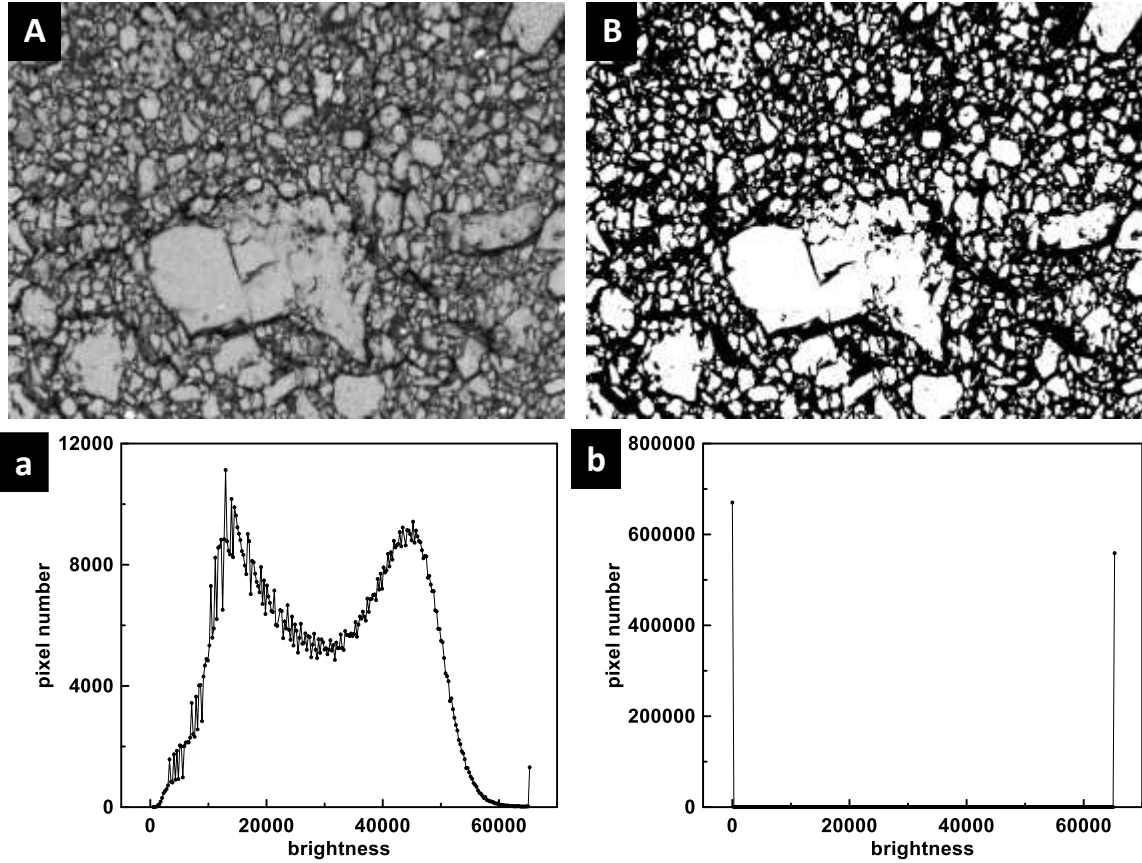


Figure 6.6 (A) A cross-sectional BSE image of a V7/LiPAA electrode after 20 cycles (B) Image (A) processed by increasing the contrast to the maximum. (a) and (b) Corresponding histograms of image (A) and (B), respectively.

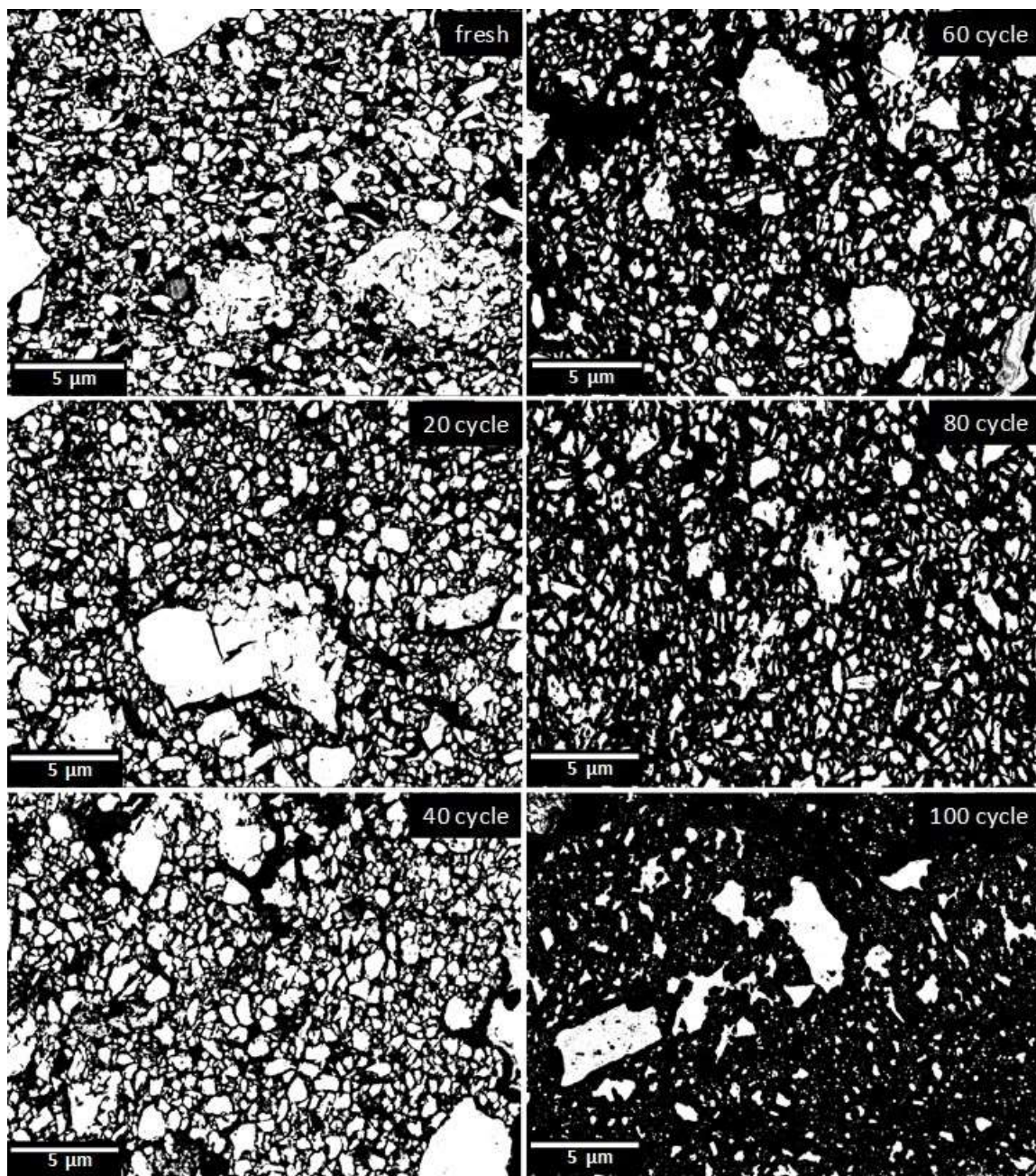


Figure 6.7 Processed cross-sectional BSE images of V7/LiPAA electrodes after different cycles as indicated.

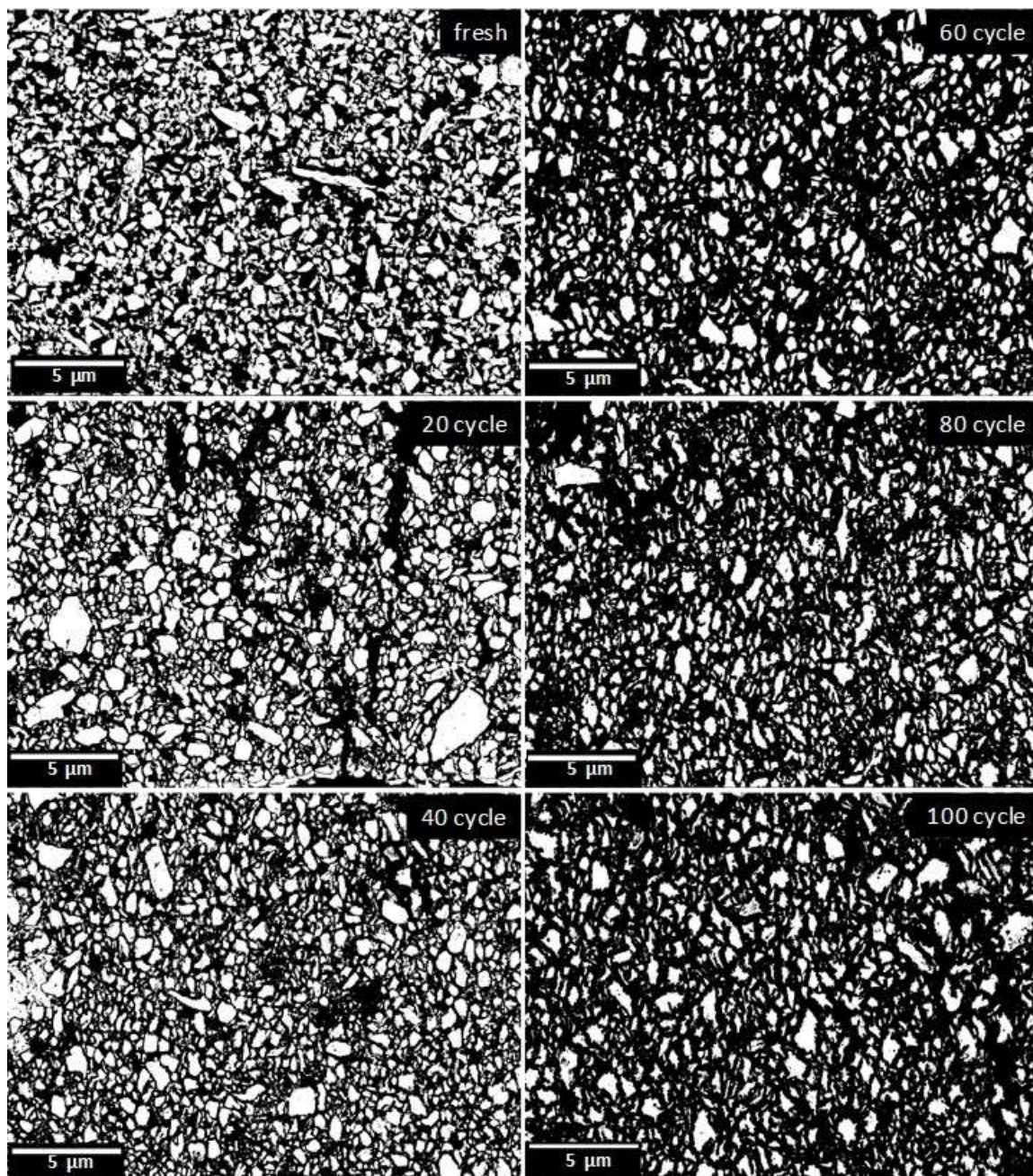


Figure 6.8 Processed cross-sectional BSE images of V7/CA electrodes after different cycles as indicated.

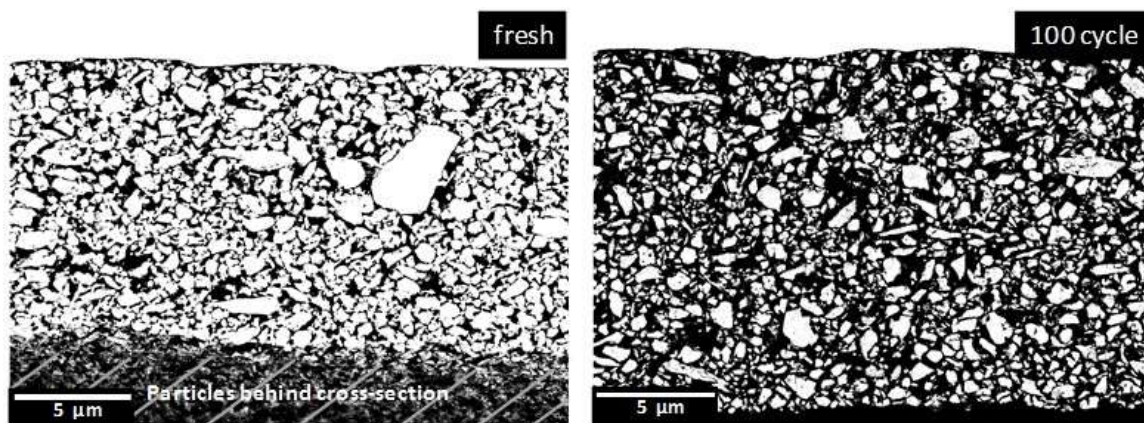


Figure 6.9 Processed cross-sectional BSE images of V7/PVDF electrodes after different cycles as indicated.

Figures 6.7-6.9 show processed BSE images of pristine and post-cycled V7/LiPAA, V7/CA and V7/PVDF electrodes, respectively. The final alloy volume fraction of V7/LiPAA and V7/CA electrodes after different cycles, as determined by the percent alloy pixels in SEM images after image processing, are shown in Figure 6.10. The error bars shown represent the standard deviation of the alloy volume fraction obtained from multiple images acquired from each sample. This error resulted from variations such as alloy particle size distribution and electrode porosity. A post-cycled V7/PVDF electrode was cross-sectioned at a state where most of its lithiation capacity had not been released, implying that there must be a particle volume increase. However, the alloy volume fraction after 100 cycles (~44%) was similar to the initial value (~48%), implying a simultaneous porosity volume fraction increase, since no obvious SEI growth was observed. Particles of the poor-performing PVDF electrode remain pristine, because they didn't undergo actual lithiation/delithiation after the initial cycle. Both LiPAA and CA coatings had an initial alloy ratio of ~45%, corresponding to an initial porosity of ~55%, which is typical of hand-coated alloy electrodes.¹¹ However, during cycling, the alloy volume fraction decreases approximately linearly. After 100 cycles, the alloy volume fraction is only 10-20%. The

alloy volume fraction decrease likely results from continuous alloy fracture as the cycle number increases, leading to the generation of fresh particle surfaces and thus SEI growth. Fracture and particle expansion would also increase electrode porosity. Both effects dilute the alloy volume fraction in the same imaging area. The continuous SEI growth indicates that better-performing binders could not prevent mechanical fractures of Si-based materials during cycling which is in contrary to the conclusion drawn by previous research.^{24,88} SEI volume fraction change is also of high interest, further image analyses are required to obtain this quantity.

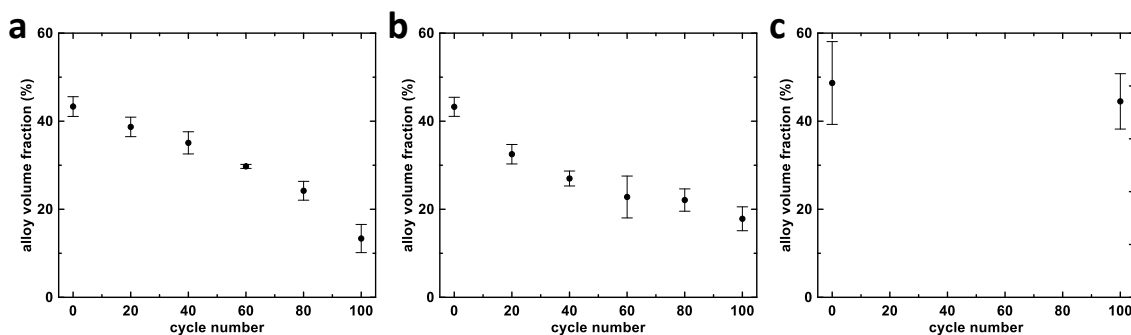


Figure 6.10 Alloy volume fraction vs. cycle number for pristine and post-cycled (a) V7/LiPAA electrodes, (b) V7/CA, and (c) V7/PVDF electrodes.

6.4 Conclusion

This study introduces a quantitative analysis method to investigate mechanical fade mechanism of neat alloy electrodes using different binders (LiPAA, CA, and PVDF) via SEM imaging. Electrodes using PVDF binders show little delithiation capacity due to particle contraction, alloy particles were isolated and did not undergo expansion and contraction thus distinct particle edges were observed. Electrodes with LiPAA and CA binders present good cycling performance, which implies good electric connection between particles during cycling. However, a continuous decrease in alloy volume fraction

was observed, with less than 20% of alloy volume shown in BSE images after 100 cycles, indicating enormous SEI and porosity growth as cycle number increases. This shows that LiPAA and CA binders possess limited ability to control alloy fracture and SEI growth during cycling.

It is worth pondering why the use of functionalized binders could help the maintenance of the electronic association between alloy particles despite their fracture and being covered by a thick SEI layer. This is a serious problem, since SEI growth resulting from the side reactions during repeated expansion and contraction of alloy particles would finally exhaust the active Li ions in full cells. An ideal SEI should be thin and dense, having the capability to inhibit particle fracture and simultaneously achieve good cycling. Untreated alloy particles have high reactivity towards electrolyte and large volume expansion compared to carbon or graphite materials, and thus do not form a stable SEI during cycling. Therefore, new methods, such as carbon coating⁸⁹ of high energy density materials, might be needed to prevent severe parasitic reactions on particle surfaces.

Chapter 7 INORGANIC COMPOUNDS AS BINDERS FOR SI-ALLOY ANODES

7.1 Introduction

As introduced in Chapter 1, inorganic binders have been used for Li-ion batteries due to their low cost, high electrochemical and thermal stability, and compatibility with water as a slurry solvent. The use of such binders in alloy anodes has not been previously reported. In this chapter, three inorganic binders of interest, lithium polysilicate ($\text{Li}_2\text{Si}_5\text{O}_{11}$), sodium polyphosphate ($(\text{NaPO}_3)_n$), and lithium phosphate monobasic (H_2LiPO_4) were investigated as binders for pure Si-alloy and pure graphite anodes. These electrodes were characterized for their electrochemical performance and their microstructure was investigated before and after electrochemical cycling.

7.2 Experimental

Binders evaluated in this study were Li polysilicate (20 wt% in H_2O , Sigma-Aldrich), sodium polyphosphate (sodium hexametaphosphate, 65-70% P_2O_5 basis, Sigma-Aldrich), and lithium phosphate monobasic (99%, Sigma-Aldrich). Neat Si alloy electrode slurries were prepared by mixing Si alloy (V7 alloy, 3M Company) and binder in a weight ratio of 9:1. Distilled water was added to control slurry viscosity. Graphite (MAGE, Hitachi) slurries were made in the same method, but with the addition of ~ 0.1 mL isopropylene alcohol to improve wetting. Slurries were mixed in a Mazerustar mixer at 5000 rpm for 10 minutes and then spread onto 15 μm thick copper foil with a 0.004-inch coating bar. All coatings were stored in air at room temperature overnight and then dried for 30 mins at 120 $^\circ\text{C}$ in air. TiN (< 3 μm , density: 5.24 g/mL, Aldrich) coatings were also prepared to measure the electrochemistry of binders without interference from an active material.

Electrode disks with an area of 1.30 cm² were punched from the coatings after drying and heated under vacuum at 120 °C overnight and transferred without air exposure to an Ar-filled glovebox for cell making. The mass loadings were ~2 mg/cm² and ~3 mg/cm² for neat V7 and graphite electrodes, respectively, corresponding to specific capacities of and ~2.4 mAh/cm² and ~1.1 mAh/cm², respectively.

Coin cell assembly and electrochemical test methods were the same as described in the experimental section of Chapter 3. Pristine and post-cycled neat V7 and graphite electrodes were cross-sectioned using a cross-section polisher (JEOL, IB-19530CP) and characterized using a scanning electron microscope (SEM, TESCAN MIRA3) with an accelerating potential of 5 kV. To abate air exposure, a desiccator was used to transfer cycled electrode samples to the cross-section polisher, and a stream of argon gas was flowed over the post-cycled electrodes during the sample loading procedure for the cross-section polisher and SEM. True density of binders (sodium polyphosphate and lithium phosphate monobasic) was measured by a Micromeritics AccuPyc II 1340 gas pycnometer with a dry helium atmosphere.

7.3 Results and Discussion

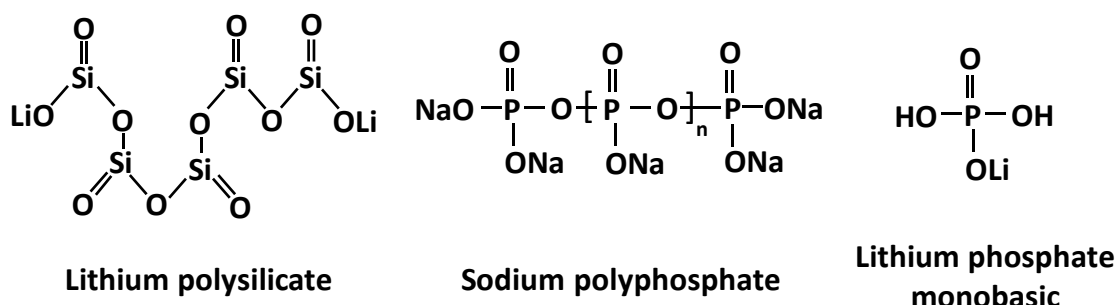


Figure 7.1 Structures of the inorganic binders investigated in this study.

The structures of the inorganic binders investigated in this study are depicted in Figure 7.1. It is worth noting that the Si=O double bonds are extremely reactive in water and tend to hydrolyze, as shown in Figure 7.2(a).^{90,91} Lithium polysilicate and sodium polyphosphate are polymers that possess bridging and non-bridging oxygen atoms, lithium phosphate monobasic is a small molecule with solely non-bridging oxygen atoms and acidic protons. Figure 7.2(b) shows the proposed mechanism of condensation of hydroxyl groups of silicate species and hydroxyl groups on the Si-alloy particle surfaces leading to the formation of covalent silicate-Si bonding (Si-O-Si), which is similar to the carboxylic acid connected to Si.⁹² Phosphate species possibly undergo a similar reaction.

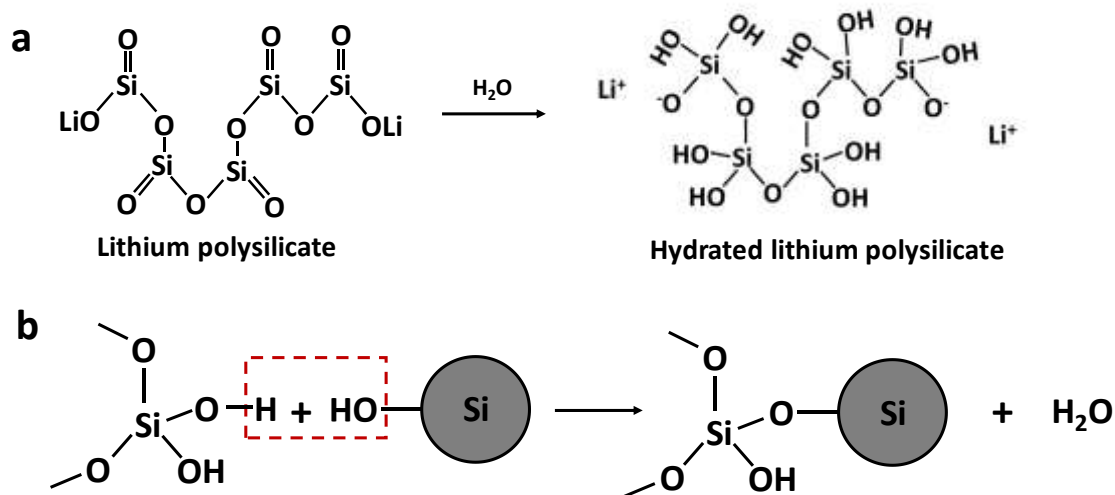


Figure 7.2 (a) Lithium polysilicate conversion to hydrated lithium polysilicate. (b) Proposed mechanism of hydrated lithium polysilicate connected onto the particle surface.

The alloy electrode slurries prepared using these inorganic binders resulted in homogeneous coatings as shown in Figure 7.3(a-c). However, poor electrode integrity resulted when the binder was used with graphite. Portions of the coating sloughed from the electrodes when electrodes were punched. Given the poor quality of these graphite coatings with 10 wt% binder (see Figure 7.3(d-f)), neat graphite coatings were remade with a higher

binder fraction of 20 wt% to measure their electrochemical characteristics. As can be seen in Figure 7.3(g-i), graphite electrode quality was significantly improved by increasing the binder fraction. However, binder solution separation from the graphite particles was also severe due to the low viscosity of the aqueous electrode slurry, especially for the LiH_2PO_4 coating, for which white crystals were observed on the Cu foil surface after drying.

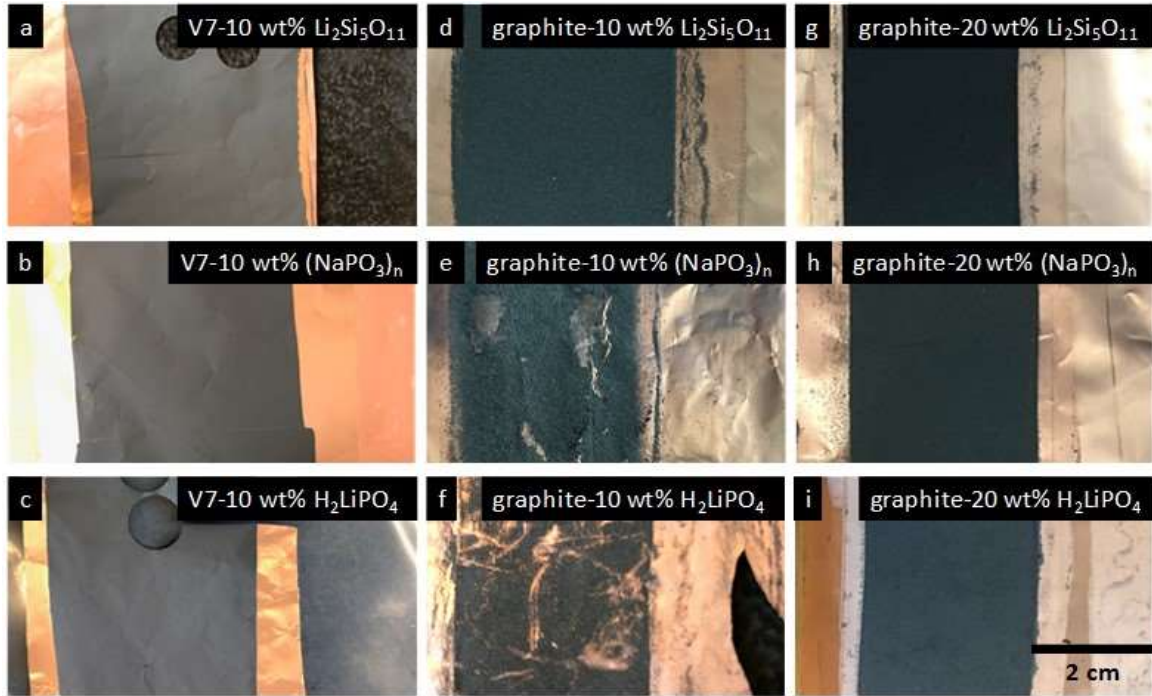


Figure 7.3 Digital photographs of (a-c) neat Si alloy and (d-i) neat graphite coatings prepared with $\text{Li}_2\text{Si}_5\text{O}_{11}$, $(\text{NaPO}_3)_n$, and H_2LiPO_4 binders, as indicated.

Electrodes comprised of TiN and binder were prepared to study binder electrochemistry. TiN is electrically conductive and electrochemically inert at low potentials. For this reason, the electrochemical performance of binder can be examined in a composite coating without interference from active materials.⁵⁸

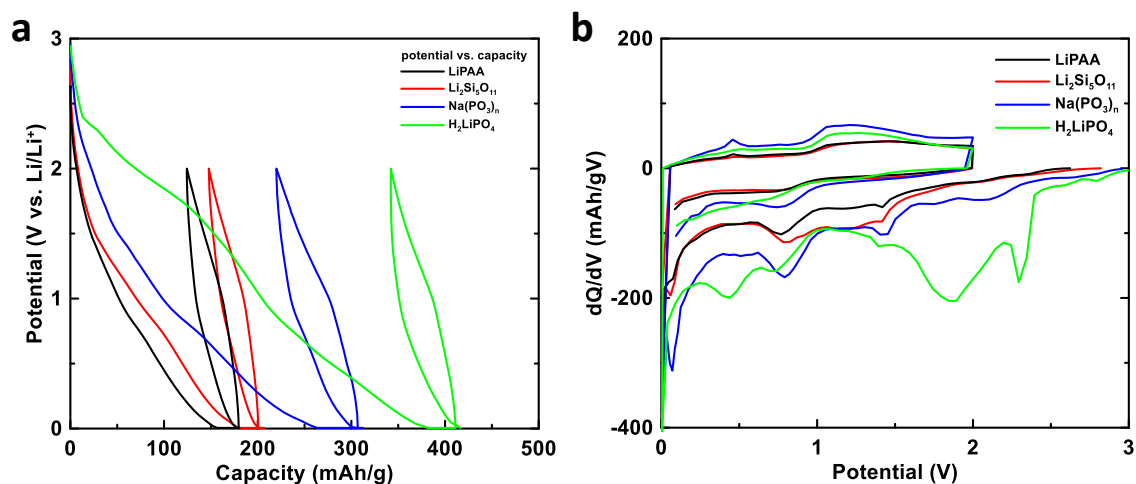


Figure 7.4 (a) Potential curves and (b) differential capacity curves of LiPAA, Li₂Si₅O₁₁, (NaPO₃)_n, and H₂LiPO₄ binders vs. Li-metal as measured in a TiN/binder composite coating.

Figure 7.4(a) shows the first cycle potential curves of LiPAA, Li₂Si₅O₁₁, (NaPO₃)_n, and H₂LiPO₄ binders in TiN/binder electrodes where the TiN/binder weight ratio is 9/1, corresponding to a TiN/binder volume ratio of 73/27, 80/20, 81/19, and 79/21 for the TiN/LiPAA, TiN/Li₂Si₅O₁₁, TiN/(NaPO₃)_n, and TiN/H₂LiPO₄ electrodes, respectively. Volume fraction of each electrode component was obtained based on the densities listed in Table 1. The initial lithiation capacities of LiPAA, Li₂Si₅O₁₁, (NaPO₃)_n, and H₂LiPO₄ binders are 180, 201, 307, and 411 mAh/g respectively, and the first cycle reversible capacities are 55, 53, 87, and 69 mAh/g respectively. The large first lithiation capacity of H₂LiPO₄ binder is likely due to its reduction to generate H₂, because H⁺ of the H₂LiPO₄ electrode possesses the highest potential vs Li/Li⁺. All binders show very small reversible capacities (~25 mAh/g) compared to the V7 Si alloy theoretical capacity of ~1200 mAh/g. After the first lithiation process, all binders show a similar electrochemical behavior to PVDF, which is considered to be electrochemically inert.⁵⁸ Therefore, the reversible capacity measured may not be from the binders, but from other sources, e.g. capacitance.

Figure 7.4(b) shows the first one and a half cycle-differential capacity curves of the four binders selected. H_2LiPO_4 electrode shows a broad peak at ~ 2 V, presumably due to H^+ reduction. Other binders exhibit smaller peaks in their differential capacity curves, which may be from the reduction of impurities (e.g. water) and the decomposition of electrolyte salts and organic solvents.⁹³

Table 7.1 Densities of electrode component materials in g/cm^3 .

	TiN	LiPAA	$\text{Li}_2\text{Si}_5\text{O}_{11}$	$(\text{NaPO}_3)_n$	H_2LiPO_4	MAGE
Density	5.24	1.54 ¹¹	2.27 ⁹⁴	2.52	2.16	2.26 ¹¹

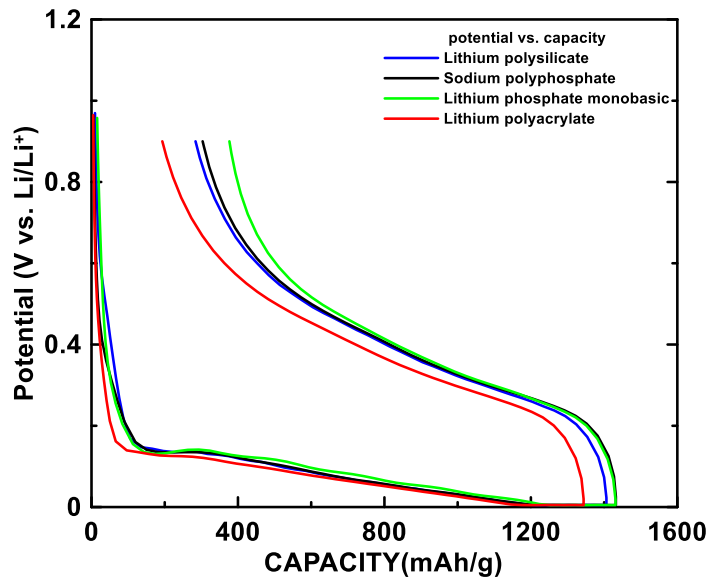


Figure 7.5 The first cycle potential vs. capacity curves of neat V7 electrodes with $\text{Li}_2\text{Si}_5\text{O}_{11}$, $(\text{NaPO}_3)_n$, H_2LiPO_4 , and LiPAA binders, respectively.

Figure 7.4 shows the potential vs. capacity curves for pure V7 electrodes with inorganic binders and commonly-used LiPAA organic binder. All potential profiles show a nucleation plateau at ~ 0.16 V and two characteristic sloping plateaus of Si that are described in Chapter 1. The ICE values of the electrodes with $\text{Li}_2\text{Si}_5\text{O}_{11}$, $(\text{NaPO}_3)_n$, H_2LiPO_4 , and LiPAA binders, were 80%, 79%, 74%, and 86%, respectively. The lowest

ICE is that of the V7- H_2LiPO_4 electrode, which is possibly due to the reduction of hydrogen from the H_2LiPO_4 binder to form H_2 gas.

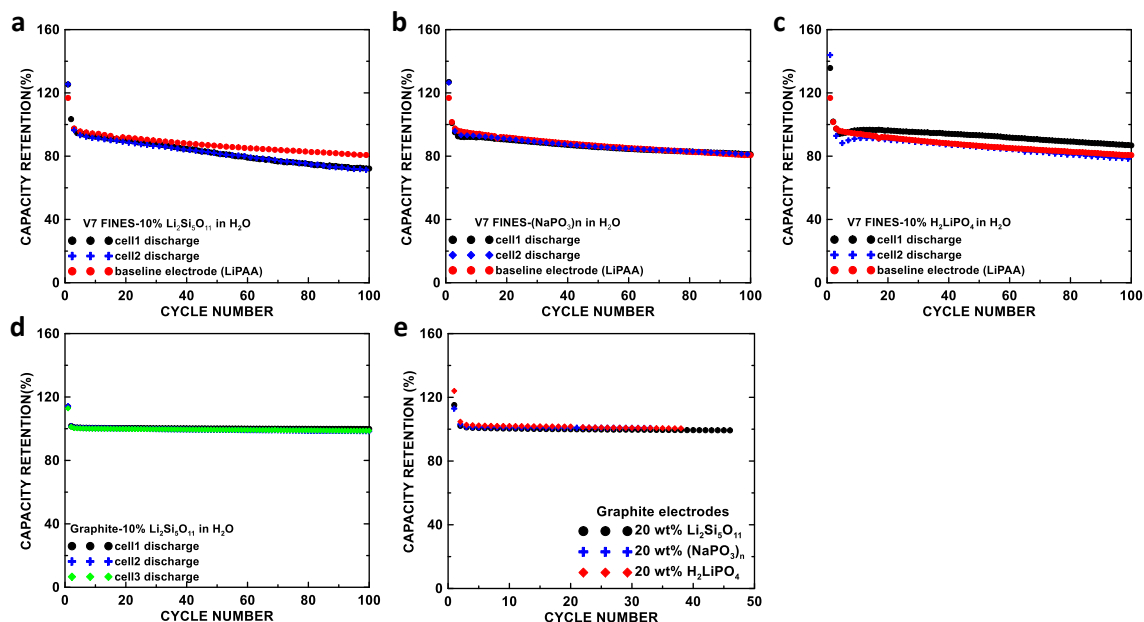


Figure 7.6 Cycling performance of (a) V7- $\text{Li}_2\text{Si}_5\text{O}_{11}$, (b) V7- $(\text{NaPO}_3)_n$, (c) V7- H_2LiPO_4 , (d) graphite- $\text{Li}_2\text{Si}_5\text{O}_{11}$ and (e) graphite-20 wt% inorganic binders electrodes. The electrochemical performance of V7 electrodes using inorganic binders was shown with the comparison of a V7-LiPAA electrode.

Figure 7.6 shows the capacity vs. cycle number of V7 or graphite in electrodes with $\text{Li}_2\text{Si}_5\text{O}_{11}$, $(\text{NaPO}_3)_n$, or H_2LiPO_4 binder. Duplicate cells were used to confirm the electrochemical performance. Compared to the performance of a V7-LiPAA electrode, all alloy cells with inorganic binders showed similar cycling results. V7- $\text{Li}_2\text{Si}_5\text{O}_{11}$, V7- $(\text{NaPO}_3)_n$, and V7- H_2LiPO_4 electrodes showed a capacity retention of 71.75%, 81.05%, and 82.56%, respectively. Cells using polymeric $\text{Li}_2\text{Si}_5\text{O}_{11}$ and $(\text{NaPO}_3)_n$ binders showed good cycling repeatability. However, the reproducibility of H_2LiPO_4 cells were poor. It was mentioned in Chapter 4 and 5 that when small molecules serve as binders in cells, proper slurry viscosity is necessary to guarantee repeatable cells cycling performance. Therefore,

the low viscosity of the aqueous slurry using a molecular binder H_2LiPO_4 likely leads to an uneven coating and thus cells with poor reproducibility.

Graphite electrodes using 10 wt% or 20 wt% inorganic binders show good electrochemical performance. Despite the poor coating quality of the graphite- $\text{Li}_2\text{Si}_5\text{O}_{11}$ (10 wt%) electrodes, they had excellent cycling with 99% capacity retention after 100 cycles. As shown in Chapter 1, graphite electrodes can have superb performance even without binder. However, the incapability of these inorganic binders to provide mechanical association with graphite results in fragile coatings that are not practical to handle. Surface treatment of the graphite (e.g. mild oxidation with an acid) may alleviate this issue.

Figure 7.7 shows the morphology of V7 electrodes using inorganic binders before and after cycling. After 100 cycles, the surface of the alloy particles was severely eroded. Many researchers use a surface modification mechanism, including the formation of an artificial SEI layer, to explain the good performance of binders for Si-based materials. However, such a mechanism is hard to understand if the alloy surface is continually eroded away during cycling. Another explanation for the good performance of these binders is that they possess a large amount of oxygen atoms that possibly interact with hydroxyl groups on Si-alloy surfaces, leading to a strong “self-healing” effect, enhancing their ability to bind to fractured alloy particles and keep them electrically and ionically connected.

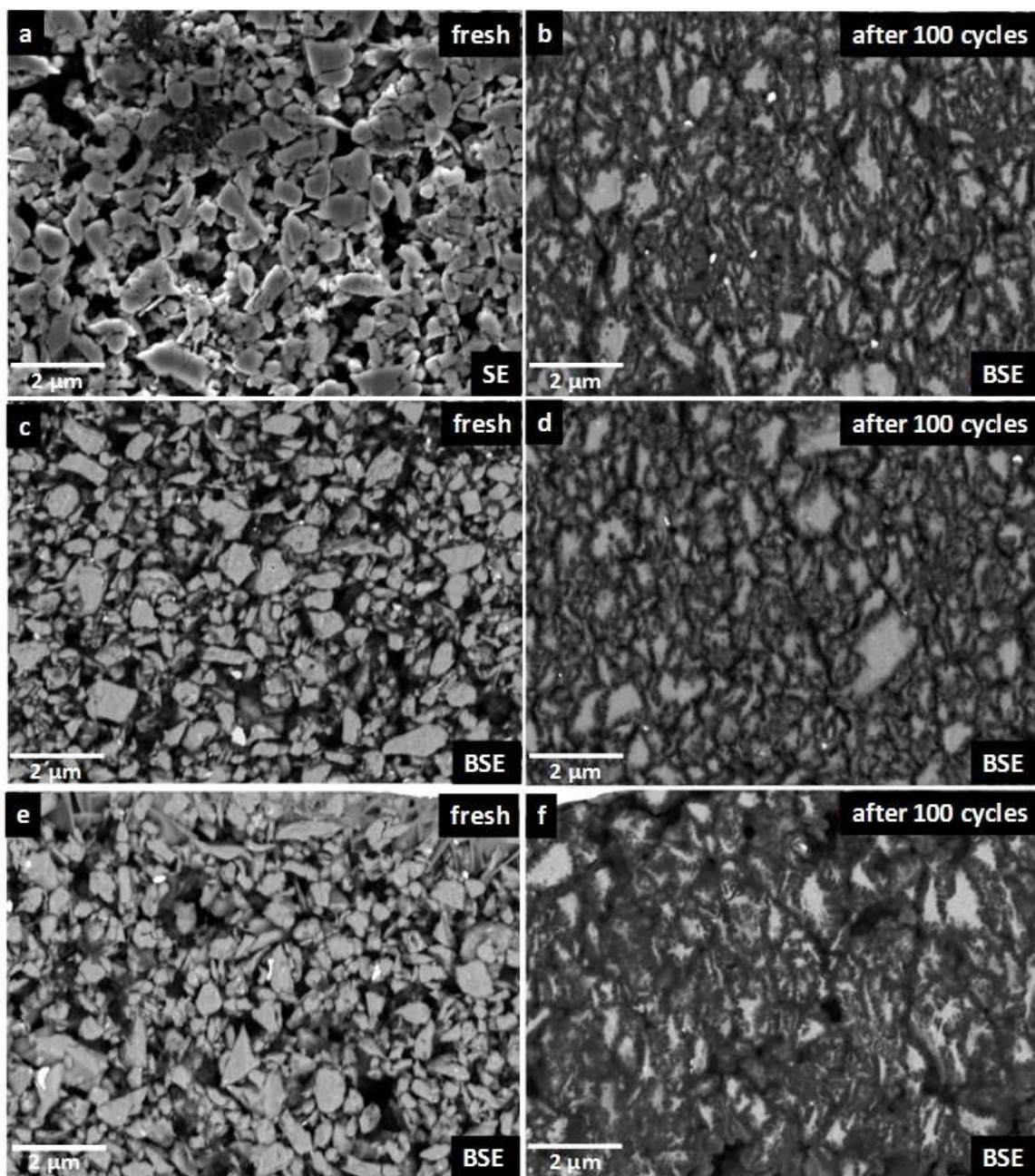


Figure 7.7 SEM images of (a, c, e) pristine and (b, d, f) post-cycled (100 cycles) V7-Li₂Si₅O₁₁, V7-(NaPO₃)_n, and V7-H₂LiPO₄ electrodes, respectively.

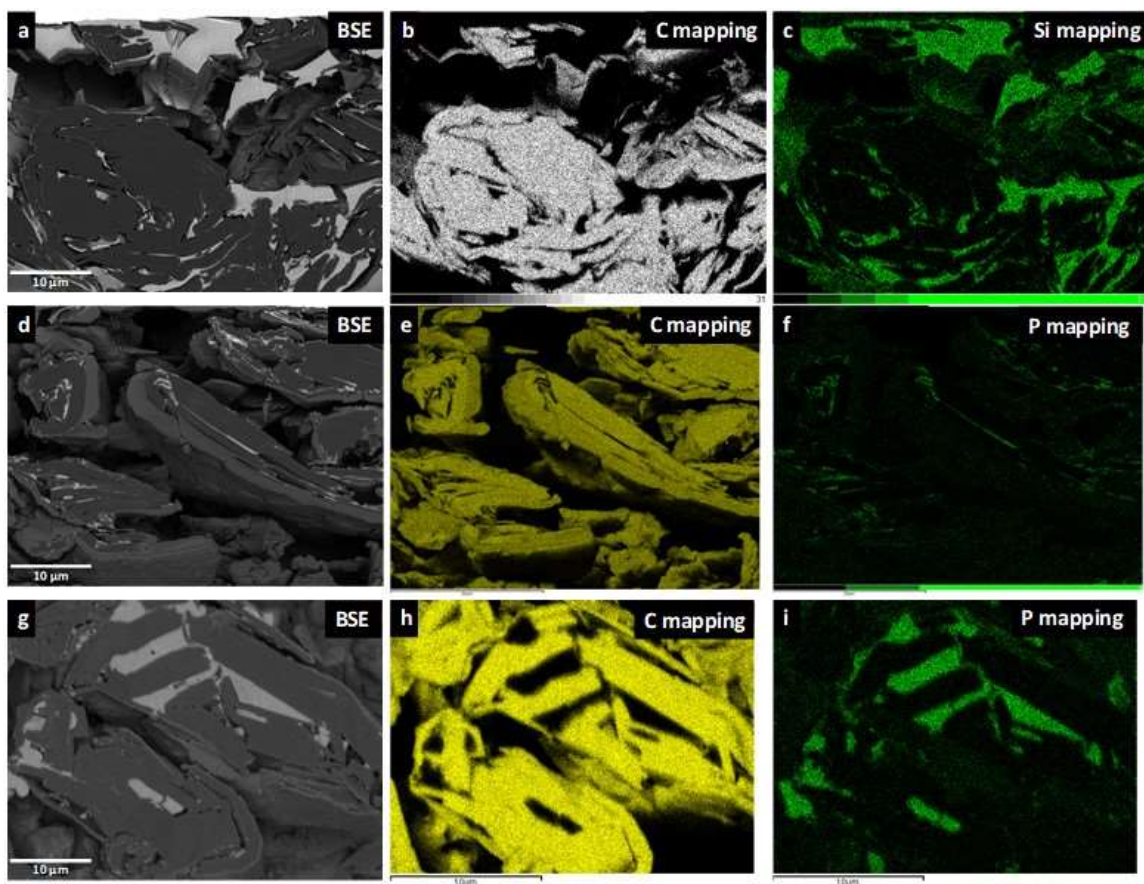


Figure 7.8 (a, d, g) BSE, (b, e, h) C mapping, and (c, f, i) Si/P mapping of pristine graphite- $\text{Li}_2\text{Si}_5\text{O}_{11}$, graphite- $(\text{NaPO}_3)_n$, and graphite- H_2LiPO_4 electrodes, respectively.

Figure 7.8 shows cross-sectional BSE images and element mappings of graphite electrode using $\text{Li}_2\text{Si}_5\text{O}_{11}$, $(\text{NaPO}_3)_n$, and H_2LiPO_4 binders. These images show that the inorganic binders can enter into voids into the graphite particles during the electrode slurry making processes. This was confirmed by the Si mapping for $\text{Li}_2\text{Si}_5\text{O}_{11}$ electrode and the P mapping for both $(\text{NaPO}_3)_n$ and H_2LiPO_4 electrodes. Little binder actually appeared on outer surfaces of the graphite particles, which can explain the observation that these binders fail to physically hold graphite particles mechanically.

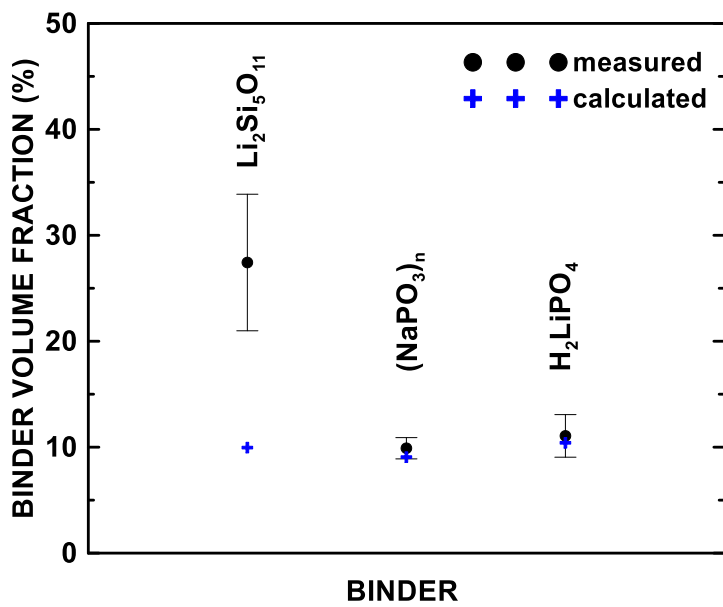


Figure 7.9 Calculated and measured inorganic binder volume fractions in graphite/binder (10 wt%) electrodes.

Figure 7.9 shows the calculated and measured inorganic binder volume fractions in neat graphite electrodes. The calculated volume fractions of inorganic binders are 9.96%, 9.06% and 10.41% for the graphite/ $\text{Li}_2\text{Si}_5\text{O}_{11}$, graphite/ $(\text{NaPO}_3)_n$ and graphite/ H_2LiPO_4 electrodes, respectively, where the graphite/binder weight ratio is 9/1. The measured binder volume fraction for each graphite/binder electrode was obtained based on the cross-sectional SEM images. The error bars shown in Figure 7.8 represent the difference between multiple SEM images acquired from each electrode. The measured binder volume fractions of both $(\text{NaPO}_3)_n$ and H_2LiPO_4 electrodes are in good agreement with the calculated binder fractions. However, in the case of the $\text{Li}_2\text{Si}_5\text{O}_{11}$ electrode, the observed binder fraction is nearly three times greater than the calculated value, indicating that the $\text{Li}_2\text{Si}_5\text{O}_{11}$ binder is very likely to have an open structure, similar to a sol-gel. Considering that electrodes with $\text{Li}_2\text{Si}_5\text{O}_{11}$ cycle with little fade at near theoretical capacity, it is apparent that the large

volume of binder must allow ion diffusion. This suggests that $\text{Li}_2\text{Si}_5\text{O}_{11}$ binder is likely in the form of a porous gel that is filled with electrolyte.

7.4 Conclusion

In this work, three inorganic binders, Li polysilicate, $(\text{NaPO}_3)_n$, and H_2LiPO_4 , were implemented onto both pure Si-alloy and pure graphite electrodes and demonstrated to be efficient binders that enable good cycling performance of the alloy anodes. They have poor adhesion to graphite, however, resulting in graphite coatings that cycle well, but have poor mechanical properties. Increasing binder amounts can improve the graphite coating quality. However, this can sacrifice cell energy density, further studies such as graphite surface treatment are required to enable the use of small amounts of these inorganic binders with graphite. Lithium polysilicate binder has a unique open framework and is likely in the form of an electrolyte-filled gel. Si-alloy electrodes with these inorganic binders had both excellent mechanical properties and cycling performance as good as electrodes made with state-of-the-art LiPAA binder. This implies that the silicic and phosphoric acid groups are just as effective as carboxylic acid groups thought responsible for LiPAA's good performance. These binders represent a brand-new approach for achieving good cycling in Si-alloy electrodes.

Chapter 8 CONCLUSION

8.1 Conclusions

Si-based materials suffer from poor cyclability due to large volume changes during cycling. Binders are considered to play a vital role in the improvement of Si-based materials' electrochemical performance, since they are responsible for functions such as modification of the electrode/electrolyte interface and provision of electrode mechanical integrity. In this thesis, much effort was devoted to improving the alloy cell cycling performance, investigating the effect of binder characteristics such as MW on alloy cycling, and identifying failure mechanisms of Si-alloy materials via SEM imaging. Some new binder systems besides state-of-the-art polymeric organic binders were also explored.

Chapter 3 describes a strategy to improve the cycling of Si-alloy coatings with CMC/SBR binder using small functional molecules as slurry additives. It turned out that binders processing a high density of carboxyl groups, such as NaPAA, Na citrate and Na mellitate, were able to enhance cell electrochemical performance due to the maintenance of electronic connection. It was also observed that more severe alloy particle surface erosion was observed for better performing electrodes, indicating that even well-preformed binders can not prevent particle fracture. Further studies are needed tackle the problem.

In Chapter 4, the effect of NaPAA molecular weight on the cycling performance of pure Si alloy anodes was investigated. It was demonstrated that the binder MW has no relation to alloy cycling performance, as long as good slurry rheological properties are maintained. It was found that cell electrochemical performance was sensitive to electrode slurry rheology and thus seemingly related to binder MW. Aqueous solutions of low MW binders resulted in low slurry viscosity, particle settling, and binder loss during coating,

which could be solved by the addition of a highly viscous solvent PG. Furthermore, PG could be completely removed during drying, so that it had no influence on the final electrode composition. This study shows that thickening can be separated from binder functionality. Electrodes with small MW binders can cycle well by using a high-viscosity slurry solvent like PG to guarantee a homogeneous dispersion of electrode components. This greatly increases alloy electrode binder selection, and could possibly lead to reduced cost and improved performance.

Chapter 5 describes the electrochemical performance of electrodes containing Si-alloys using CA binder. In this study, PG also served as a slurry solvent to enable the use of molecular binders in electrodes comprising Si-alloy by inhibiting particle settling during coating. Therefore, the use of PG eliminated the need of using polymeric binders to maintain good slurry rheology. The high functional group density of CA is beneficial to the cycling of the neat alloy electrodes but simultaneously resulted in alloy particle agglomeration and thus inferior cycling of the composited graphite/alloy electrodes. This study further demonstrates the importance of the binder functionality for alloy cycling and provides more options in terms of binder systems for Si-based anodes.

Chapter 6 describes relations between particle degradation and cell electrochemical performance. In this study, three binders PVDF, CA, and LiPAA were tested as binders for neat Si-alloy electrodes. Electrodes with PVDF binder failed to achieve good cycling due to PVDF's lack of functional groups. Distinct particle edges were observed after 100 cycles, since alloy particle disconnection during cycling, resulted in the isolation of alloy particles. These isolated alloy particles did not undergo expansion and contraction and therefore remained pristine. In contrast, electrodes using heavily functionalized CA and LiPAA

binders had good cycling performance, but the alloy particles were severely eroded after 100 cycles. Failure mechanisms of Si-alloy materials were investigated via SEM imaging. It turned out that CA electrodes which have better electrochemical performance show particle degradation in similar degrees compared to LiPAA electrodes. Particles in both CA and LiPAA electrodes continuously fractured as the cycle number increased. This study indicates that functional binders have a limited ability to reduce parasitic reactions on alloy surfaces and a method of quantifying alloy particle degradation during cycling was established. The reason why functionalized binders are capable to maintain electrode integrity despite particles fracture is still a mystery.

Chapter 7 describes the implementation of three inorganic binders: Li polysilicate, $(\text{NaPO}_3)_n$, and H_2LiPO_4 , for neat Si-alloy and neat graphite electrodes. Si-alloy electrodes with these inorganic binders showed similar excellent mechanical properties and cycling performance compared to the LiPAA binder, implying that the silicic and phosphoric acid groups might be as effective as carboxylic acid groups, which are considered responsible for the good performance of advanced organic binder systems. The bad mechanical properties of graphite electrodes using these inorganic binders could be improved through increasing the binder fraction. It was found that lithium polysilicate binder has a unique open framework and is likely in the form of an electrolyte-filled gel. These binders provide a brand-new approach for achieving good cycling in Si-alloy electrodes.

8.2 Future work

A quantification method studying alloy degradation by SEM imaging showed the importance of keeping SEM measuring conditions constant. The apparent brightness and contrast of the images obtained varied because the images were focused by changing the electron beam instead of adjusting the stage up and down, which leads to the alteration of physical working distance, thereby making the resolution of electrode components, including alloy particles, SEI, and porosity, difficult. In the future, all SEM images should be taken under the same SEM settings, including accelerating potential, magnification, brightness, contrast etc. It is possible that a peak fitting model could be applied to deconvolute the contributions from the different electrode components in the histograms.

For pristine electrodes, electrode cross-sectional images solely contain information of alloy particles and porosity, which is unlikely resolved by simply increasing image contrast to the maximum, since both particles on and behind cross-section can be seen due to a high initial electrode porosity. More precise particle threshold control methods such as adjusting image brightness are required to eliminate possible measurement error. In the case of post-cycled electrodes, particles behind cross-section can be sheltered by the generated SEI, thus alloy volume fraction can be obtained by merely increasing image contrast. The main difficulty lies in separating SEI and porosity in images, which cannot be resolved by histogram of BSE images, since SEI components are complicated and vary in color. EDS elemental mapping might be capable to quantify SEI, since SEI components usually comprise element P, which is excluded in alloy and porosity. Then the rest in images is porosity. In this way, a relatively accurate quantitative result showing alloy and SEI

change in size and amount during cycling can be obtained, which can give researchers an intuitive grasp of the effect of binders or electrolytes on alloys.

It has been demonstrated that the MW of NaPAA binder has little effect on alloy cell cycling when good coating quality is achieved. Whereas to enable the utilization of various polymerization degree binders in alloy electrodes in industry, subtle electrode slurry recipe optimization should be made. Commercial graphite anode slurries often use a PVDF/NMP binder system, the solid content of slurry (including both the active materials and the binder) is typically 60-70 wt%, corresponding to an active material volume fraction of 40-50%. The component volume fraction is more widely used in industry, since the volume related parameters are crucial to the coating drying process which is vital to the component distribution within the electrode which directly effects cell cycling. To reach solid volume fractions in the range of 40-50% in neat alloy electrodes, the V7 alloy weight fraction should be approximately in the range of 70-80%, which is much higher than a solid fraction of 40-60% used in Chapter 4. In the future, the solid content of neat alloy slurries should be set to a constant value (e.g. 70 wt%). Then, different molecular weight binders can be tested consistently with respect to electrode cycling performance.

Slurry viscosity is another key parameter in electrode manufacturing. A proper slurry viscosity is needed to avoid active material settling and binder loss, as mentioned in Chapter 4. It was found that particle settling is not related to the slurry solid content but to the viscosity of the slurry liquid phase (comprising both the dissolved binder and the solvent). Therefore, there are two manners to increase the binder solution viscosity: using a highly viscous solvent such as PG or using a polymeric binder with large MW. Typical slurry viscosity for industry is in the 1700-3500 cPs range with variations depending on

the customer demands such as the loading targets. In this case, the content of both active materials and the binders are fixed. Therefore, more effort should be devoted to exploring a proper H₂O/PG solvent fraction for each NaPAA binder to simultaneously achieve an appropriate slurry liquid viscosity and an appropriate total slurry viscosity.

Graphite/alloy composite anodes using CMC/SBR binders are successfully commercialized at present. The limitation for CA binder implementation in practice is the strong hydrogen bonding between CA molecules, which leads to the agglomeration of alloy particles in the composite electrodes. In the future, improvements such as using binder alkali salts or dispersion agents are required to tackle the alloy agglomeration problem.

Based on the alloy volume fraction quantification, it was found that binders possessing a high functional group density aid in alloy cycling but fail to prevent alloy surface erosion during cycling. New SEI layers were continuously generated without severe impact on the alloy cycling. It is valuable to do some *in situ* analyses to determine the SEI components formed on alloy surfaces to help understand the binder working mechanism. The results of such analyses might give guidance on new binder system development. New materials design such as surface coatings might also be valuable. The continuous fracturing of alloy particles indicates that the previously reported robust SEI layer formed due to FEC additive decomposition can not handle the huge volume change during cycling when alloy particles directly contact electrolytes. A surface coating such as graphite, carbon or components considered vital to a stable SEI might be helpful to buffer the volume changes of alloys during cycling and prevent alloy particles from contacting electrolytes, thus diminishing parasitic reactions that consume active Li ions.

Increasing binder amounts can improve the mechanical properties of graphite/inorganic binder electrodes but simultaneously sacrifice cell energy density. Further studies such as graphite surface treatment are required to enable the use of small amounts of these inorganic binders with graphite. Si-alloy electrodes with inorganic binders (alkali phosphate and alkali silicate) had both excellent mechanical properties and cycling performance as good as LiPAA binders, indicating the possibility of chemical bonding formation between these inorganic binders and alloys. The analysis of generated components during electrode cycling might give aid in understanding the reason why these binders can boost alloy cycling performance.

Bibliography

1. Yang, Z. *et al.* Electrochemical energy storage for green grid. *Chem. Rev.* **111**, 3577–3613 (2011).
2. Zhu, G. N., Wang, Y. G. & Xia, Y. Y. Ti-based compounds as anode materials for Li-ion batteries. *Energy and Environmental Science* **5**, 6652–6667 (2012).
3. Wang, L., Chen, B., Ma, J., Cui, G. & Chen, L. Reviving lithium cobalt oxide-based lithium secondary batteries-toward a higher energy density. *Chemical Society Reviews* **47**, 6505–6602 (2018).
4. Blomgren, G. E. The Development and Future of Lithium Ion Batteries. *J. Electrochem. Soc.* **164**, A5019–A5025 (2017).
5. Winter, M., Barnett, B. & Xu, K. Before Li Ion Batteries. *Chemical Reviews* **118**, 11433–11456 (2018).
6. Obrovac, M. N. & Chevrier, V. L. Alloy negative electrodes for Li-ion batteries. *Chem. Rev.* **114**, 11444–11502 (2014).
7. Ramanujapuram, A. *et al.* Degradation and stabilization of lithium cobalt oxide in aqueous electrolytes. *Energy Environ. Sci.* **9**, 1841–1848 (2016).
8. Liu, Q. *et al.* Approaching the capacity limit of lithium cobalt oxide in lithium ion batteries via lanthanum and aluminium doping. *Nat. Energy* **3**, 936–943 (2018).
9. Obrovac, M. N. & Chevrier, V. L. Alloy Negative Electrodes for Li-Ion Batteries. *Chem. Rev.* **114**, 11444–11502 (2014).
10. Obrovac, M. N., Christensen, L., Le, D. B. & Dahn, J. R. Alloy Design for Lithium-Ion Battery Anodes. *J. Electrochem. Soc.* **154**, A849–A855 (2007).

11. Du, Z., Dunlap, R. A. & Obrovac, M. N. High Energy Density Calendered Si Alloy/Graphite Anodes. *J. Electrochem. Soc.* **161**, A1698–A1705 (2014).
12. Timmons, A. *et al.* Studies of Si_{1-x}C_x Electrode Materials Prepared by High-Energy Mechanical Milling and Combinatorial Sputter Deposition. *J. Electrochem. Soc.* **154**, A865–A874 (2007).
13. Cao, Y., Bennett, J. C., Dunlap, R. A. & Obrovac, M. N. A Simple Synthesis Route for High-Capacity SiO_x Anode Materials with Tunable Oxygen Content for Lithium-Ion Batteries. *Chem. Mater.* **30**, 7418–7422 (2018).
14. Wang, Y., Cao, S., Liu, H., Zhu, M. & Obrovac, M. N. Si-TiN alloy Li-ion battery negative electrode materials made by N₂ gas milling. *MRS Commun.* **8**, 1352–1357 (2018).
15. Cao, Y., Bennett, J. C., Dunlap, R. A. & Obrovac, M. N. Li Insertion in Ball Milled Si-Mn Alloys. *J. Electrochem. Soc.* **165**, A1734–A1740 (2018).
16. Du, Z., Hatchard, T. D., Dunlap, R. A. & Obrovac, M. N. Combinatorial Investigations of Ni-Si Negative Electrode Materials for Li-Ion Batteries. *J. Electrochem. Soc.* **162**, A1858–A1863 (2015).
17. Liu, Y., Scott, B. & Obrovac, M. N. Ball Milled Si-W Alloys: Part I. Microstructural and Phase Evolution during Ball Milling. *J. Electrochem. Soc.* **166**, A1170–A1175 (2019).
18. Wang, D. Y. *et al.* A Comparative Study of Vinylene Carbonate and Fluoroethylene Carbonate Additives for LiCoO₂/Graphite Pouch Cells. *J. Electrochem. Soc.* **161**, A467–A472 (2014).

19. Ota, H., Sakata, Y., Inoue, A. & Yamaguchi, S. Analysis of Vinylene Carbonate Derived SEI Layers on Graphite Anode. *J. Electrochem. Soc.* **151**, A1659–A1669 (2004).
20. Jung, R. *et al.* Consumption of Fluoroethylene Carbonate (FEC) on Si-C Composite Electrodes for Li-Ion Batteries. *J. Electrochem. Soc.* **163**, A1705–A1716 (2016).
21. Petibon, R. *et al.* Studies of the Capacity Fade Mechanisms of LiCoO₂/Si-Alloy: Graphite Cells. *J. Electrochem. Soc.* **163**, A1146–A1156 (2016).
22. Dalavi, S., Guduru, P. & Lucht, B. L. Performance Enhancing Electrolyte Additives for Lithium Ion Batteries with Silicon Anodes. *J. Electrochem. Soc.* **159**, A642–A646 (2012).
23. Verma, P., Maire, P. & Novák, P. A review of the features and analyses of the solid electrolyte interphase in Li-ion batteries. *Electrochimica Acta* **55**, 6332–6341 (2010).
24. Cao, P. F. *et al.* Effect of Binder Architecture on the Performance of Silicon/Graphite Composite Anodes for Lithium Ion Batteries. *ACS Appl. Mater. Interfaces* **10**, 3470–3478 (2018).
25. Wachtler, M., Wagner, M. R., Schmied, M., Winter, M. & Besenhard, J. O. The effect of the binder morphology on the cycling stability of Li-alloy composite electrodes. *J. Electroanal. Chem.* **510**, 12–19 (2001).
26. Wu, M. *et al.* Toward an ideal polymer binder design for high-capacity battery anodes. *J. Am. Chem. Soc.* **135**, 12048–12056 (2013).
27. Chen, H. *et al.* Exploring Chemical, Mechanical, and Electrical Functionalities of Binders for Advanced Energy-Storage Devices. *Chem. Rev.* **118**, 8936–8982 (2018).

28. Kasavajjula, U., Wang, C. & Appleby, A. J. Nano- and bulk-silicon-based insertion anodes for lithium-ion secondary cells. *J. Power Sources* **163**, 1003–1039 (2007).
29. Pejovnik, S., Dominko, R., Bele, M., Gaberscek, M. & Jamnik, J. Electrochemical binding and wiring in battery materials. *J. Power Sources* **184**, 593–597 (2008).
30. Nguyen, C. C., Yoon, T., Seo, D. M., Guduru, P. & Lucht, B. L. Systematic Investigation of Binders for Silicon Anodes: Interactions of Binder with Silicon Particles and Electrolytes and Effects of Binders on Solid Electrolyte Interphase Formation. *ACS Appl. Mater. Interfaces* **8**, 12211–12220 (2016).
31. Park, J. H. *et al.* Polyimide gel polymer electrolyte-nanoencapsulated LiCoO₂ cathode materials for high-voltage Li-ion batteries. *Electrochem. commun.* **12**, 1099–1102 (2010).
32. Park, J. H., Cho, J. H., Kim, J. S., Shim, E. G. & Lee, S. Y. High-voltage cell performance and thermal stability of nanoarchitected polyimide gel polymer electrolyte-coated LiCoO₂ cathode materials. *Electrochim. Acta* **86**, 346–351 (2012).
33. Li, C.-C. & Wang, Y.-W. Binder Distributions in Water-Based and Organic-Based LiCoO₂ Electrode Sheets and Their Effects on Cell Performance. *J. Electrochem. Soc.* **158**, A1361–A1370 (2011).
34. El Ouatani, L. *et al.* Surface film formation on a carbonaceous electrode: Influence of the binder chemistry. *J. Power Sources* **189**, 72–80 (2009).
35. Xu, J., Chou, S. L., Gu, Q. F., Liu, H. K. & Dou, S. X. The effect of different binders on electrochemical properties of LiNi_{1/3}Mn_{1/3}Co_{1/3}O₂ cathode material in lithium ion batteries. *J. Power Sources* **225**, 172–178 (2013).

36. Choi, S., Kwon, T. woo, Coskun, A. & Choi, J. W. Highly elastic binders integrating polyrotaxanes for silicon microparticle anodes in lithium ion batteries. *Science* **357**, 279–283 (2017).
37. Wilson, A. M. & Dahn, J. R. Lithium Insertion in Carbons Containing Nanodispersed Silicon. *J. Electrochem. Soc.* **142**, 326–332 (1995).
38. Li, J., Christensen, L., Obrovac, M. N., Hewitt, K. C. & Dahn, J. R. Effect of Heat Treatment on Si Electrodes Using Polyvinylidene Fluoride Binder. *J. Electrochem. Soc.* **155**, A234–A238 (2008).
39. Tran, B. *et al.* Thick LiCoO₂/Nickel Foam Cathode Prepared by an Adhesive and Water-Soluble PEG-Based Copolymer Binder. *J. Electrochem. Soc.* **159**, A1928–A1933 (2012).
40. Jeong, S. S., Böckenfeld, N., Balducci, A., Winter, M. & Passerini, S. Natural cellulose as binder for lithium battery electrodes. *J. Power Sources* **199**, 331–335 (2012).
41. Lux, S. F., Balducci, A., Schappacher, F. M., Passerini, S. & Winter, M. (Invited) Na-CMC as Possible Binder for LiFePO₄/C Composite Electrodes: The Role of the Drying Procedure. *ECS Trans.* **25**, 265–270 (2010).
42. Wood, D. L., Li, J. & Daniel, C. Prospects for reducing the processing cost of lithium ion batteries. *J. Power Sources* **275**, 234–242 (2015).
43. Zhang, Z., Zeng, T., Lai, Y., Jia, M. & Li, J. A comparative study of different binders and their effects on electrochemical properties of LiMn₂O₄ cathode in lithium ion batteries. *J. Power Sources* **247**, 1–8 (2014).

44. Komaba, S. *et al.* Study on polymer binders for high-capacity SiO negative electrode of Li-Ion batteries. *J. Phys. Chem. C* **115**, 13487–13495 (2011).
45. Doberdò, I. *et al.* Enabling aqueous binders for lithium battery cathodes – Carbon coating of aluminum current collector. *J. Power Sources* **248**, 1000–1006 (2014).
46. Nguyen, B. P. N., Chazelle, S., Cerbelaud, M., Porcher, W. & Lestriez, B. Manufacturing of industry-relevant silicon negative composite electrodes for lithium ion-cells. *J. Power Sources* **262**, 112–122 (2014).
47. Guerfi, A., Kaneko, M., Petitclerc, M., Mori, M. & Zaghbi, K. LiFePO₄ water-soluble binder electrode for Li-ion batteries. *J. Power Sources* **163**, 1047–1052 (2007).
48. Lee, J. H., Lee, S., Paik, U. & Choi, Y. M. Aqueous processing of natural graphite particulates for lithium-ion battery anodes and their electrochemical performance. *J. Power Sources* **147**, 249–255 (2005).
49. Dimov, N., Noguchi, H. & Yoshio, M. A chemometric investigation of the effect of the process parameters on the performance of mixed Si/C electrodes. *J. Power Sources* **156**, 567–573 (2006).
50. Lux, S. F., Schappacher, F., Balducci, A., Passerini, S. & Winter, M. Low Cost, Environmentally Benign Binders for Lithium-Ion Batteries. *J. Electrochem. Soc.* **157**, A320–A325 (2010).
51. Vogl, U. S. *et al.* Mechanism of interactions between CMC binder and si single crystal facets. *Langmuir* **30**, 10299–10307 (2014).
52. Kovalenko, I. *et al.* A major constituent of brown algae for use in high-capacity Li-ion batteries. *Science* **334**, 75–79 (2011).

53. Lee, B. R. & Oh, E. S. Effect of molecular weight and degree of substitution of a sodium-carboxymethyl cellulose binder on Li₄Ti₅O₁₂ anodic performance. *J. Phys. Chem. C* **117**, 4404–4409 (2013).
54. Magasinski, A. *et al.* Toward efficient binders for Li-ion battery Si-based anodes: Polyacrylic acid. *ACS Appl. Mater. Interfaces* **2**, 3004–3010 (2010).
55. Higgins, T. M. *et al.* A Commercial Conducting Polymer as Both Binder and Conductive Additive for Silicon Nanoparticle-Based Lithium-Ion Battery Negative Electrodes. *ACS Nano* **10**, 3702–3713 (2016).
56. Porcher, W. *et al.* Understanding Polyacrylic Acid and Lithium Polyacrylate Binder Behavior in Silicon Based Electrodes for Li-Ion Batteries. *J. Electrochem. Soc.* **164**, A3633–A3640 (2017).
57. Yoon, T., Chapman, N., Nguyen, C. C. & Lucht, B. L. Electrochemical reactivity of polyimide and feasibility as a conductive binder for silicon negative electrodes. *J. Mater. Sci.* **52**, 3613–3621 (2017).
58. Wilkes, B. N., Brown, Z. L., Krause, L. J., Triemert, M. & Obrovac, M. N. The Electrochemical Behavior of Polyimide Binders in Li and Na Cells. *J. Electrochem. Soc.* **163**, A364–A372 (2015).
59. Han, Z. J. *et al.* Electrochemical lithiation performance and characterization of silicon-graphite composites with lithium, sodium, potassium, and ammonium polyacrylate binders. *Phys. Chem. Chem. Phys.* **17**, 3783–3795 (2015).
60. Kasinathan, R., Marinaro, M., Axmann, P. & Wohlfahrt–Mehrens, M. Influence of the molecular weight of poly-acrylic acid binder on performance of Si-alloy/graphite composite anodes for lithium-ion batteries. *Energy Technol.* **6**, 2256–2263 (2018).

61. Hu, B. *et al.* The existence of optimal molecular weight for poly(acrylic acid) binders in silicon/graphite composite anode for lithium-ion batteries. *J. Power Sources* **378**, 671–676 (2018).
62. Yu, X. *et al.* Three-Dimensional Conductive Gel Network as an Effective Binder for High-Performance Si Electrodes in Lithium-Ion Batteries. *ACS Appl. Mater. Interfaces* **7**, 15961–15967 (2015).
63. Koo, B. *et al.* A highly cross-linked polymeric binder for high-performance silicon negative electrodes in lithium ion batteries. *Angew. Chemie - Int. Ed.* **51**, 8762–8767 (2012).
64. Song, J. *et al.* Interpenetrated Gel Polymer Binder for High-Performance Silicon Anodes in Lithium-ion Batteries. *Adv. Funct. Mater.* **24**, 5904–5910 (2014).
65. Ebnesajjad, S. Characteristics of adhesive materials. in *Handbook of Adhesives and Surface Preparation* 137–183 (Elsevier, 2011).
66. Fauteux, D. G. & Shi, J. Lithium ion electrolytic cell and method for fabricating same. US Patent 5,856,045, 5 Jan., 1999.
67. Kay, A. Inorganic binders for battery electrodes and aqueous processing thereof. US Patent Application Publication 20110117432A1, 19 May, 2011.
68. Obrovac, M. N. & Christensen, L. Structural Changes in Silicon Anodes during Lithium Insertion/Extraction. *Electrochem. Solid-State Lett.* **7**, A93 (2004).
69. Zhang, W.-J. Lithium insertion/extraction mechanism in alloy anodes for lithium-ion batteries. *J. Power Sources* **196**, 877–885 (2011).
70. Iaboni, D. S. M. & Obrovac, M. N. $\text{Li}_{15}\text{Si}_4$ Formation in Silicon Thin Film Negative Electrodes. *J. Electrochem. Soc.* **163**, A255–A261 (2016).

71. Redondo-Iglesias, E., Venet, P. & Pelissier, S. Measuring Reversible and Irreversible Capacity Losses on Lithium-Ion Batteries. *2016 IEEE Veh. Power Propuls. Conf. VPPC 2016 - Proc.* (2016). doi:10.1109/VPPC.2016.7791723
72. Li, J., Lewis, R. B. & Dahn, J. R. Sodium carboxymethyl cellulose a potential binder for Si negative electrodes for Li-ion batteries. *Electrochem. Solid-State Lett.* **10**, A17–A20 (2007).
73. Bridel, J. S., Azaïs, T., Morcrette, M., Tarascon, J. M. & Larcher, D. Key parameters governing the reversibility of Si/carbon/CMC electrodes for Li-ion batteries. *Chem. Mater.* **22**, 1229–1241 (2010).
74. Karkar, Z., Guyomard, D., Roué, L. & Lestriez, B. A comparative study of polyacrylic acid (PAA) and carboxymethyl cellulose (CMC) binders for Si-based electrodes. *Electrochim. Acta* **258**, 453–466 (2017).
75. Nguyen, C. C., Seo, D. M., Chandrasiri, K. W. D. K. & Lucht, B. L. Improved Cycling Performance of a Si Nanoparticle Anode Utilizing Citric Acid as a Surface-Modifying Agent. *Langmuir* **33**, 9254–9261 (2017).
76. Liu, Y. *et al.* An All-Integrated Anode via Interlinked Chemical Bonding between Double-Shelled–Yolk-Structured Silicon and Binder for Lithium-Ion Batteries. *Adv. Mater.* **29**, 1–11 (2017).
77. Zhao, X., Dunlap, R. A. & Obrovac, M. N. Low Surface Area Si Alloy/Ionomer Composite Anodes for Lithium-Ion Batteries. *J. Electrochem. Soc.* **161**, A1976–A1980 (2014).

78. Yang, H., Bang, H., Amine, K. & Prakash, J. Investigations of the Exothermic Reactions of Natural Graphite Anode for Li-Ion Batteries during Thermal Runaway. *J. Electrochem. Soc.* **152**, A73–A79 (2004).
79. Krause, L. J., Brandt, T., Chevrier, V. L. & Jensen, L. D. Surface Area Increase of Silicon Alloys in Li-Ion Full Cells Measured by Isothermal Heat Flow Calorimetry. *J. Electrochem. Soc.* **164**, A2277–A2282 (2017).
80. Le, D.-B. Electrodes including polyacrylate binders and methods of making and using the same. US Patent 7,875,388 B2, 25 Jan., 2011.
81. Han, Z. J. *et al.* High-capacity Si-graphite composite electrodes with a self-formed porous structure by a partially neutralized polyacrylate for Li-ion batteries. *Energy Environ. Sci.* **5**, 9014–9020 (2012).
82. Lestriez, B. Functions of polymers in composite electrodes of lithium ion batteries. *Comptes Rendus Chim.* **13**, 1341–1350 (2010).
83. Gao, S. *et al.* High-performance LiFePO_4/C electrode with polytetrafluoroethylene as an aqueous-based binder. *J. Power Sources* **298**, 292–298 (2015).
84. He, M., Wang, Y. & Forssberg, E. Slurry rheology in wet ultrafine grinding of industrial minerals: A review. *Powder Technol.* **147**, 94–112 (2004).
85. Senapati, P. K., Mishra, B. K. & Parida, A. Modeling of viscosity for power plant ash slurry at higher concentrations: Effect of solids volume fraction, particle size and hydrodynamic interactions. *Powder Technol.* **197**, 1–8 (2010).

86. Sun, L., Su, T., Xu, L., Liu, M. & Du, H.-B. Two-dimensional ultra-thin SiO_x (0 < x < 2) nanosheets with long-term cycling stability as lithium ion battery anodes † ChemComm COMMUNICATION. *Chem. Commun* **52**, 4341 (2016).
87. Wang, C. *et al.* Self-healing chemistry enables the stable operation of silicon microparticle anodes for high-energy lithium-ion batteries. *Nat. Chem.* **5**, 1042–1048 (2013).
88. Sun, Y., Liu, N. & Cui, Y. Promises and challenges of nanomaterials for lithium-based rechargeable batteries. *Nat. Energy* **1**, 16071 (2016).
89. Wang, C. *et al.* A well-defined silicon nanocone-carbon structure for demonstrating exclusive influences of carbon coating on silicon anode of lithium-ion batteries. *ACS Appl. Mater. Interfaces* **9**, 2806–2814 (2017).
90. Wendel, D. *et al.* Silicon and Oxygen's Bond of Affection: An Acyclic Three-Coordinate Silanone and Its Transformation to an Iminosiloxysilylene. *J. Am. Chem. Soc.* **139**, 17193–17198 (2017).
91. TAYLOR, H. F. W. Proposed Structure for Calcium Silicate Hydrate Gel. *J. Am. Ceram. Soc.* **69**, 464–467 (1986).
92. Hochgatterer, N. S. *et al.* Silicon/graphite composite electrodes for high-capacity anodes: Influence of binder chemistry on cycling stability. *Electrochem. Solid-State Lett.* **11**, 76–80 (2008).
93. Lin, L. *et al.* In situ quantification of interphasial chemistry in Li-ion battery. *Nat. Nanotechnol.* **14**, (2019).
94. Tischendorf, B. *et al.* The density of alkali silicate glasses over wide compositional ranges. *J. Alloys Compd.* **239**, 197–202 (1996).